UNIVERSITY OF ILLINOIS
URBANA

AERONOMY REPORT NO. 93

ROCKET OBSERVATIONS OF SOLAR RADIATION DURING THE ECLIPSE OF 26 FEBRUARY 1979

by
H. M. Bliss
L. G. Smith

May 1, 1980

Library of Congress ISSN 0568-0581

Aeronomy Laboratory
Department of Electrical Engineering
University of Illinois
Urbana, Illinois

Supported by
National Aeronautics and Space Administration

UILU-ENG-80 2507

A E R O N O M Y R E P O R T

NO. 93

ROCKET OBSERVATIONS OF SOLAR RADIATION DURING THE ECLIPSE OF 26 FEBRUARY 1979

by

H. M. Bliss
L. G. Smith

May 1, 1980

Supported by
National Aeronautics and
Space Administration
Grant NGR 14-005-181

Aeronomy Laboratory
Department of Electrical Engineering
University of Illinois
Urbana, Illinois

ABSTRACT

In February 1979 three Nike Tomahawk rockets were launched in Red Lake, Ontario, one previous to, and two during, the total eclipse of the sun, for the purpose of studying the atmosphere and it's interaction with solar radiation. On board were experiments from both the University of Illinois and the University of Bern, Switzerland. This paper describes the method and preliminary results of three of these experiments that were used to measure solar radiation in the X-ray, Lyman-α, and visible parts of the spectrum. The instrumentation designed for this investigation is described in detail, along with post-flight data processing techniques. The retrieved data have been processed to some extent to verify that a valid representation of the solar radiation has been obtained.

The Lyman-α experiment yielded very good results, and preliminary data have been included in this report. The visible radiation experiment served as support for the other experiments and also functioned well. Due to a high level of energetic particles during the eclipse, the X-ray data were contaminated and are not presented. However, satellite observations indicate no appreciable level of X-rays from the sun during the time of the eclipse.

TABLE OF CONTENTS

LIST OF TABLES

LIST OF FIGURES

1. INTRODUCTION

This report describes experiments prepared for rockets launched in Canada, near Red Lake, during, and before, the total solar eclipse of 26 February 1979. Of major interest is solar radiation in the UV and X-ray parts of the spectrum, both as they relate to the source (the sun) and to their interaction with the atmosphere.

These experiments were part of an integrated payload also containing experiments for ion composition, electron density and energetic particles, with the broad objective of studying the chemical modelling of the lower ionosphere (which, here, because of the pre-determined rocket apogee, is defined to extend up to 135 km altitude). Thus the solar radiation experiments serve to give, to the modelling, the necessary input rates due to Lyman-α (121.6 nm) and hard X-rays (as represented by the wavelength range of 0.2 to 0.8 nm).

The importance of solar eclipses in the study of the ionosphere is further discussed in Chapter 2.

The experiment to measure solar X-rays in the wavelength range 0.2 to 0.8 nm is described in Chapter 3. Though this experiment performed well in the rocket flights, an unexpectedly high flux of energetic particles contaminated the data. Fortunately, other (satellite) data show that the sun itself was not active and therefore that hard X-rays could not have been a significant ionization source.

The Lyman-α experiment, described in Chapter 4, did perform well, and valuable data were obtained. In addition to the measurement of (energy) flux at this wavelength, used for calculation of ionization rates, these data are used in studying scattered Lyman-α, in observing the brightness of the solar chromosphere (as a function of radial distance), and in determining rocket aspect (when used in conjunction with the spin magnetometer).

A sensor for visible radiation was also included in the payload, primarily as a check of the trajectory data and of the calculations of eclipse circumstances. This experiment, described in Chapter 5, also performed well.

The integration of these experiments into the payloads for Nike Tomahawk rockets is described in Chapter 6.

1. INTRODUCTION

This report describes experiments prepared for rockets launched in Canada, near Red Lake, during, and before, the total solar eclipse of 26 February 1979. Of major interest is solar radiation in the UV and X-ray parts of the spectrum, both as they relate to the source (the sun) and to their interaction with the atmosphere.

These experiments were part of an integrated payload also containing experiments for ion composition, electron density and energetic particles, with the broad objective of studying the chemical modelling of the lower ionosphere (which, here, because of the pre-determined rocket apogee, is defined to extend up to 135 km altitude). Thus the solar radiation experiments serve to give, to the modelling, the necessary input rates due to Lyman-α (121.6 nm) and hard X-rays (as represented by the wavelength range of 0.2 to 0.8 nm).

The importance of solar eclipses in the study of the ionosphere is further discussed in Chapter 2.

The experiment to measure solar X-rays in the wavelength range 0.2 to 0.8 nm is described in Chapter 3. Though this experiment performed well in the rocket flights, an unexpectedly high flux of energetic particles contaminated the data. Fortunately, other (satellite) data show that the sun itself was not active and therefore that hard X-rays could not have been a significant ionization source.

The Lyman-α experiment, described in Chapter 4, did perform well, and valuable data were obtained. In addition to the measurement of (energy) flux at this wavelength, used for calculation of ionization rates, these data are used in studying scattered Lyman-α, in observing the brightness of the solar chromosphere (as a function of radial distance), and in determining rocket aspect (when used in conjunction with the spin magnetometer).

A sensor for visible radiation was also included in the payload, primarily as a check of the trajectory data and of the calculations of eclipse circumstances. This experiment, described in Chapter 5, also performed well.

The integration of these experiments into the payloads for Nike Tomahawk rockets is described in Chapter 6.

The algorithms and programs for computer-processing the data from the Lyman-α experiments are given in Chapter 7.

The eclipse circumstances of the rockets, calculated from the trajectory data, are presented in Chapter 8, together with a preliminary evaluation of the performance of the experiments.

Chapter 9 contains a summary of this report and some suggestions for additional data processing and analysis.

2. SOLAR ECLIPSES AND THE IONOSPHERE

A solar eclipse provides an opportunity to study the interaction of solar radiation with the ionosphere as well as the sun as a source of ionizing radiation. Since an eclipse provides a predictable obscuration of the solar disk, changes in the electrical composition of the ionosphere during an eclipse can be related to the ionizing radiation coming from the sun. Rocket investigations are suitable for this type of study because the solar radiation can be measured simultaneously with the electrical properties of interest at various levels of the atmosphere. This chapter will discuss work that has already been done in this area and results of previous rocket experiments.

2.1 *Electron Density*

During an eclipse, electron density measurements are made principally in the *D*, *E*, and *F* regions of the ionosphere. In the *F* region (above about 250 km) the eclipse effect is difficult to identify because of the generally less regular behavior and longer time constants associated with this region.

The most regular of the ionospheric layers, the *E*-layer (at about 110 km), exhibits a clearly defined eclipse effect. The electron density is found to decrease gradually as the visible disk of the sun is obscured, but even in total eclipses of the maximum possible duration (approximately 7 minutes) the electron density never decreases to less than one third of its normal value [*Smith et al.*, 1965].

Originally it was thought that ionizing radiation from the sun is entirely absent during totality and that the time constants of the processes by which the electrons are removed are such that the electron density does not fully decay to zero. It has since been realized that the solar corona, which due to its size is not fully obscurred during a total eclipse, is a significant source of radiation so that even during totality there is a certain amount of ionizing radiation reaching the atmosphere causing reduced (but still present) electron concentrations.

This theory has been supported by previous eclipse rocket investigations. Particularly during the eclipse of 7 March 1970 at Wallops Island, Virginia where *Accardo et al.* [1972] measured the residual flux of totality in the bands 0.2-0.8, 0.8-2.0, and 4.4-6.0 nm to be 5, 7, and 16 percent of

the flux from the uneclipsed sun. Also *Smith* [1972] measured the Lyman-α radiation (1216 Å) from the solar chromosphere and corona during the totality of an eclipse to be 0.15 percent of the flux from the unobscured sun.

In the *D* region (nominally 60-90 km) electron densities have also been observed to decrease substantially below their normal value during an eclipse. [*Smith et al.*, 1965; *Mechtly et al.*, 1969; *Mechtly et al.*, 1972]. This, as yet, has been not satisfactorily explained, partly due to the complex chemistry of the water-cluster ions in this region. This is the region of particular interest in the experiments for the eclipse of 26 February 1979.

2.2 *Ionizing Radiation*

As the major source of ionization in the earth's atmosphere, the radiation generated by the sun covers a wide spectrum of energies including the more important X-rays and extreme ultra-violet radiations. The solar spectrum includes numerous emmission lines eminating from the chromospheric and coronal regions of the sun, as well as some continuum radiation.

The present study is concerned with solar radiation which can penetrate to the lowest part of the ionosphere, the *D* region. The important ionizing radiation of the *D* region are the hard X-rays (0.25 to 0.8 nm), the intense Lyman-α line emission (121.6 nm), and the energetic charged particles that make up the galactic cosmic rays [*Whitten and Poppoff*, 1971].

Measurements of solar radiation during an eclipse prove valuable in three ways. The first is that radiation measurements can provide information about the radiation source; second, the concentration profiles of the constituents of the neutral atmosphere can be derived using absorption spectroscopy methods; and third, insight is gained into the mechanisms of radiation-ionospheric interactions by observing the variation in electron density caused by the obscuration of the solar radiation source.

2.2.1 *Solar radiation source.* Previous eclipse flights have provided valuable information about the sun as a source of Lyman-α radiation. It has been confirmed that most of the solar Lyman-α radiation eminates from the chromosphere, which has been shown to extend approximately 4000 km above the surface of the photosphere (the visible sphere) [*Weeks and Smith*, 1971]. The eclipse is thus of smaller magnitude for Lyman-α that it is in the visible spectrum. This is illustrated in Figure 2.1 in which the crosses

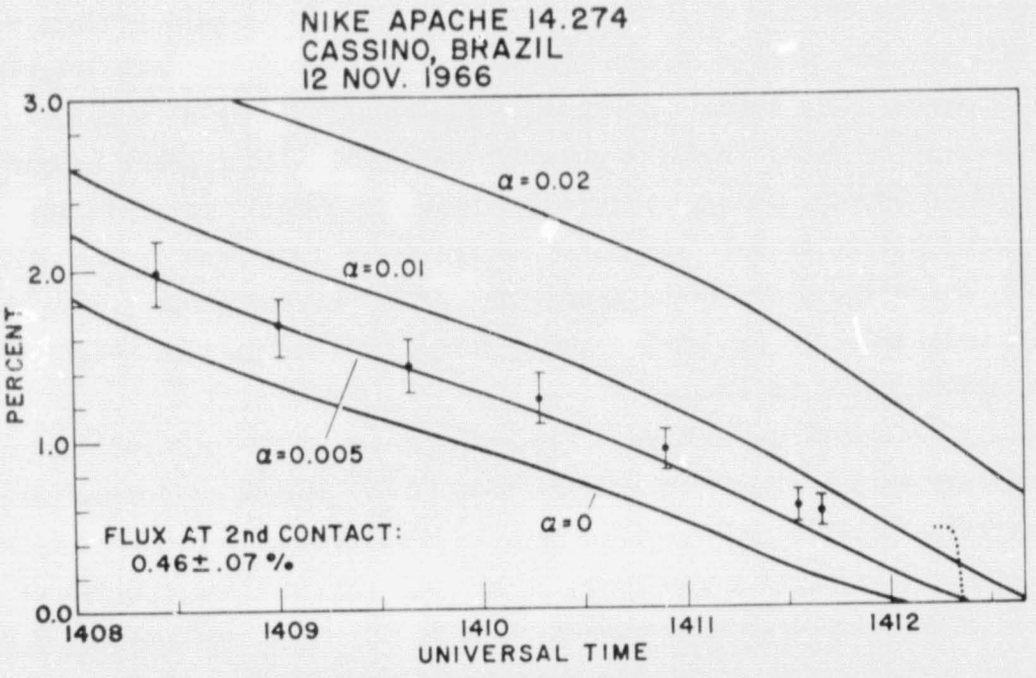

Figure 2.1 Lyman-α data for south limb compared with chromosphere models. [*Weeks and Smith*, 1971]

give the Lyman-α flux as a percentage of the obscured sun as observed by Nike Apache 14.274 during the eclipse of 12 November 1966. The solid curves show the calculated percentage of the disk visible as derived from the trajectory of the payload for different disc sizes. The curve labeled $\alpha = 0$ refers to the size of the solar disc as it appears in the visible spectrum, while the curves for $\alpha = 0.005$, $\alpha = 0.01$, and $\alpha = 0.02$ refer to discs larger by 0.5, 1, and 2 percent, respectively. It is seen in Figure 2.1 that the chromosphere has a diameter approximately 0.5 percent larger than that of the visible disc.

During the eclipse of 7 March 1970 further Lyman-α measurements were made with the aid of Nike Apache 14.437. It was found that the brightness of the chromospheric Lyman-α decreases exponentially over a range of 0.005-0.03 solar radii from the photospheric limb, with a scale height of 3835 ± 70 km [*Smith*, 1972]. Figure 2.2 shows this measured variation expressed relative to the brightness of the first 1 percent of the disc exposed, which was found to be approximately 14 percent greater than the average brightness of the entire Lyman-α disc indicating limb brightening of the chromosphere in Lyman-α.

2.2.2 *Absorption profiles.* The measurement of the absorption profile of a certain wavelength of solar radiation is one method of determining concentration profiles of specific neutral constituents of the atmosphere. This technique requires a knowledge of the absorption cross section of the species in question over a frequency range inclusive of the pass-band of the radiation detector. An effective absorption cross section of the species can be derived by taking the weighted mean of the absorption cross section over the spectral width of the detector. When applying this technique one must be certain that the absorption of the species in question is indeed being measured and not some mixture of constituents with similar absorption properties. Measurements of Lyman-α and 260 nm absorption profiles have provided data for molecular oxygen and ozone concentrations, respectively [*Evans and Smith*, 1975]. Concentration profiles obtained during eclipse conditions provide information about the transport phenomena of the neutral species under investigation.

In addition to deriving concentration profiles, absorption profiles are also useful in studying scattered Lyman-α radiation.

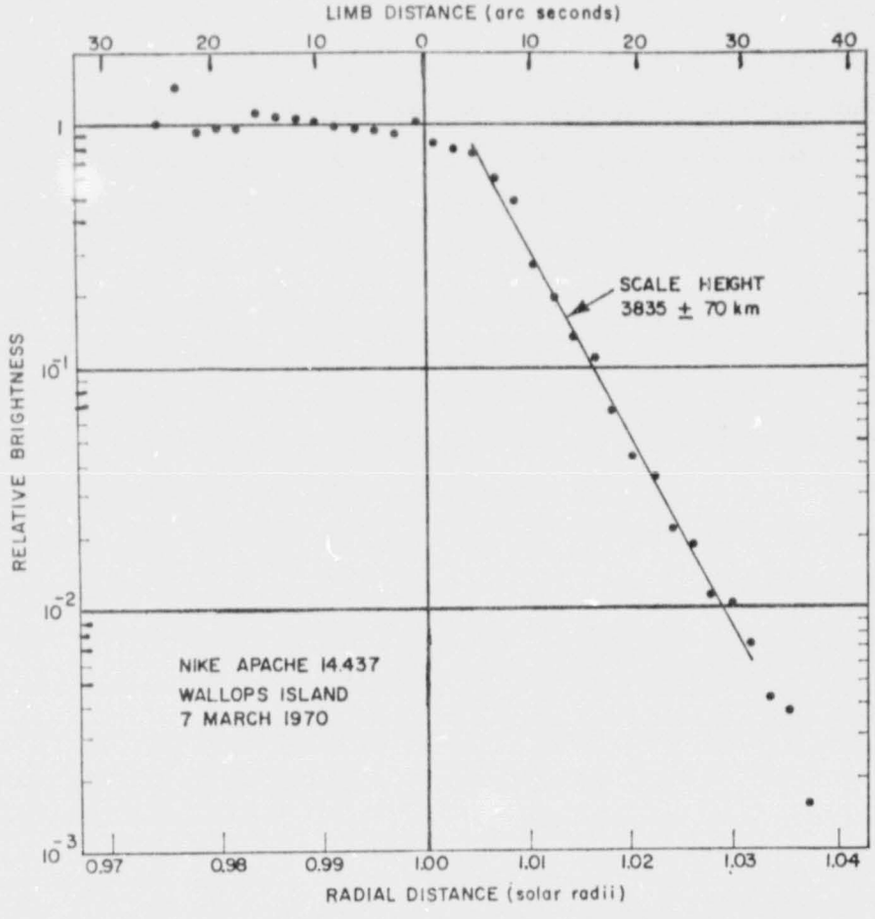

Figure 2.2 The relative brightness of the solar limb in Lyman-α. [*Smith*, 1972]

2.2.3 *Ionization of the D-region.* As already has been noted the three main sources of ionization of the *D*-region (at about 80 km) are Lyman-α radiation, hard X-rays, and galactic cosmic rays. The very energetic galactic cosmic rays and solar X-rays ionize all atmospheric constituents, whereas the Lyman-α radiation can ionize only those constituents having ionization potentials lower than 10 eV.

The relative importance of the three major sources of *D*-region ionization was determined during the eclipse of 7 march 1970 by *Accardo et al.* [1972]. It was found that at 80 km, during totality, the ionization of a trace constituent, nitric oxide, by Lyman-α produced 4×10^{-2} ion-pairs cm^{-3} s^{-1}, the ionization by X-rays (0.2 to 0.8 nm) produce 1.1×10^{-2} ion-pairs cm^{-3} s^{-1}, and the ionization by galactic cosmic rays produced 0.4×10^{-2} ion-pairs cm^{-3} s^{-1}, thus giving a total, for these three sources 5.5×10^{-2} ion-pairs cm^{-3} s^{-1}. These data indicate that ionization of NO by Lyman-α radiation is the major source of ionization at the altitudes of the *D*-region. This is because the intense Lyman-α line of the solar spectrum aligns with a transmission window in the absorption cross section of molecular oxygen (a major constituent of the atmosphere) allowing penetration of Lyman-α into the *D*-region, whereas the other ionizing radiations are absorbed at higher altitudes. Therefore, Lyman-α radiation is of major interest for interpretation of the changes in electrical properties of the *D*-region that occur during an eclipse.

3. SOLAR X-RAYS (0.2 to 0.8 nm)

Each of the three payloads carried a Geiger counter sensitive to radiation in the range of 0.2 to 0.8 nm (1.5 to 6.2 keV). The operation of the Geiger counter and associated counter circuit will be discussed, followed by the calibration procedures and calibration records for the X-ray experiment.

Unit optical depths are 72 and 95 km for the wavelengths 0.2 and 0.8 nm, respectively. The band of X-rays selected for investigation is representative of these unit optical depths and is a source of ionization in the *D*-region. The band of X-rays is convenient for measurement by a Geiger counter with a thin window of beryllium.

Although this band of X-rays is relatively broad, the actual spectral energy distribution can be recovered by assuming a black body temperature for the source. This can be obtained from the absorption profile of the radiation, although not during the eclipse itself. The method is discussed in *Accardo et al.* [1972].

3.1 *The Geiger Counter and Bias Circuit*

A geiger counter is an extremely sensitive device used for the detection of ionizing radiation, either corpuscular or electromagnetic. The high sensitivity of the Geiger counter is due to the fact that an individual photon or energetic particle can trigger a discharge from the Geiger counter tube. Thus any types of particles which can release charge within a Geiger counter can be detected, including X-rays which produce ionization by secondary processes [*Price*, 1964].

Geiger counters generally consist of a chamber containing a conducting cylindrical surface which surrounds a wire along its axis of symmetry. A cylindrical geometry is commonly used because it facilitates parameters that are easily controlled to meet design requirements. The chamber is filled with an inert gas, usually helium, argon, or neon. A small percentage of a polyatomic gas is also added for quenching purposes. Quenching is the process of terminating an electrical discharge within the tube, which will be explained later in this section. Any polyatomic gas molecule will produce the quenching action although each polyatomic gas has certain advantages and disadvantages which must be considered when choosing a gas fill for a Geiger counter [*Korff*, 1947].

The Geiger counters used in the present experiment are contained in a stainless steel cylindrical chamber which also serves as the outer conductor. The chamber has a wall thickness of 0.5 mm, radius of 12.5 mm, length of 76 mm, a central wire of radius 0.005 mm, and is filled with neon at 0.5 Atm with 1% isobutane added as the quenching agent.

For operation of the Geiger counter a large potential is applied between the outer conductor which is referred to as the cathode and the central wire which is called the anode or, sometimes, the collector electrode. This potential sets up an electric field defined by the geometry of the electrodes, with magnitude given by (3.1),

$$E \cong \left| \frac{V}{r \log_{10}(r_1/r_2)} \right| \tag{3.1}$$

where E is the electric field strength, V is the applied voltage between the cathode and the anode, r is the point of observation, and r_1 and r_2 are the radii of the wire and the cylinder respectively. Using equation (3.1), the aforementioned dimensions of the Geiger tube, and an applied voltage of 950 V (the voltage used in the experiment), the electric field intensity is found to vary monotonically from 79.2 kV cm^{-1} at the wire surface to 317 kV cm^{-1} at the cylinder wall. At only 1 mm away from the wire surface the field strength drops to 3.77 kV cm^{-1} indicating a rapid increase in the electric field when approaching the central wire. Keeping this in mind, an explanation of the discharge operation of the tube will follow.

Assume that an ionizing event has taken place within the volume of the Geiger tube, i.e., one or more charged particles, or photons, or neutral particles have by some process produced ionization within the electric field inside the Geiger tube. Once this ionizing event has taken place the electric field will cause the positive ions to move toward the cylinder wall and the negative ions and the electrons to move toward the central wire. As the electrons approach the wire, they enter the region of rapidly increasing electric field and are therefore accelerated to high velocities. These electrons will cause the release of more electrons upon collision with any atoms in their path. The additional electrons released along with the original electrons will continue moving toward the wire causing even more electrons to be released along the way giving an avalanche effect.

Since the charge collected on the wire depends on the final number of electrons arriving there, a response due to one single electron is greatly amplified in this manner.

While this process is taking place the positive ions, moving much slower due to their greater mass, drift toward the cylinder wall. Ideally, when the positive ions reach the cylinder wall they are neutralized terminating the discharge process and the counter tube is ready to detect another ionization event. In reality the process of neutralizing the positive ions may result in the release of electrons which will move inward and initiate new avalanches and cause the discharge process to repeat itself, resulting in a multiple discharge or a continuous, self-sustaining discharge. To prevent the undesirable release of electrons upon neutralization of the positive ions is the function of the quenching gas. The quenching gas will inhibit the release of electrons thus removing the conditions for reinitiation of the discharge process.

The Geiger tube does not immediately recover from the discharge, in that the positive ions form a nearly cylindrical sheath around the central wire which disrupts the electric field and prevents the initiation of new avalanches near the anode. This situation continues until the ion sheath has migrated out of the high electric field region near the wire. The time interval during which the tube is completely insensitive to incoming radiation is called the "dead time", followed by the "recovery time" which is the time required for the pulse size to regain its original amplitude. Another time interval that is commonly defined is the "resolving time" which is the time after a count for which the entire measuring system is insensitive to incoming pulses. The resolving time is always greater or equal to the dead time.

Figure 3.1 illustrates these time intervals for a Geiger counter operating at a high counting rate.* The resolving time of a Geiger counter presents an upper bound on the counting rate, but if the resolving time, τ, is known, a corrected counting rate N_o can be approximated for any measured rate N by using (3.2) [*O'Kelley*, 1962].

---

*To actually "see" an output resembling Figure 3.1 would require a storage oscilliscope because each pulse is triggered at a different time.

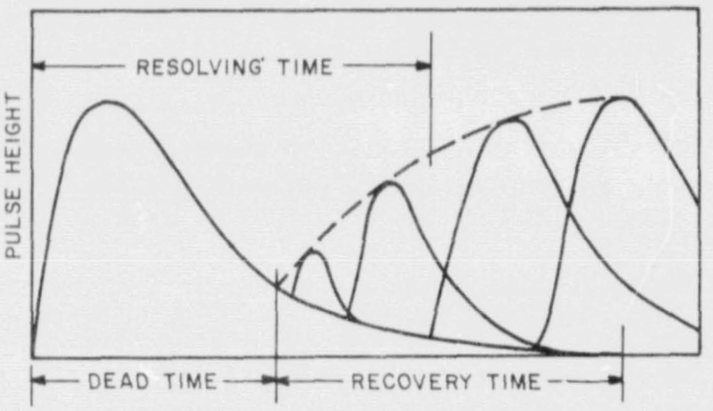

Figure 3.1 Illustration of pulse shapes in a typical Geiger tube operating at a high counting rate. The dead time and recovery times are determined by the Geiger tube characteristics, but the resolving time depends on the electronic recording system [*O'Kelley*, 1962].

$$N_o = \frac{N}{1 - N\tau} \tag{3.2}$$

Since the Geiger counters for this experiment are used to detect X-rays which have a relatively high photoelectric absorption cross section, a thin beryllium window is mounted in the side of the cylinder to admit the X-rays into the Geiger tube. Most of X-rays incident upon the window will enter the tube because of the relatively low photoelectric absorption cross section of beryllium and the thinness of the window. The window and gas fill combination determines the band of wavelengths for which the counter is sensitive. The efficiency of the tube in the low energy region decreases because of absorption in the window and in the high energy region because of the decrease in the photoelectric absorption cross section of the gas fill. With the present beryllium window and neon gas fill, the counter is theoretically sensitive to X-rays in the range of 1.5 to 6.2 keV. However, during the eclipse it became evident the the counter is also sensitive to electrons with energies greater than 40 keV.

3.2 *Electronic Circuits*

The block diagram in Figure 3.2 shows the structure of the X-ray electronics. The resolving time, as described in the previous section, is determined by the duration of a positive going pulse from the output of the monostable multivibrator during which the circuit will not respond to any signal coming from the X-ray tube. The dead time of the detector is approximately 130 microseconds while the resolving time of the circuit is set to approximately 190 microseconds giving an extra margin to allow for any changes in the performance of the counter during the flight as well as variations in operating characteristics from one counter to another.

The 950 V bias necessary for the operation of the counter in the Geiger region is derived from the +30 V power bus using a 3 watt regulated DC-to-DC converter module manufactured by Technetic, Inc. Figure 3.3 gives the details of the biasing circuit. The series combination of R_4 and C_4 serves as a smoothing filter for the DC-to-DC converter output. The signal from the detector tube will have a 950 V DC component which is removed from the active differentiator input by the capacitor C_3. The resistance R_2 isolates the power supply from the central wire, thus allowing the anode voltage to drop upon the collection of electrons following a discharge in the Geiger

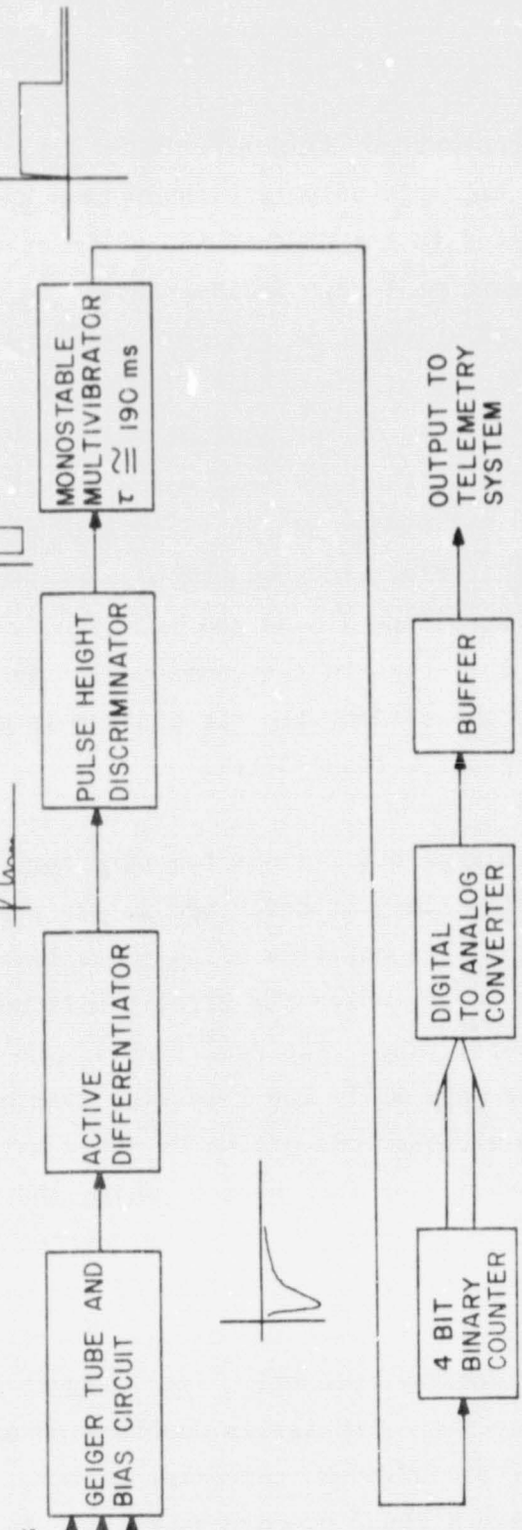

Figure 3.2 Block diagram showing structure of the X-ray electronics.

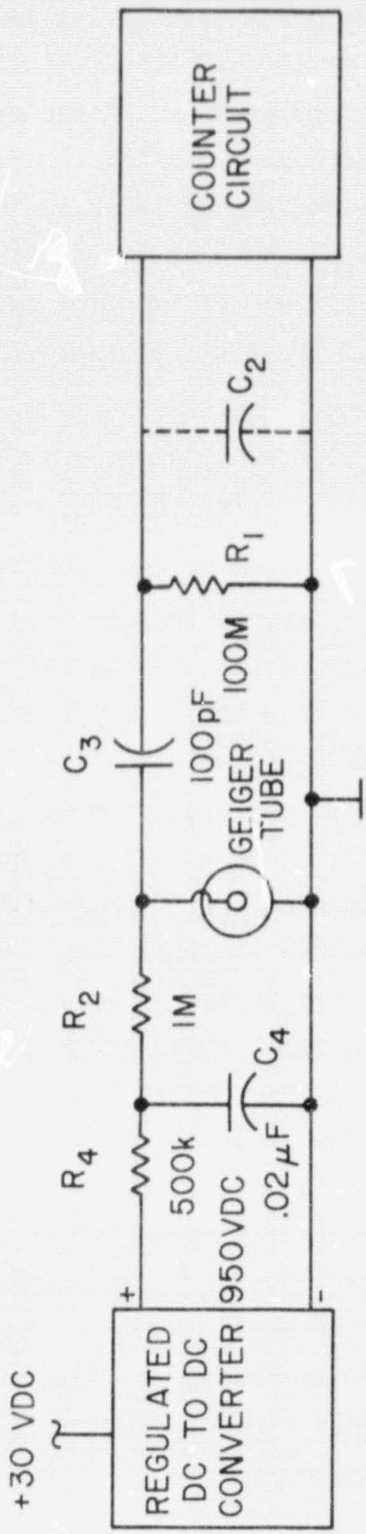

Figure 3.3 Details of the biasing circuit for the X-ray electronics.

counter. R_2 also serves as a protective device in that the 1 MΩ resistor will limit the current to 1 mA if the counter should go into continuous discharge or if the high voltage portions of the circuit should be accidentially short circuited during testing. Similarly R_1 will provide current limiting if the capacitor C_3 fails in such a way that it acts as a short circuit. Neglecting R_1 because it is relatively large compared with R_2 and R_4 and neglecting C_4 because it is relatively large compared with C_3 and the input capacitance C_2, the time constant of the bias circuit is given by,

$$\tau_B = RC = (R_2 + R_4)(R_2 + R_4)\left(\frac{C_2C_3}{C_2 + C_3}\right) = 75\ \mu s$$

where the values for R_2, R_4, C_2, and C_3 are taken from Figure 3.3. Therefore the response time of the bias circuit is less than the 190 μs resolving time of the counter circuit and will not slow down the count rate.

The sensitivity of the active differentiator is such that pulses of amplitude greater than the threshold of the pulse height discriminator will be produced for two consecutive particles coming into the detector not closer than one system dead-time apart. Thus a photon or an energetic particle entering a not fully recovered Geiger counter will produce a smaller than normal output pulse, as shown in Figure 3.1, but will be detected by the edge sensing characteristics of the differentiation circuit and will also trigger the monostable multivibrator via the pulse height discriminator given that the particle enters the tube at least 190 μs later than the previous photon or energetic particle.

The pulse height discriminator performs a twofold function in that it provides the proper logic levels for the multivibrator input and also provides some degree of noise immunity by only reacting to inputs greater or equal to a predetermined threshold voltage. Figure 3.4 gives the circuit details for the pulse-height discriminator. The threshold voltage V_T is selected by choosing the proper value for R_3 in the following equation,

$$V_T \cong \frac{22200}{R_3} - 0.2$$

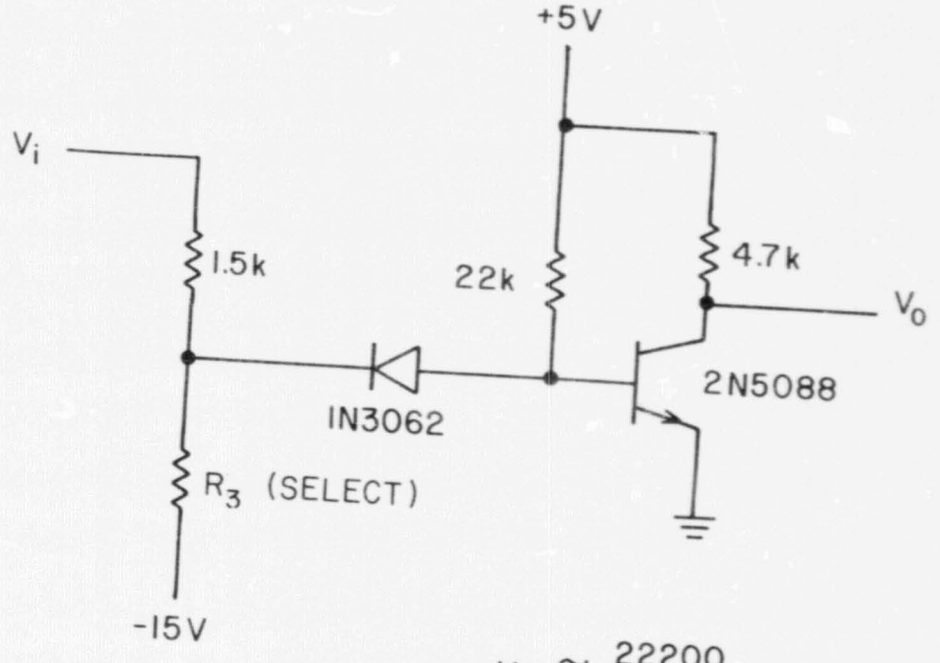

Figure 3.4 The pulse-height discriminator circuit used in the X-ray electronics.

To transmit a series of pulses such as those coming from the multivibrator output would require a very large dynamic range. In order to present this information on the FM/FM telemetry system of the payload the following scheme is used, which decreases the dynamic range requirements of the telemetry channel while retaining the information density of the detector output.

As mentioned previously the monostable multivibrator will produce an output pulse of approximately 190 μs when a photon or energetic particle enters the counter. These pulses are fed into a 4 bit binary counter with output to a 4 bit digital-to-analog converter which will produce a lower bandwidth signal consisting of a series of 16 step staircases as the counter cycles through its 16 different outputs. The signal is then amplified by the buffer amplifier to translate the staircase to a 0 to 5 V level compatiable with the telemetry channel. Therefore, to determine an average count rate over a certain time interval, one must determine the number of "steps" in that interval.

3.3 *Testing and Calibration*

Table 3.1 of this section gives a summary of the testing and calibration procedures for the X-ray electronics and are followed by Figures 3.5 and 3.6 which give the circuit details and the component layout, respectively. These figures should be referenced while reviewing the testing and calibration procedure. Table 3.2 gives the calibration record for the Geiger counters flown in Nike Tomahawks 18.1020, 18.1021, and 18.1022.

Figure 3.7 is a photograph of a fully assembled X-ray deck. The Geiger Tube can be seen in the lower left-hand corner of the picture.

Table 3.1 Procedure for the testing and calibration of the X-ray electronics.

1. Adjust the DC to DC converter to give an output of 950 V.
2. Place a radioactive source near the window of the counter tube and observe the tube output at test point T_1 to verify proper operation of the tube. The pulses should be like the ones shown in Figure 3.1 with a maximum magnitude of approximately 1 V.
3. While the counter is counting select the capacitance C_2 that will just stop the damped oscillations at test point T_3. Measure and record the magnitude of the pulses. The magnitude should be approximately 7 V and to achieve this it is acceptable to allow a few cycles of damped oscillations if necessary as long as they damp out in less than one resolving time.
4. Isolate the input to the pulse height discriminator and apply a sine wave to determine the threshold voltage. While observing the output of the monostable multivibrator slowly increase the sine wave amplitude until the monostable is triggered. Measure the record and the threshold voltage which would be the amplitude that just triggers the monostable multivibrator.
5. Using the sine wave input to the pulse height discriminator as in step 4 adjust the amplitude to a value greater than the threshold voltage and monitor the output of the multivibrator. Adjust R_6 to give a pulse duration of approximately 190 μs.
6. With input to pulse height disciminator as in step 5 adjust R_9 to produce a 0 to 5 V staircase at test point T_9.
7. Reconnect differentiator output to the pulse height discriminator, place test source near the Geiger tube window, and observe output at test point T_9 to insure overall proper operation of the Geiger counter.

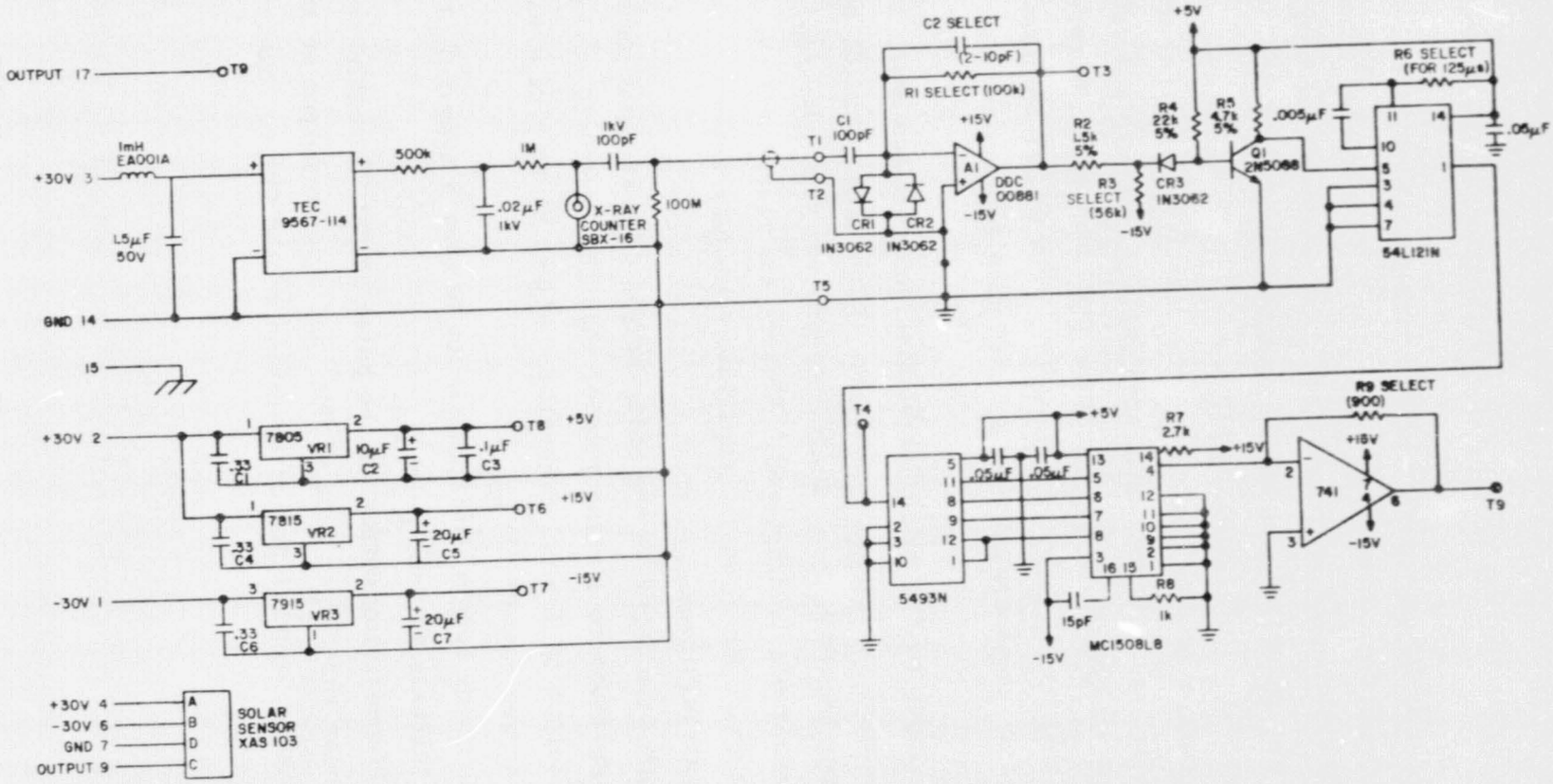

Figure 3.5 Circuit details of the X-ray electronics.

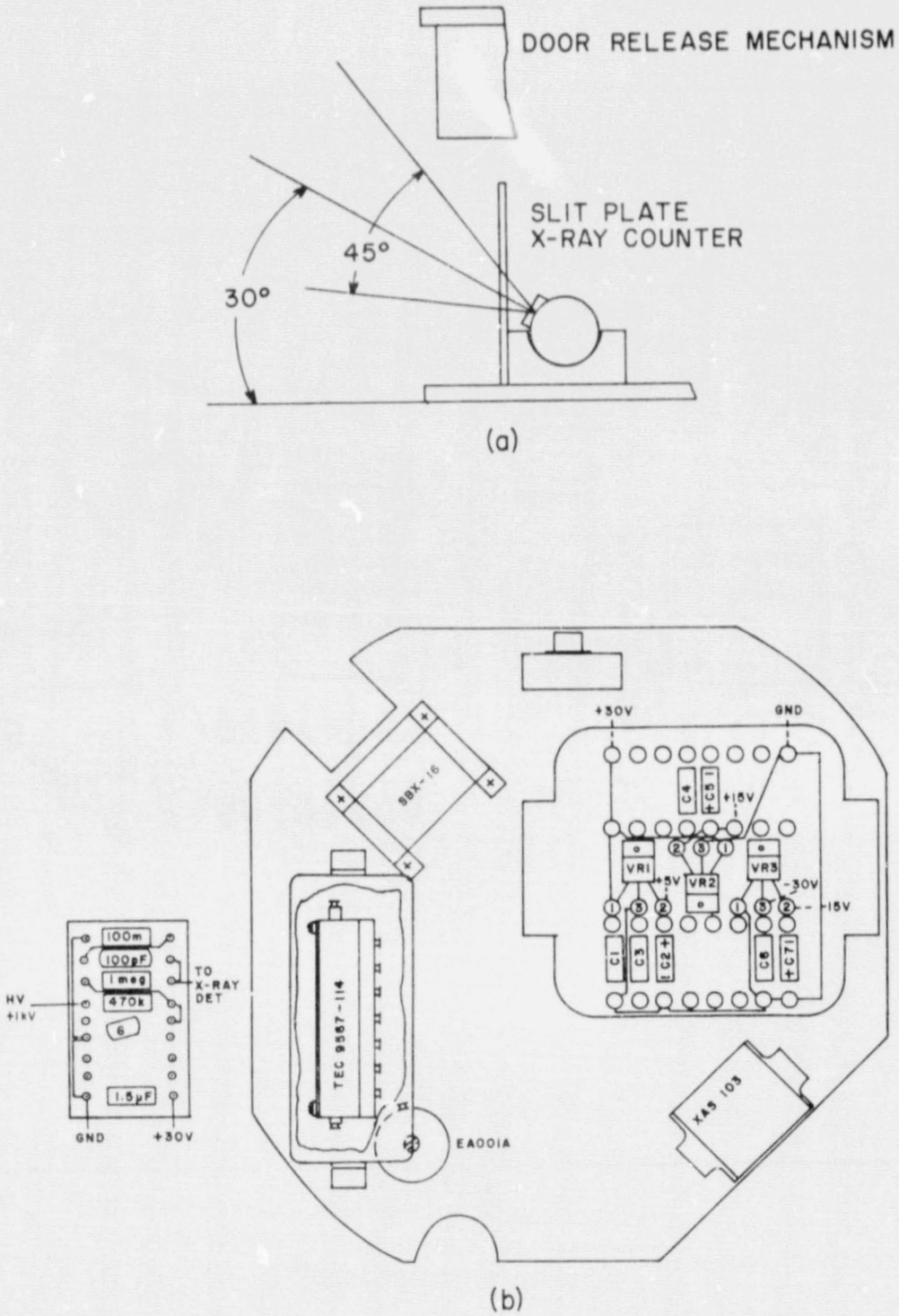

Figure 3.6 Component layout for the X-ray electronics.

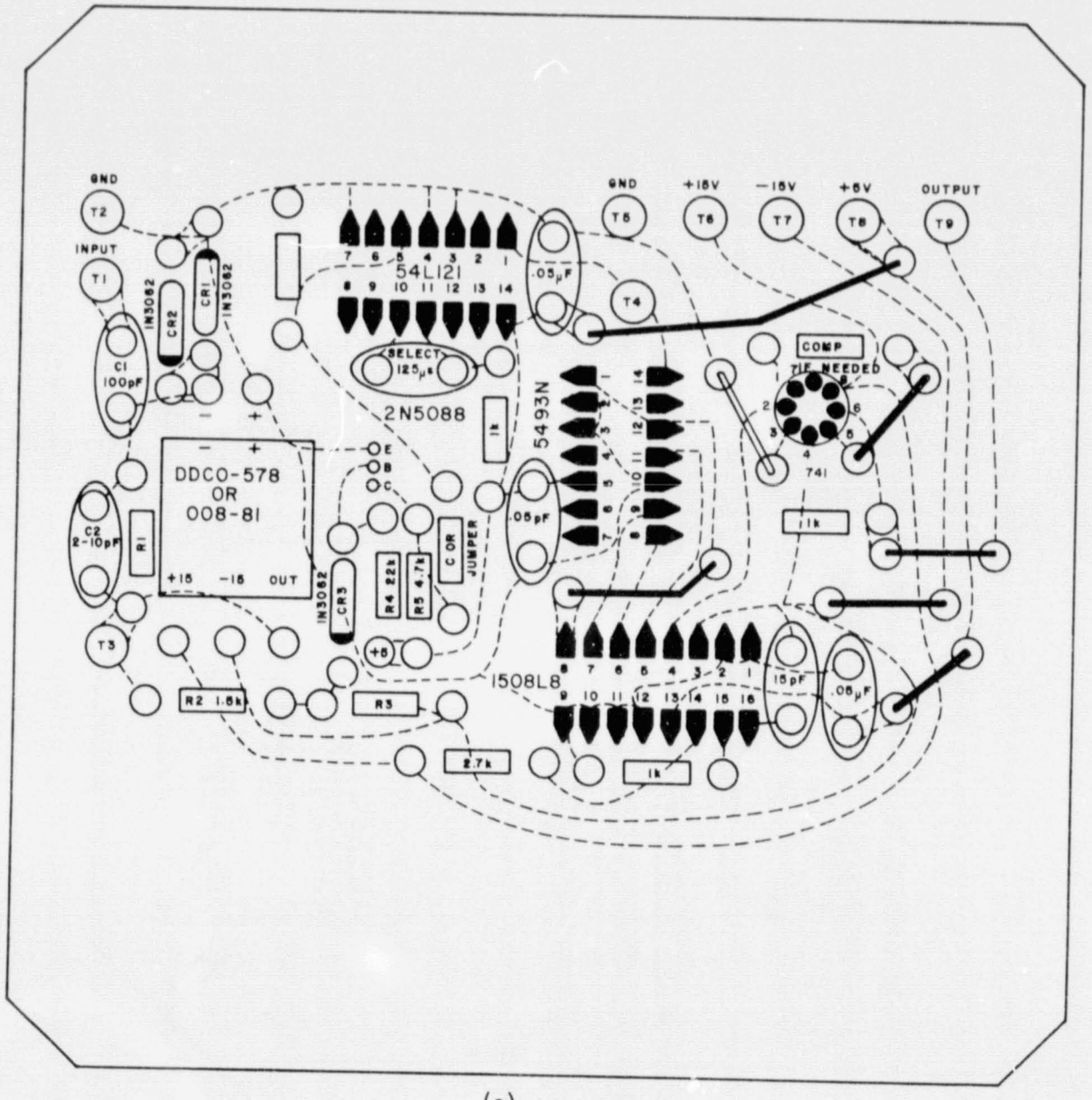

(c)

Figure 3.6 Continued.

Table 3.2 Calibration record for the X-ray electronics.

	18.1020	18.1021	18.1022
SUPPLY VOLTAGE (V)	950	950	950
TUBE OUTPUT (V)	-1.0	-0.6	-1.0
C_2 (pF)	6	4	5
DIFFERENTIATOR OUTPUT (V)	7.2	6.5	6.8
THRESHOLD VOLTAGE (V)	0.23	0.26	0.22
RESOLVING TIME (μs)	194	193	194
R_6 (Ω)	28K, 1%	24K||270K, 5%	24.9K, 5%
OUTPUT SWING (V)	0 - 5.0	0 - 4.8	0 - 5.0
R_9 (Ω)	1K, 5%	1K||18K, 5%	820, 10%

Figure 3.7 A photograph of the X-ray deck for the payload of Nike Tomahawk 18.1021. The larger aluminum can houses the X-ray electronics and the smaller one contains the high-voltage bias circuit. The Geiger counter and aperture-defining plate are at the lower left. This deck also carries the solar sensor, shown at the upper right.

4. LYMAN-α RADIATION

Each payload carries two photometers* sensitive to a narrow spectral band of solar radiation. When flux of the proper wavelength (Lyman-α) is incident upon one of these devices, a small current proportional to the intensity of the radiation is produced, which is fed into an electrometer (current-to-voltage converter). The following sections describe the operation of the photoionization chamber, the associated electronics, and the use of the two photometers in determining rocket aspect and Lyman-α flux.

4.1 *Photoionization Chambers*

A photoionization chamber is a device used to measure flux intensity within a specific spectral band, consisting of a chamber of gas, a window to admit flux, and an applied voltage across two electrodes in contact with the gas. A cross section of the photometers used is shown in Figure 4.1, where a voltage would be applied between the pin electrode and the outer shell.

A photon of sufficient energy will pass through the window into the chamber, collide with a gas molecule, causing the release of an electron, thus ionizing the molecule. The ionized gas molecule is then attracted to the negative electrode, which is the center pin, and the free electron drifts to the positive electrode, which is the outer shell, producing a current flow in the photometer. The resulting current is proportional to the number of photoionized molecules, which is proportional to the number of incoming photons, which gives a linear relationship between current and flux intensity. Therefore, when calibrated, a current measurement gives the intensity of solar radiation entering the chamber.

The upper and lower limits of the spectral band of a detector are determined by the ionization potential of the gas and the filter characteristics of the window, respectively. Nitric oxide, the gas fill used in the photometers, has an ionization potential of 9.25 eV, which implies that an incoming photon must have at least 9.25 eV of energy to photoionize a gas molecule. This gives an upper wavelength limit of 135 nm. The window material, magnesium flouride, will pass wavelengths of 112 nm or greater giving a bandpass of 112 to 135 nm for the NO-MgF_2 combination.

---

*The names photometer, photoionization chamber, and photon detector will be used interchangeably.

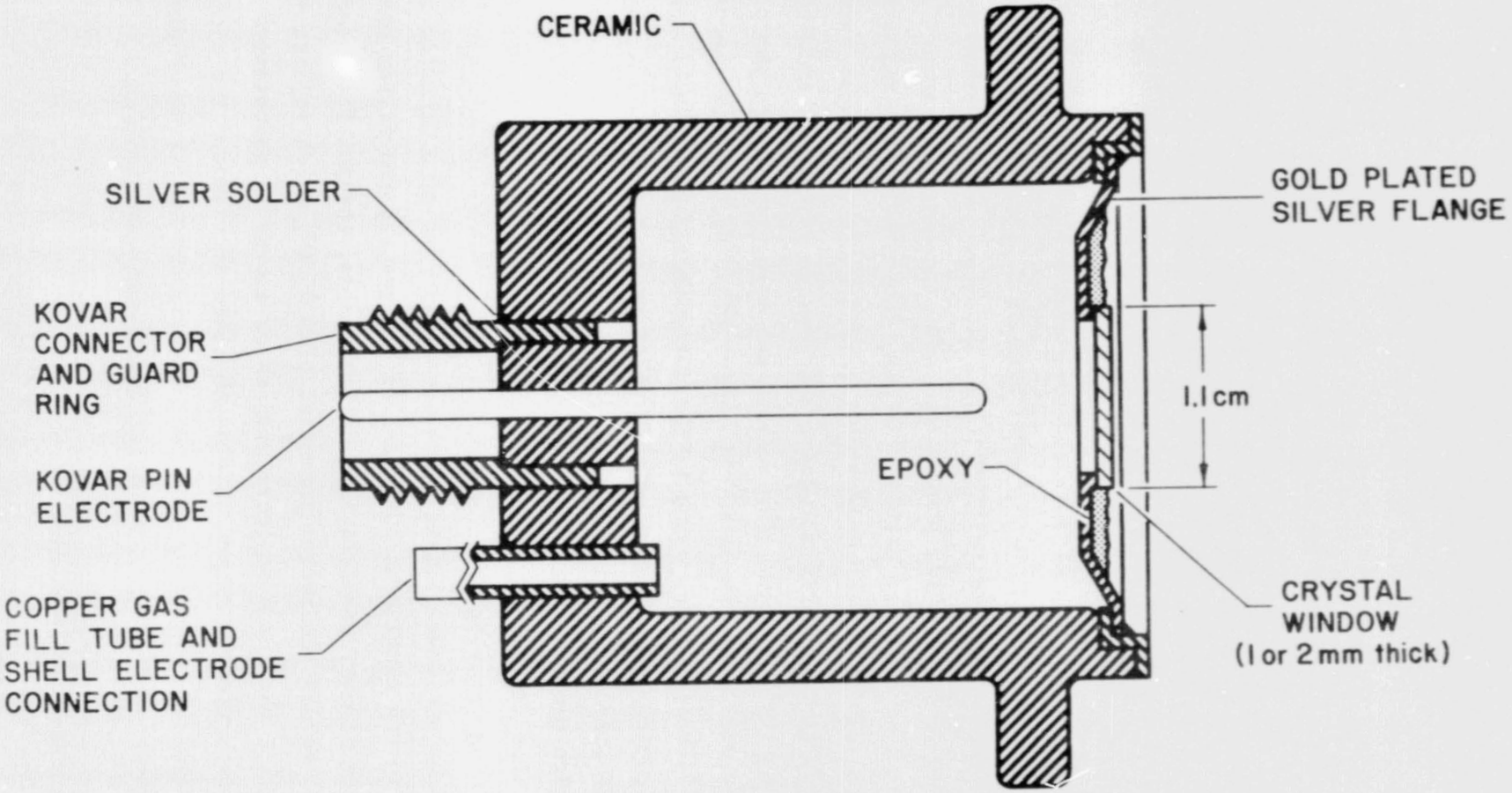

Figure 4.1 Cross section of ultraviolet radiation ion chamber [*Evans and Smith*, 1975].

The NO-MgF_2 detector was chosen because of its narrow bandwidth around the Lyman-α line (121.6 nm), giving discrimination against unwanted wavelengths and for the desirable non-hygroscopic qualities of the MgF_2 window.

4.2 *Electronic Circuits*

The instrumentation that will be referred to as the Lyman-α electronics consists of one photo-ionization chamber, two stages of amplification, and an in-flight calibration circuit. A block diagram of the Lyman-α electronics is given in Figure 4.2. As indicated in the figure, the photometers have a nominal quantum efficiency of 60 percent at Lyman-α. This quantum efficiency indicates that 60 percent of the incoming Lyman-α photons will ionize gas molecules within the photo-ionization chamber. Since each ionization of a gas molecule results in a released electron, the quantum efficiency can be used to derive the sensitivity of the photometer.

In response to an incoming flux of 1 photon s^{-1}, a photometer with a quantum efficiency of 60 percent would produce the current given by,

$$I_\alpha = (1 \text{ photon } s^{-1})(0.6 \text{ electron/photon})(1.60 \times 10^{-19} \text{ C/electron})$$
$$= 10^{-19} \text{ C } s^{-1} = 10^{-10} \text{ nA}$$

Therefore, this photometer would have a sensitivity of $S_p = 10^{-10}$ nA/(photon·s) The quantum efficiencies (as measured by the manufacturer) and corresponding photometer sensitivities for the six photo-ionization chambers of the present experiment, are given in Table 4.1.

The current from the photometer is fed into the first stage of amplification which is provided by the electrometer. The electrometer is a specialized operational amplifier designed for the measurement of extremely small currents. It is configured as a linear current-to-voltage converter with nominal sensitivities of 0.25 V/nA and 2.5 V/nA for the pre-eclipse and eclipse flights, respectively.

The second stage of amplification, the buffer amplifier, provides isolation of the electrometer and also supplies current drive to the telemetry channel. The buffer amplifier is configured for unity gain for the pre-eclipse flight and a gain of 10 for the flights during the eclipse. Referring to Figure 4.2, the nominal overall sensitivity for the pre-eclipse electronics is,

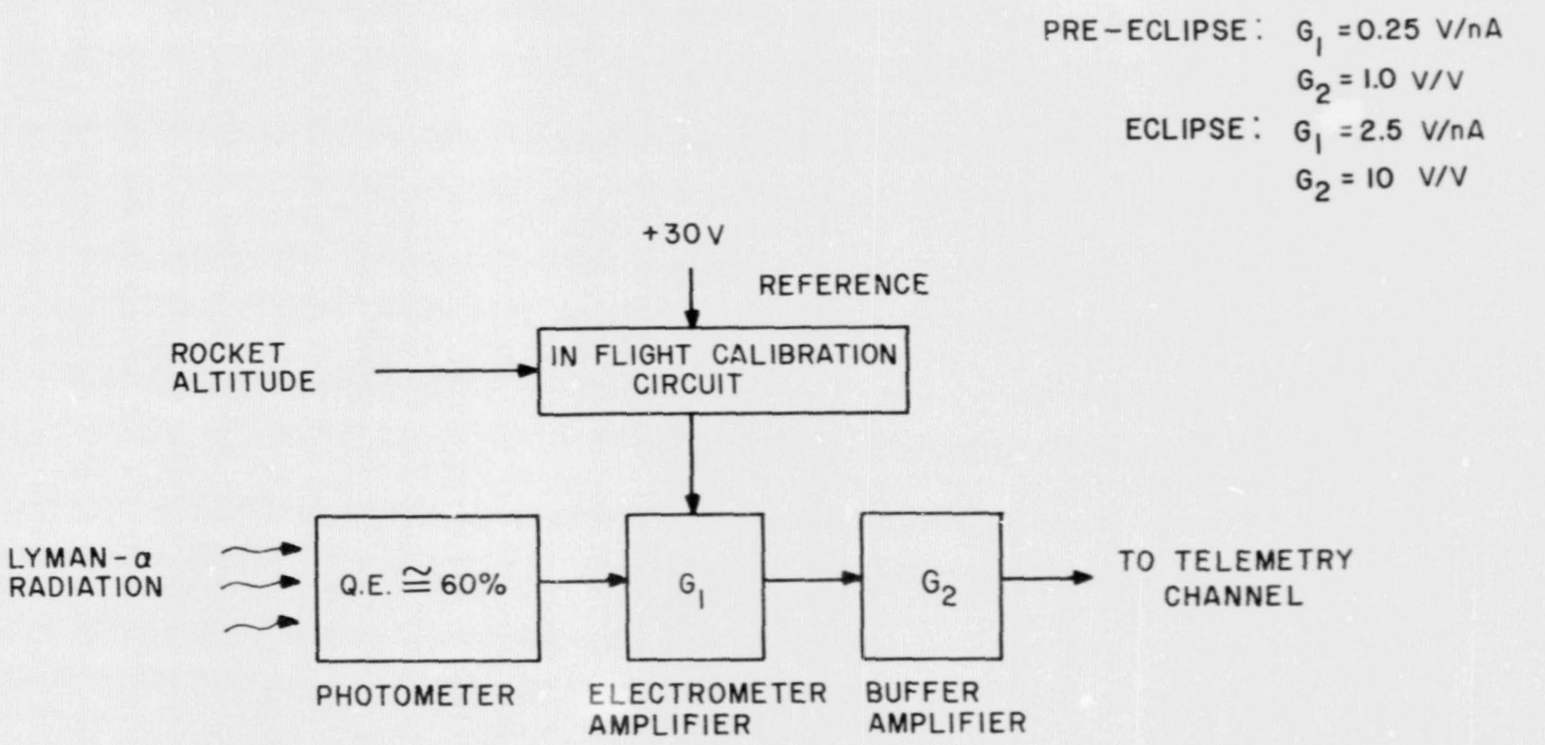

Figure 4.2 Block diagram of Lyman-α electronics.

Table 4.1 Sensitivities of Lyman-α instrumentation (U = uncollimated and C = collimated).

	Q.E./100	$S_p \times 10^{21}$	$I_{FS} \times 10^{9}$	$S_\alpha \times 10^{12}$
18.1020 U	0.591	0.946	19.4	0.244
18.1020 C	0.621	0.994	20.2	0.246
18.1021 U	0.536	0.858	0.208	20.6
18.1021 C	0.678	1.08	0.208	26.0
18.1022 U	0.610	0.976	0.205	23.8
18.1022 C	0.640	1.02	0.188	27.1

$$\text{Q.E.} = \frac{\text{quantum efficiency of photometer}}{\text{as specified by the manufacturer}}$$

$S_p \triangleq$ sensitivity of photometer

$$= \frac{(\text{Q.E./100 e/photon})(1.60 \times 10^{-19}\ \text{coul/e})\ (1\ \text{photon s}^{-1})}{(1\ \text{photon s}^{-1})}$$

$$= (\text{Q.E./100})(1.60 \times 10^{-21})\ \text{A/photon} \cdot \text{s}^{-1}$$

$S_\alpha \triangleq$ overall sensitivity of Lyman-α electronics (including detector)

$$= \left(S_p \ \frac{\text{A}}{\text{photon} \cdot \text{s}^{-1}}\right)\left(\frac{5\ \text{Volts}}{I_{FS}\ \text{A}}\right)$$

$$= \left(\frac{5\ S_p}{I_{FS}}\right) \frac{\text{Volts}}{\text{photon} \cdot \text{s}^{-1}}$$

$I_{FS} \triangleq$ full scale input current

$$S_\alpha = S_p \times G_1 \times G_2$$
$$= [10^{-10} \text{ nA/(photon·s)}](0.25 \text{ V/nA})(1 \text{ V/V})$$
$$= 2.5 \times 10^{-11} \text{ V/(photon·s)}$$

Also, derived in the same manner, the nominal overall sensitivity for the eclipse flight is 2.5×10^{-9} V/(photon·s), which is 100 times greater to detect the reduced Lyman-α intensity of eclipse conditions. Since the circuitry is designed to provide a 5 V maximum signal at the output of the buffer amplifier, the instrumentation has the capability to measure Lyman-α intensity up to 2×10^{11} photons s^{-1} for the pre-eclipse payload and 2×10^{9} photons s^{-1} for the eclipse payload. Actual overall sensitivities and full scale currents for the six Lyman-α detectors can be found in Table 4.1.

An in-flight calibration circuit provides a reference current to the electrometer producing a 5 V buffer amplifier output from 40 km to 70 km using altitude-sensitive switches (baroswitches).

A detailed circuit diagram of the Lyman-α electronics and associated circuitry is shown in Figure 4.3. Determination of the component values marked "select" is discussed in Section 4.4. The 89.6 V bias voltage for the photometer is provided by four 22.4 V batteries (Mallory RM 412) connected in series. The Keithley 302 electrometer is chosen for its high input resistance of 10^{12} ohms and desirable stability characteristics. Manufacturer's specifications for the Keithley 302 are given in Table 4.2. Diode protection is used on the input of the 741 operational amplifier as a safeguard against any large transients which may occur during the flight, and at the output to prevent a negative signal into the telemetry channel. The MC7814/MC7915 voltage regulators provide ±15 V using the ±30 V busses as power sources.

4.3 *Frequency Response*

The total Lyman-α waveform delivered to the telemetry channel is dependent upon the angular sensitivity of the detector, the spin rate of the payload, as well as the frequency response of the circuits. As already mentioned in the introduction, each payload carries two photometers used together for determining rocket aspect and for measuring Lyman-α flux. The details of the arrangement will be given later in this chapter but, for now,

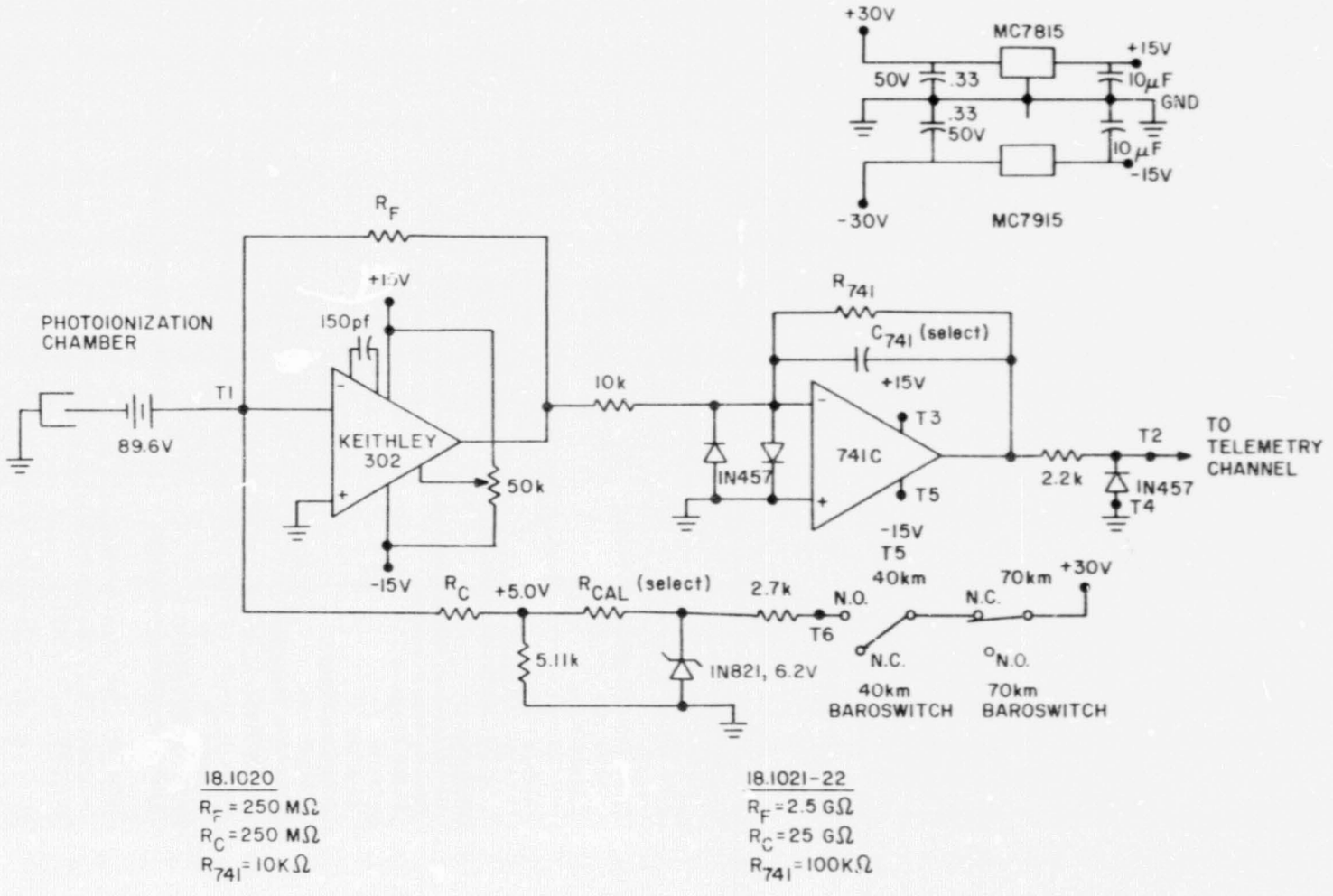

18.1020
R_F = 250 MΩ
R_C = 250 MΩ
R_{741} = 10KΩ

18.1021-22
R_F = 2.5 GΩ
R_C = 25 GΩ
R_{741} = 100KΩ

Figure 4.3 Circuit details of the Lyman-α electronics.

Table 4.2 Specifications for the Keithley Model 302.

Specifications measured at 25°C.	MODEL 302
DC VOLTAGE GAIN, OPEN LOOP:	
Unloaded (Minimum)	12,000
Full Load (Minimum)	10,000
INPUT CHARACTERISTICS:	
Common Mode	
Resistance (Minimum)	—
Shunt Capacitance (Maximum)	—
Rejection (Minimum)	—
Voltage Limit	—
Between Inputs	
Resistance (Minimum)	10^{12} ohms
Shunt Capacitance (Maximum)	5 picofarads
Overload Limit	±100 volts continuous ±400 volts momentary
Current Stability	
Offset	10^{-14} ampere
vs. Time (worst case)	10^{-15} ampere/24 hours
vs. Temperature (worst case)	Doubles every 5°C
vs. Supply (worst case)	$5x10^{-15}$ ampere /%
Voltage Stability	
Offset	Adjustable to zero
vs. Time (worst case)	2 millivolts/week after 1-hour warm-up
vs. Temperature (worst case)	150 microvolts/°C
vs. Supply (worst case)	1 millivolt/%
Current Noise	
0.1-10 cps (Maximum peak-to-peak	$5x10^{-15}$ ampere
Voltage Noise	
0.1-10 cps (Maximum rms)	10 microvolts
10 cps—500 kc (Maximum rms)	100 microvolts
FREQUENCY:	
Gain Bandwidth Product (Minimum)	150 kc
Slewing Rate (Minimum)	0.1 volt/microsecond
Rolloff (Nominal)	6 db/octave
OUTPUT:	
Amplifier	±10 volts @ 5 milliamperes
Reference Voltage	—
Regulation	—
OPERATING TEMPERATURE:	−0°C to +50°C
CONNECTORS:	
Input	Teflon-insulated feed through
All Other	#20 pins 0.2" long, 0.2" grid
POWER REQUIREMENTS:	
Voltage (positive and negative)	15 volts regulated ±0.1%
+Current (Plus output current)	5 milliamperes
−Current (Plus output current)	5 milliamperes
DIMENSIONS; WEIGHT:	1" high x 1" wide x 9/16" deep; ½ ounce

we need only note that one detector is collimated and the other is not. The angular variation of the uncollimated detector is expected to approach a $(\text{cosine})^2$ function while the collimated detector is expected to have a nearly triangular variation with angle. Figure 4.4 shows idealized waveforms from a collimated and an uncollimated detector, respectively. Due to the spinning motion of the payload, these waveforms are periodic with a period $T = 1/(\text{spin rate})$.

Since an accurate measurement of the peak amplitude of the signals is necessary in the final analysis, the frequency response of the Lyman-α electronics must be considered to determine if any reduction of the signal amplitude will be introduced by the Lyman-α circuit. Referring to Figure 4.3, consider the Lyman-α electronics with the frequency compensation capacitor, C_{741}, removed. The circuit is essentially two cascaded operational amplifiers. A first-order approximation to the transfer function for an op-amp with feedback will be derived. Consider the op-amp configuration in Figure 4.5 where R_1 and R_2 are resisters and C_{eff} is the effective capacitance in the feedback path introduced by the physical layout and the op-amp. Summing current at node a gives,

$$\frac{v_i - v_a}{R_2} = \frac{v_o - v_a}{R_1 \| C_{\text{eff}}} \tag{4.1}$$

where v_a is the voltage at node a. Using an ideal op-amp approximation, the following equation is also true,

$$v_a = \lim_{A \to \infty} \left(\frac{v_o}{A} \right) = 0 \tag{4.2}$$

Combining equations (4.1) and (4.2) gives the following transfer function,

$$\frac{v_o}{v_i} = \frac{R_1 \| C_{\text{eff}}}{R_C} = \frac{R_1}{R_e} \left(\frac{1}{1 + j\omega R_1 C_{\text{eff}}} \right) \tag{4.3}$$

which has a single-pole roll-off at $\omega_{3\text{dB}} = 1/R_1 C_{\text{eff}}$. Since the Keithley 302 inherently has a much lower gain-bandwidth-product than the 741C and considering their relative gains, it will be assumed that the frequency response of the entire circuit is that of the Keithley 302 (multiplied by a factor of 10 for the eclipse electronics) and, furthermore, it will be assumed that the response of the Keithley 302 is characterized by the

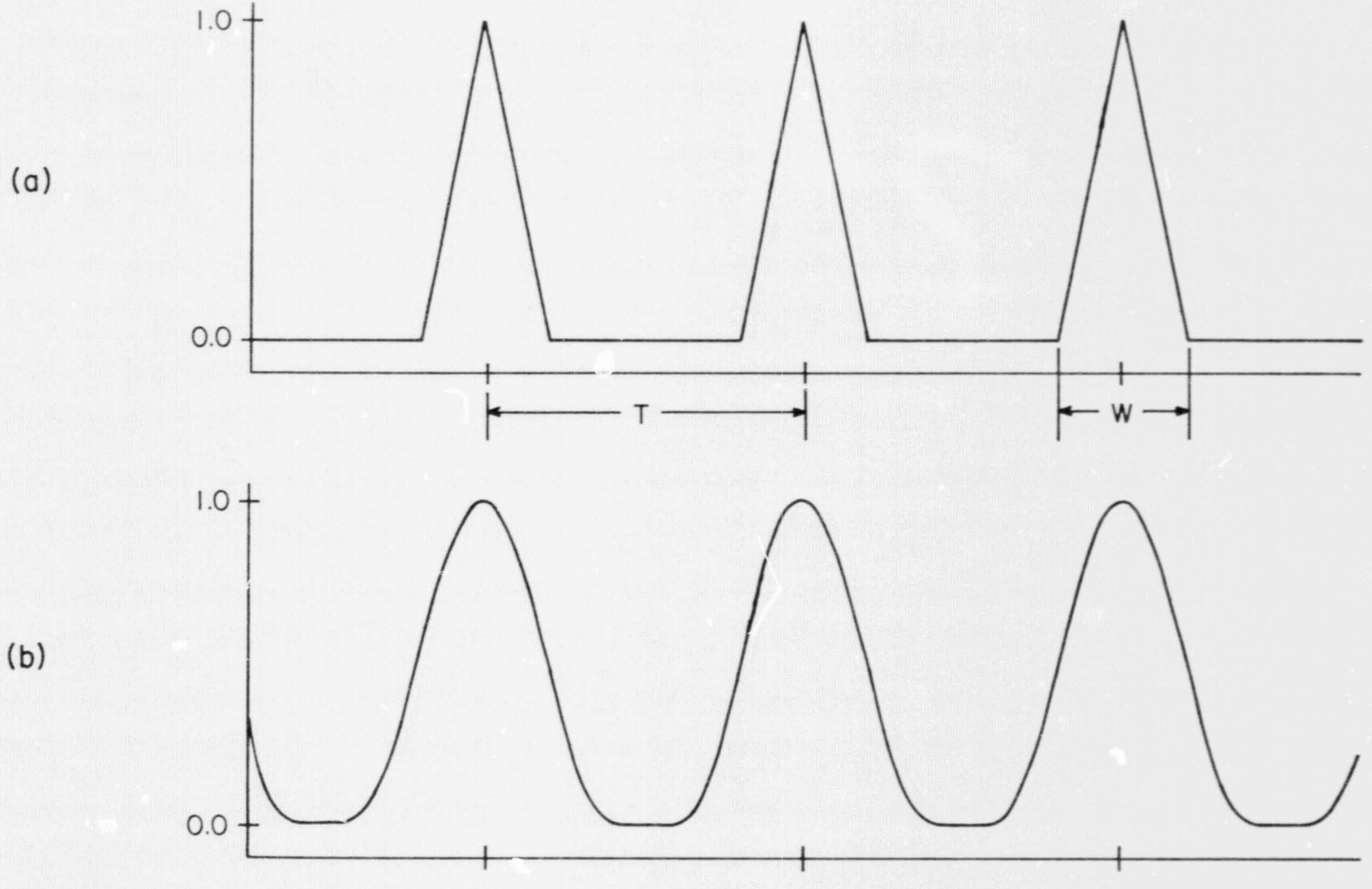

Figure 4.4 Idealized waveforms for (a) collimated detector, and (b) uncollimated detector.

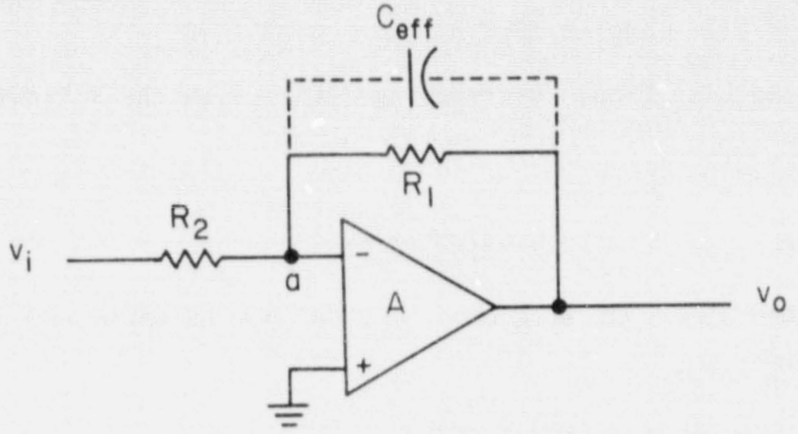

Figure 4.5 Operational amplifier in an inverting-amplifier configuration.

transfer function in (4.3) with R_1 replaced by R_F(see Figure 4.3).

It will now be shown that by applying a step input to the Lyman-α electronics and measuring the rise time of the resulting output, a value for C_{eff} of the electrometer can be obtained thus characterizing the frequency response of the circuit. The step response of the circuit is,

$$v_o = v_i[1 - \exp(-t/R_F C_{eff})], \quad t > 0 \tag{4.4}$$

where v_i is the amplitude of the step input and v_o is the resulting output. Since rise time is defined as the time it takes for v_o to reach 0.9 v_i, the following equation must hold,

$$0.9 = [(1 - \exp(-t_R/R_F C_{eff})] \tag{4.5}$$

where t_R denotes rise time. Rearranging (4.5) gives the following expression for C_{eff},

$$C_{eff} = \frac{-t_R}{\ln(0.1)R_F} = \frac{t_R}{2.3026R_F} \tag{4.6}$$

Using (4.6), the upper 3dB frequency, f_h, can now be expressed as a function of the rise time, t_R,

$$f_h = \frac{1}{2\pi R_F C_{eff}} = \frac{2.30}{2\pi t_R} = \frac{0.366}{t_R} \tag{4.7}$$

Details of how the rise time is actually measured are given later in this chapter.

To illustrate the effects of frequency response upon the total waveform, consider the ideal collimated Lyman-α signal of Figure 4.4(a), which has the following Fourier series representation,

$$f_o(t) = \frac{W}{2T} + \sum_{k=1}^{\infty} \frac{2T}{\pi^2 k^2 W} \left(1 - \cos \frac{\pi k W}{T}\right) \left(\cos \frac{2\pi k t}{T}\right) \tag{4.8}$$

where T is the period of revolution of the payload and W is the width of the triangle pulse. In terms of the harmonic frequencies, $2\pi k/T$, of the Fourier series, and the rise time, t_R, the transfer function is given by,

$$H\left(k \frac{2\pi}{T}\right) = \left[j\left(k \frac{2\pi}{T}\right)\left(\frac{t_R}{2.3026}\right) + 1\right]^{-1} \tag{4.9}$$

which has the following magnitude and phase characteristics,

$$\left|H\left(k\,\frac{2\pi}{T}\right)\right| = \left[\left(k\,\frac{2\pi}{T}\right)^2\left(\frac{t_R}{2.3026}\right)^2 + 1\right]^{-1}$$

$$\phi\left(k\,\frac{2\pi}{T}\right) = -\tan^{-1}\left[\left(k\,\frac{2\pi}{T}\right)\left(\frac{t_R}{2.3026}\right)\right] \qquad (4.10)$$

Applying these characteristics to the triangular pulse train gives the following infinite series representation for the output,

$$f_o(t) = \frac{W}{2T} + \sum_{k=1}^{\infty}\frac{2T}{\pi^2k^2W}\left(1 - \cos\frac{\pi kW}{T}\right)\left[\left|H\left(k\,\frac{2\pi}{T}\right)\right|\right]\cos\left[k\,\frac{2\pi}{T}\,t + \phi\left(k\,\frac{2\pi}{T}\right)\right] \qquad (4.11)$$

As an example, Figure 4.6 gives a plot of the output function, $f_o(t)$, for a rise time of, t_R = 1.6 ms, a period of, T = 167 ms, and a pulse duration of, W = 40 ms, as approximated on a digital computer using the FORTRAN program titled "FOUR".* Notice that the peak values of the triangle pulses are reduced by 3.5%. Since an accurate peak value is needed for aspect information, a correction factor would be used in the final analysis for this example.

4.4 *Calibration and Testing*

The calibration and testing procedures for the Lyman-α electronics are divided into the following three categories; (1) zero offset adjustments, (2) rise-time measurements and buffer-amplifier compensation, and (3) full-scale sensitivity measurements and selection of calibration resistors. A detailed description of these procedures is given in this section, preceded by a preliminary discussion of the rise-time measurements.

To measure the rise time of the circuit a square wave of some peak-to-peak voltage, 2 V, is applied to the input and then the duration of a transition from $-VG_1G_2/R_0$ to 90% of VG_1G_2/R_0 is measured at the output, G_1G_2 is the gain of the circuit as described in Section 4.2 and R_0 is the output resistance of the square-wave generator.

---

*A listing of the program FOUR is given in Appendix I.

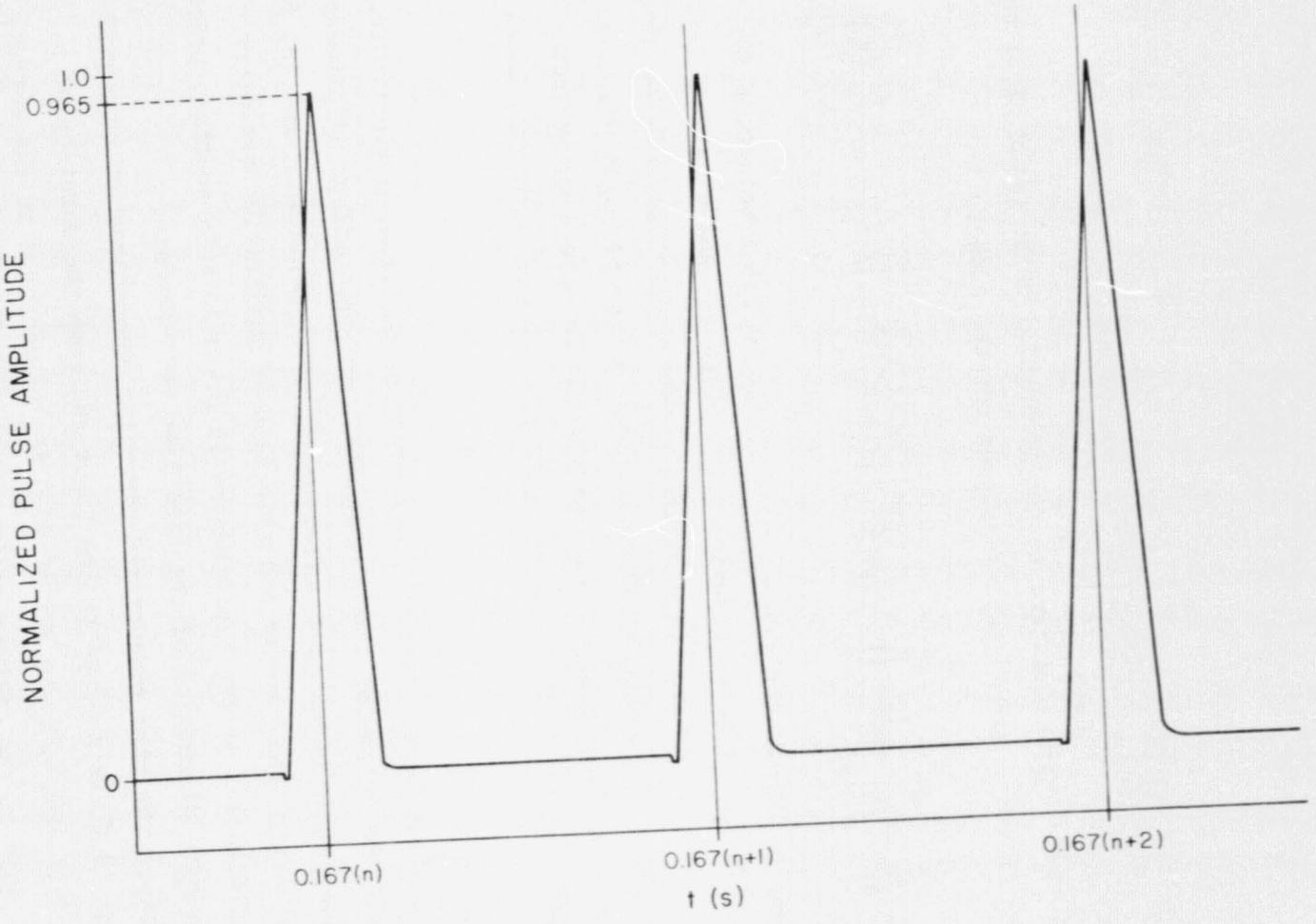

Figure 4.6 Simulated output of the Lyman-α detection circuit for an idealized collimated detector excitation function.

Assuming a circuit gain of G_1G_2 = 25 V/nA as in the two eclipse payloads and a generator output resistance of R_0 = 50 Ω, the full-scale input voltage will be determined. The input resistance of the Lyman-α electronics, which is characterized by the inverting input of the Keithley 302 electrometer, is given by,

$$R_i = R_o + \frac{R_F}{A} = 50\ \Omega + \frac{2.5 \times 10^9\ \Omega}{10^4} = 2.5 \times 10^5\ \Omega \tag{4.12}$$

where A is the open-loop gain of the electrometer and is specified by the manufacturer. The current which produces a full-scale output of 5 V is given by,

$$I_{FS} = 5\ \text{V}/G_1G_2 = 5\ \text{V}/(25\ \text{V/nA}) = 0.2\ \text{nA} \tag{4.13}$$

Therefore, to produce a full-scale swing (0 to 5 V) at the output requires an input square wave peak-to-peak amplitude given by,

$$V_{FS} = I_{FS}\, R_i = (0.2 \times 10^{-9}\ \text{A})(2.5 \times 10^5\ \Omega) = 50\ \mu\text{V} \tag{4.14}$$

which is too small of a signal to be generated by a conventional waveform generator. To produce a square wave of such a small magnitude, a triangular wave is differentiated by coupling the output of a standard waveform generator to the input of the Lyman-α circuit with a 10 pF capacitor as shown in Figure 4.7. The peak-to-peak amplitude, V_T, of a 100 Hz triangular wave which produces a 50 μV peak-to-peak square wave at the input of the Lyman-α electronics will now be determined. For positively sloped transition of the triangular wave the (displacement) current through the 10 pF capacitor is given by,

$$I_C = C\,\frac{dV}{dt} = C\,\frac{\Delta V}{\Delta t} = 2fC\Delta V \tag{4.15}$$

where f is the fundamental frequency of the triangular wave, V is the voltage across the capacitor, and I_C is the capacitor current. To produce a full-scale output of 5.0 V requires a capacitor current of

$$I_C = \frac{V_{FS}}{R_i} = I_{FS} \tag{4.16}$$

The capacitor voltage, V, in terms of the triangle wave amplitude, I_C, is given by,

$$V = V_T - V_{FS} \tag{4.17}$$

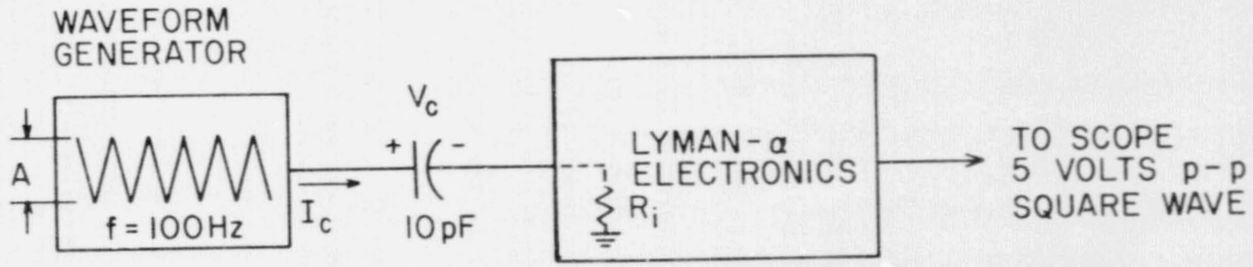

18.1020 : A ≅ 10 V p-p

18.1021/22 : A ≅ .1 V p-p

Figure 4.7 Test setup for measuring rise time.

Combining equations (4.15), (4.16), and (4.17) gives the following expression for the amplitude of the triangular wave,

$$V_T = \frac{I_{FS}}{2fC} \tag{4.18}$$

To complete the example, a peak-to-peak triangle wave amplitude of,

$$V_T = \frac{(0.2 \times 10^{-9}\ \text{A})}{2(100\ \text{Hz})(10 \times 10^{-12}\ F)} = 0.1\ \text{V} \tag{4.19}$$

would be required to produce a full-scale swing at the output of the Lyman-α electronics. This is well within the capabilities of a conventional waveform generator.

A description of the rise time measurement procedure using the above scheme for generating the small magnitude square wave is given in Table 4.3, Calibration Procedure 2. Also in Table 4.3, Calibration Procedure 1 gives the zero-offset adjustment, and Calibration Procedure 3 gives the full-scale sensitivity measurements and selection of calibration resistor. Figures 4.8 and 4.9 give the circuit details of the Lyman-α electronics and the component layout, respectively, and should be referenced when reviewing the calibration procedures. Following the calibration procedures and figures is the calibration record, Table 4.4, for flights 18.1020, 18.1021, and 18.1022.

Since each UV deck has two identical Lyman-α circuits, one for the collimated detector and one for the uncollimated detector, a circuit will be referred to as either the collimated electronics or the uncollimated electronics. Also, due to the extreme sensitivity of the electrometer amplifier to external electric fields, all measurements require the circuit shield, i.e., the aluminum case, to be in place and the hole in the bottom of the deck adjacent to the photometer mounting bracket must be covered with a grounded conductive material.

4.5 *Analysis of the Two Detector System*

Independent aspect information is not obtainable from conventional solar (or lunar) aspect sensors during the darkness of totality. However, it is possible to use two Lyman-α ion chambers, oriented differently with respect to the solar direction, to give aspect information along with corrected flux data.

Table 4.3 Calibration procedures.

Calibration Procedure 1: *Zero-Offset Adjustment*

1. Short-circuit the electrometer feedback resistor, R_F, in both the collimated and uncollimated electronics sections.
2. Connect a DVM to the collimated circuit output.
3. Adjust the 50 kΩ potentiometer of the collimated electronics to produce 0.00 V at the (collimated) output.
4. Repeat steps 2 and 3 with the uncollimated electronics.

Calibration Procedure 2: *Rise-Time Measurements and Buffer Amplifier Compensation*

1. Disconnect the cathodes of the output protection diodes of both the collimated and uncollimated electronics to allow a negative swing at the outputs.
2. Connect the test setup shown in Figures 4.7 using the uncollimated electronics keeping the 10 pF capacitor inside the circuit shield and using a shielded cable from the signal generator to the input pin.
3. Adjust the amplitude of the input triangle wave to produce a 5 V peak-to-peak square wave at the output.
4. Measure and record the rise time, which is the duration of a 0 to 90 percent positive transition of the 5 V peak-to-peak square wave.
5. Select the maximum value of C_{741} that will not cause an increase in the rise time value obtained in the previous step (being sure to turn off the circuit when changing C_{741} to avoid damaging the Keithley 302).
6. Repeat steps 2 through 5 with the uncollimated electronics.
7. Reconnect the cathodes of the output protection diodes.

Calibration Procedure 3: *Full-Scale Sensitivity Determination and Selection of Calibration Resistor*

1. Connect the test setup shown in Figure 4.9 with the collimated electronics. making sure the 1.05 GΩ calibration resistor is inside the circuit shield and using a shielded cable from the precision voltage source of the calibration resistor.
2. Adjust the precision voltage source to get 5 V at the collimated output and record the voltage.
3. Disconnect the precision voltage source.
4. Apply a voltage equal to the value of the system voltage which is approximately 30 V to the +30 V CAL input of the collimated electronics
5. Select a value for R_{CAL} to produce +5 V at the collimated output (being sure to turn off the circuit when changing R_{CAL}).
6. Repeat steps 1 through 5 with the uncollimated electronics.

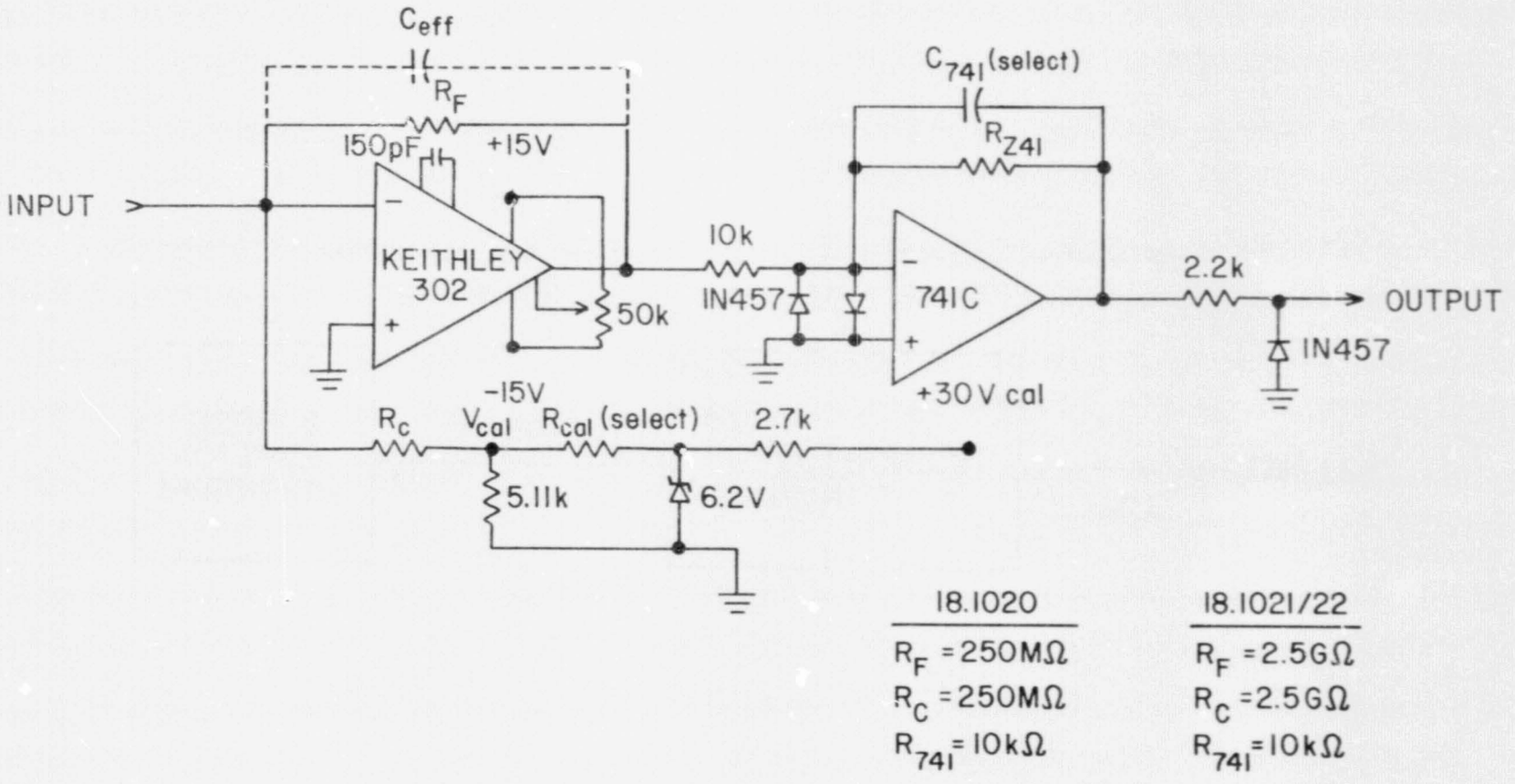

18.1020	18.1021/22
$R_F = 250M\Omega$	$R_F = 2.5G\Omega$
$R_C = 250M\Omega$	$R_C = 2.5G\Omega$
$R_{741} = 10k\Omega$	$R_{741} = 10k\Omega$

Figure 4.8 Schematic diagram of a Lyman-α electronics board.

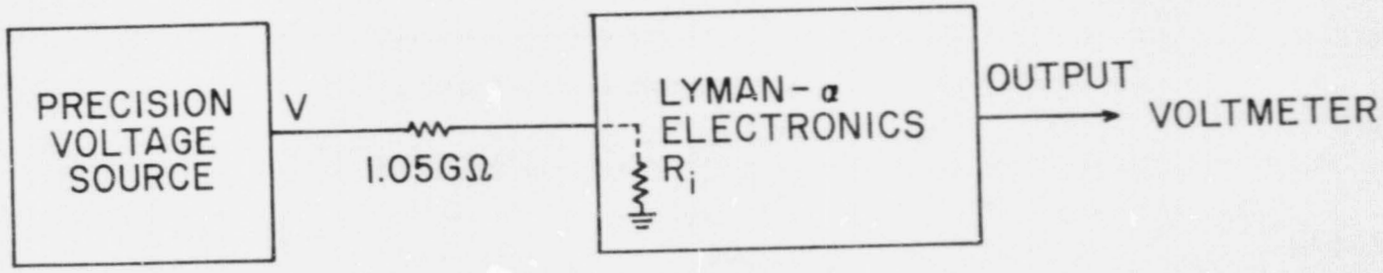

Figure 4.9 Test setup for full-scale sensitivity measurement.

Table 4.4 Calibration record for flights 18.1020, 18.1821, and 18.1022 for the collimated (C) and uncollimated (U) detectors.

	18.1020 C	18.1020 U	18.1021 C	18.1021 U	18.1022 C	18.1022 U
t_R (msec)	1.2	1.0	1.6	1.6	1.3	1.2
C_{741} (pF)	820	820	820	750	820	820
V_{FS} (V)	21.2	20.4	0.218	0.218	0.197	0.215
I_{FS} (nA)	20.2	19.4	0.208	0.208	0.188	0.205

To demonstrate this concept, consider a simple arrangement in which two ion chambers are oriented at 30° and 90° to the spin axis, as shown in Figure 4.10. For this preliminary analysis assume that the sensors have an aspect snesitivity which is represented by a cosine function.* With the sun at an angle α to the spin axis of the rocket the signals from the two detectors are,

$$I_1 = I_0 \cos(\alpha - 30°)$$
$$I_2 = I_0 \cos(90° - \alpha) = I_0 \sin \alpha \qquad (4.20)$$

where I_0 is the signal at normal incidence.**

Solving these two equations gives the angle α and I_0 in terms of the two detector outputs, I_1 and I_2,

$$\alpha = \tan^{-1}\left(\frac{\sqrt{0.75}}{I_1/I_2 - 0.5}\right) \qquad (4.21)$$

and

$$I_0 = \sqrt{\frac{4}{3}\,(I_1^{\,2} - I_1 I_2 + I_2^{\,2})} \qquad (4.22)$$

The physical system also has a maximum allowable range of values for the angle α from which I_0 can be determined. Since I_1 and I_2 are always positive the following constraints are placed on the angle α,

$$I_1 = \cos(\alpha - 30°) \geq 0 \implies -60° \leq \alpha \leq 120°$$
$$I_2 = \sin(\alpha) \geq 0 \implies 0 \leq \alpha \leq 180° \qquad (4.23)$$

thus restricting the angle α to values within the interval [0,120°].

In general, any two detector aspect detection system has a range of usable aspect angles limited by the orientation of the sensors. Referring to Figure 4.10, an increase in the allowable range of aspect angles of the example system could be facilitated by decreasing the included angle between the two detectors. As an example, if detector 2 was to remain at 90° from the spin axis, the range of usable aspect angles would be given by the interval [0, 90° + α'], where angle α' is the orientation of detector 1 and is in the interval [0, 90°]. It should be noted that a trade-off exists

---

*The actual aspect sensitivity is determined from the flight data and is discussed in section 7.3.3.

**I_0 will vary during the flight and is proportional to the solar Lyman-α radiation.

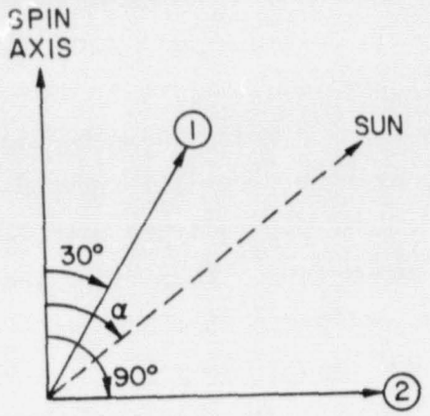

Figure 4.10 Orientation of ion chambers 1 and 2 with respect to the rocket spin axis and the sun.

between the range of usable angles and angular sensitivity of the system, i.e., to large of a range would severely decrease the resolution of this aspect detection system.

Theoretically with equations (4.21) and (4.22) and data from the two detectors, rocket aspect and solar Lyman-α intensity can be determined, respectively. However the equations were derived based on the assumption of a cosine aspect sensitivity. The actual aspect sensitivity of the detectors can be closely approximated by the function $(\text{cosine})^n$ where n is somewhere in the interval 1 to 2. The actual value of n is determined from the flight data and is discussed in section 7.3.3.

The slowly varying angular response of a detector favors an accurate flux determination but works against an accurate determination of aspect angle. To create a steeper angular variation a collimator could be added to the detector thus making it more desirable for aspect angle measurements.

The detectors in the eclipse payloads are used for the determination of both aspect angle and Lyman-α flux. Therefore, the two detector configuration chosen for the eclipse payloads consists of one detector, without a collimator, directed toward the probable direction of the sun (to be used primarily for flux determination) and the other detector, with a cylindrical collimator, directed perpendicular to the spin axis (to be used primarily for flux determination) and the other detector, with a cylindrical collimator, directed perpendicular to the spin axis (to be used for angular determination and measurement of flux from the horizon). An explanation of how the cylindrical collimator affects the angular response of the detectors will follow.

Consider a simple system consisting of a detector with a window of diameter $2a$ fitted with a cylindrical collimator of the same diameter and length ℓ, as shown in Figure 4.11. The percent area of illumination of the collimated detector surface as a function of the angle of incidence β will now be derived. From Figures 4.11 (a) and (b) it can be seen that equations (4.24) are true.

$$d = \ell \tan \beta$$
$$a \cos \phi = \frac{1}{2} d \qquad (4.24)$$

Combining these two equations gives the following definition for the angle ϕ,

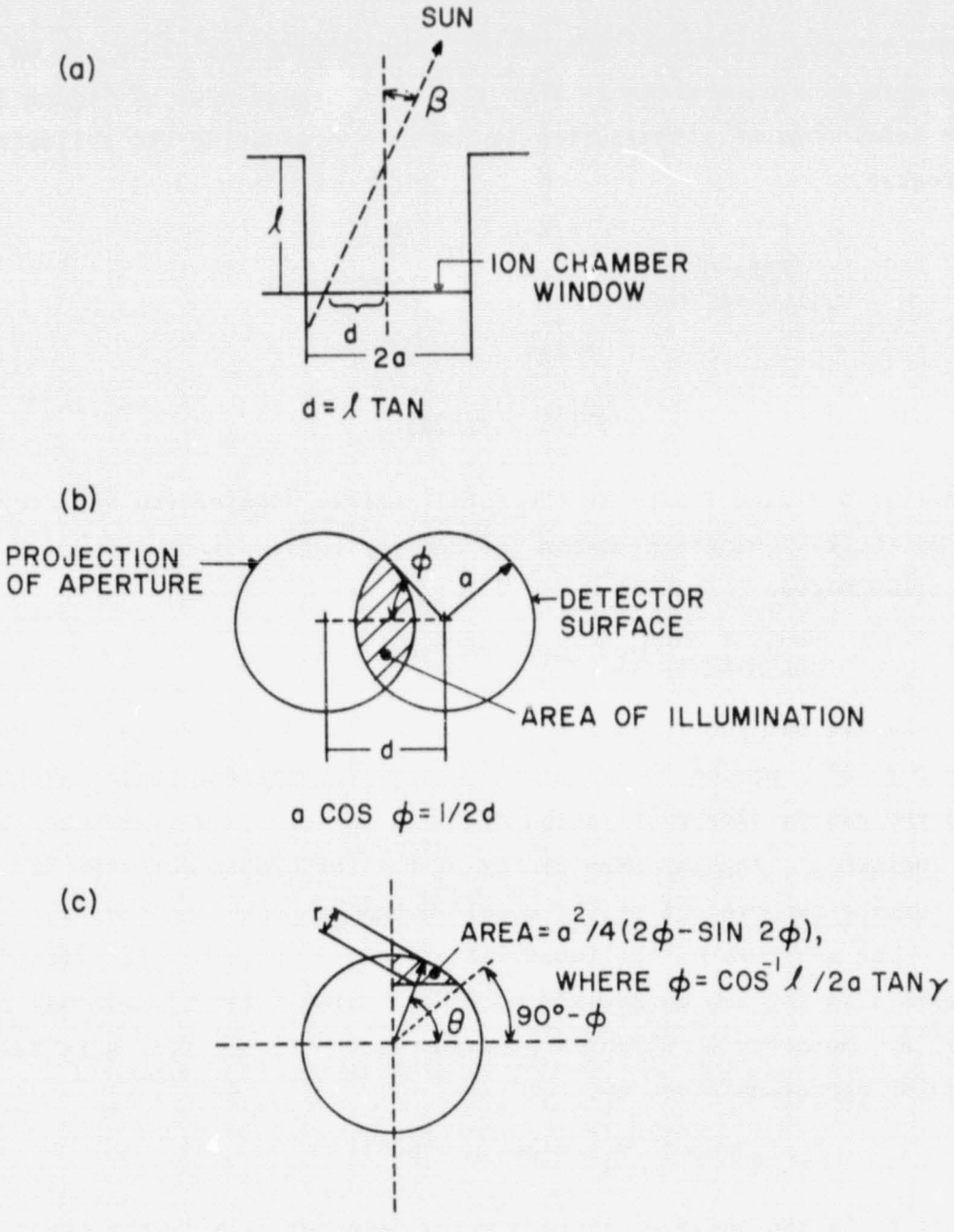

Figure 4.11 Geometry of cylindrical collimator of diameter $2a$ and depth ℓ.

$$\cos\phi = \frac{\ell}{2a}\tan\beta \quad , \quad 0 \le \phi \le \frac{\pi}{2} \tag{4.25}$$

where $\phi = \pi/2$ for normal incidence. From Figure 4.11 b it can be seen that the area of illimination is four times the shaded area of Figure 4.11 c. The total area of illumination is found by evaluating the following surface integral,

$$\text{AREA OF ILLUMINATION} = 4\int_{\pi/2-\phi}^{\pi/2}\int_{a\cos\phi/\sin\theta}^{a} r\,dr\,d\theta$$

$$= a^2(2\phi - \sin 2\phi) \tag{4.26}$$

Finally, dividing (4.26) by the total surface area of the detector, πa^2, gives the following expression for the percentage of the window surface that is illuminated.

$$\text{PERCENT AREA ILLUMINATED} = (2\phi - \sin 2\phi)/\pi \tag{4.27}$$

As an example, Figure 4.12 gives a plot of (4.27) for $\ell = 2a$ and $0 \le \beta \le 50°$. Notice that the response is cut off for angles greater than 45° and the nearly linear variation of illuminated area with respect to angle of incidence. Angular sensitivity of the collimated detector can be found by forming the product of the uncollimated response and equation (4.27).

The response of the two eclipse payload detectors is plotted in Figure 4.13 for two possible aspect angle sensitivity functions, cos β and $\cos^2\beta$. Detector 1, which is oriented at 60° to the spin axis has an angular variation given by,

$$I_1/I_0 = \cos^n(\beta_1) = \cos(\alpha - 60°) \tag{4.28}$$

where β_1 is the angle of incidence for detector 1, α is the angle of the rocket spin axis with respect to the sun, and n = 1 or 2. Detector 2, which is oriented at 90° to the spin axis, has an angular variation given by,

$$I_2/I_0 = \cos^n(\beta_2) \times \left(\text{PERCENT AREA ILLUMINATED}\right)$$

$$= \cos^n(90° - \alpha) \times (2\phi - \sin 2\phi)/\pi \tag{4.29}$$

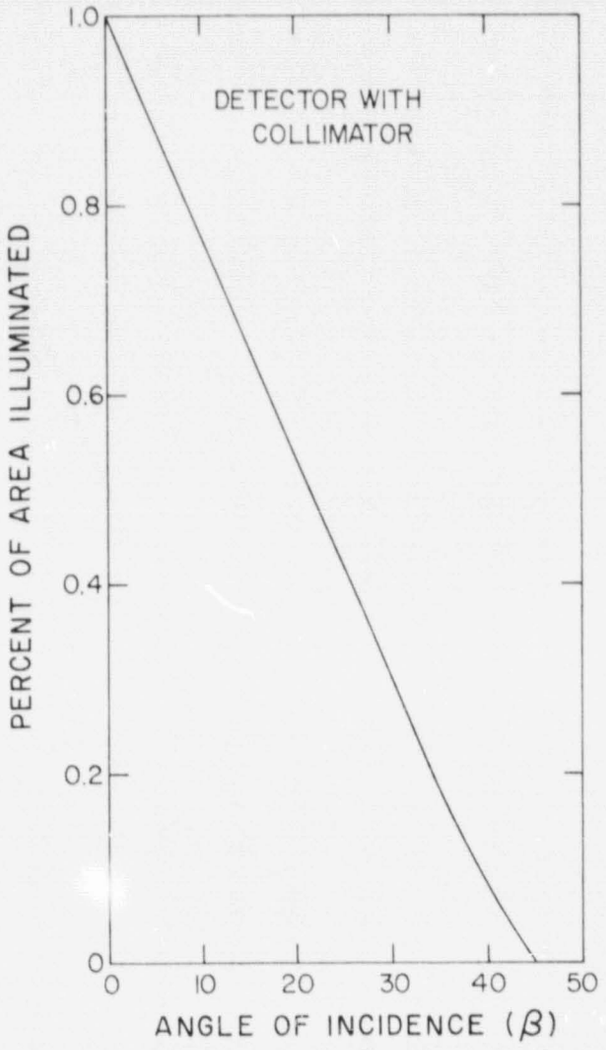

Figure 4.12 Variation of percentage of area illuminated with angle of incidence, β, for $\ell = 2a$.

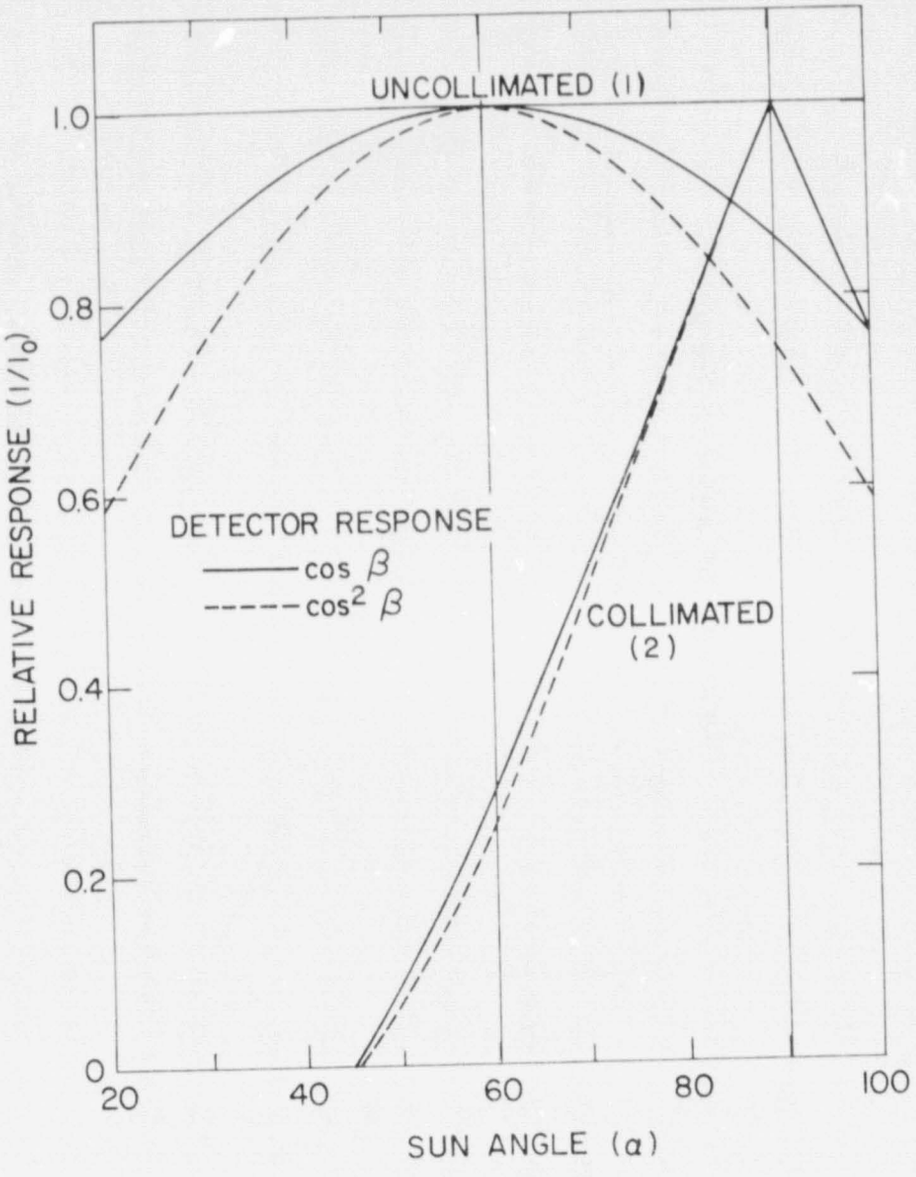

Figure 4.13 Angular response of ionization chambers with and without 45° cutoff collimator.

where β_2 is the angle of incidence for detector 2, $\phi = \cos^{-1}[\tan(90° - \alpha)]$, and $0 \leq \phi \leq \pi/2$. By examination of Figure 4.13 it can be seen that the latter variation is closely approximated by the function $(\alpha/45 - 1)$ for α in degrees and for $1 \leq n \leq 2$. This near linear response of the detector is an important outcome of using the cylindrical collimator.

For flights 18.1020, 18.1021, and 18.1022 an approximately ±5% processional motion of the payload was expected at an average sun angle of $\alpha = 65°$. From Figure 4.13 (for $n = 2$), the ratio I_2/I_1 would vary from 0.25 to 0.51 uniquely determining the sun angle throughout the flight. The final arrangement of the detectors chosen for the payloads is shown in Figure 4.14. A photograph showing a close-up of the two Lyman-α detector openings as well as the visible light sensor assembly is given in Figure 4.15.

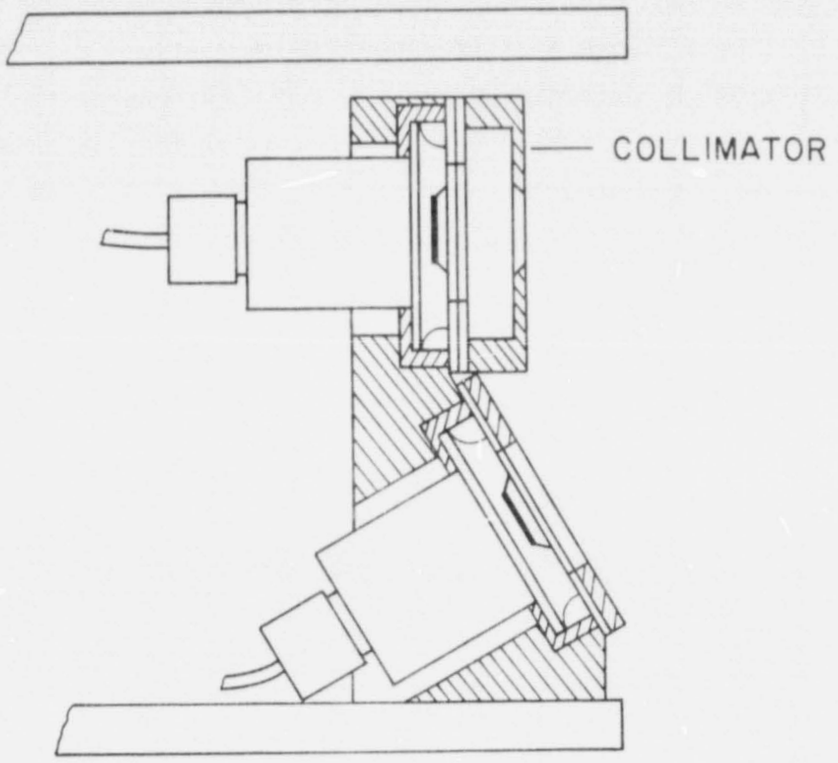

Figure 4.14 Configuration of the two Lyman-α detectors with collimated detector at 90° and uncollimated detector at 60°, with respect to the rocket spin axis. The length (ℓ) of the collimator is 1/2 in and the diameter ($2a$) is 3/8 in.

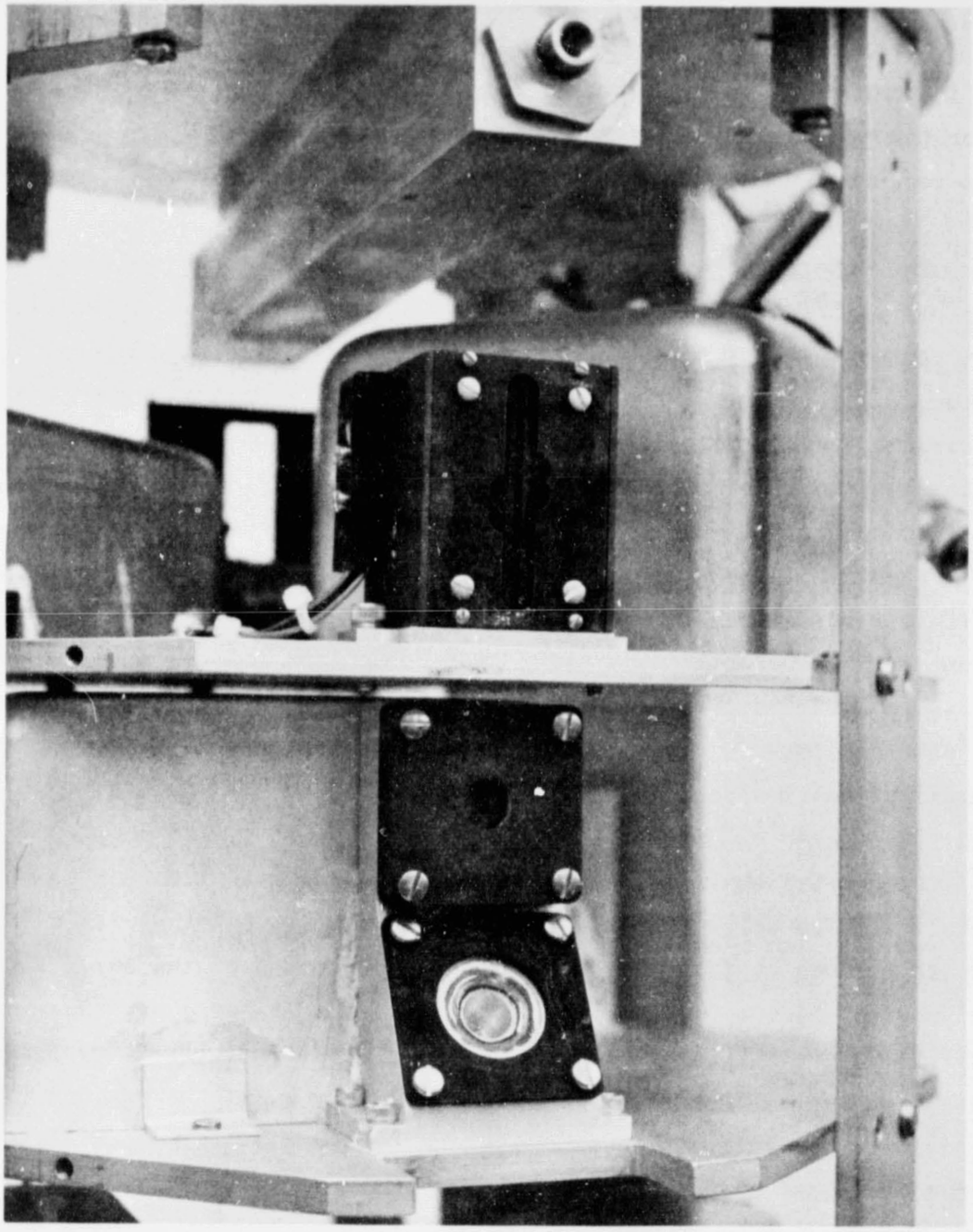

Figure 4.15 Close-up view of the payload showing the collimated, and, below it, the uncollimated Lyman-α detectors. The visible-light solar sensor is located above the two Lyman-α detectors.

5. SOLAR VISIBLE RADIATION

A visible light detection system is included in each payload to provide an indication of when the rocket enters and leaves the shadow of totality (for the two eclipse flights) and to provide a check on aspect data while the rockets are outside of the shadow.

5.1 *Sensor and Mask*

The detector consists of a solar cell, sensitive to radiation in the visible spectrum, mounted behind a back plate with a small aperature in the center which is located a fixed distance behind the face plate, as shown in Figure 5.1. The face plate is everywhere opaque except for an arrangement of a slot and four holes that can transmit visible light to the solar sensor. The solar cell signal is then amplified to not more than +5 V to maintain comparibility with the telemetry system.

Figure 5.2 shows the face plate and corresponding signals for four different rocket angles. Notice that the angles 0° and ±30° are easily identified by recognizing a group of three pulses indicating 0°, or a group of two pulses indicating ±30°. The angles 0° and 30° provide a quick check of other on-board aspect instrumentation and can be used to derive an in-flight calibration curve for the detector.

5.2 *Electronic Circuit*

Figure 5.3 shows the electronics associated with the visible radiation detector. The solar sensor transducer, SS-30, is a photo-voltaic silicon device produce by Solar System, Inc. Amplification of the solar signal is provided by the 741C operational amplifier configured as a non-inverting amplifier. Selection of the resistor marked "select" in Figure 5.3 is discussed later. The Zener diodes at the power supply inputs and the resistor-diode combination at the operational amplifier output limit the range of signal to the 0 to 5 V of the telemetry system.

5.3 *Calibration*

The calibration procedure for the visible light sensor consists of an adjustment of the amplifier gain and the generation of two calibration curves, one giving the response for varied light intensity and the other giving the output for a variation in the angle of incidence of incoming light.

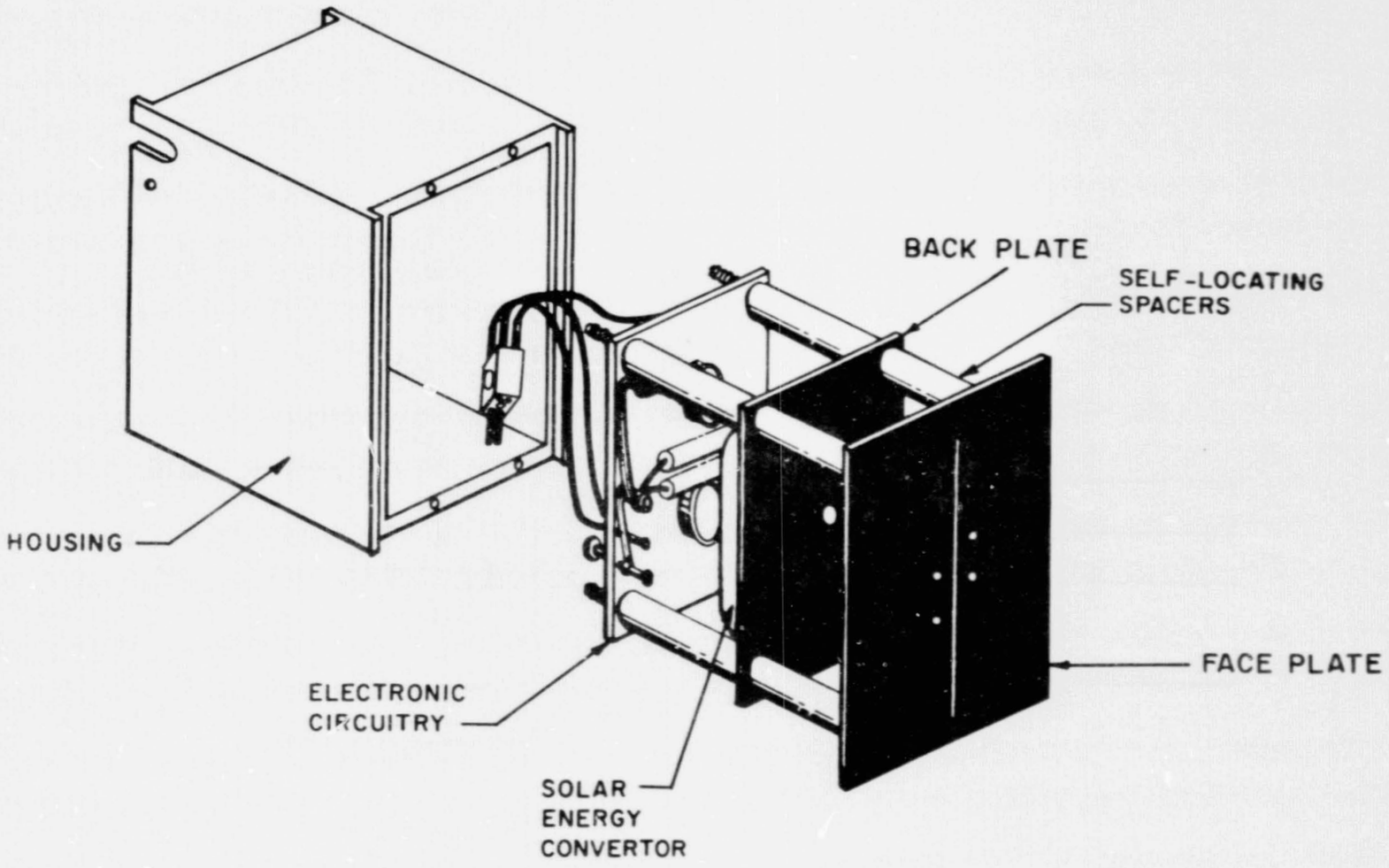

Figure 5.1 Exploded view of visible light detector.

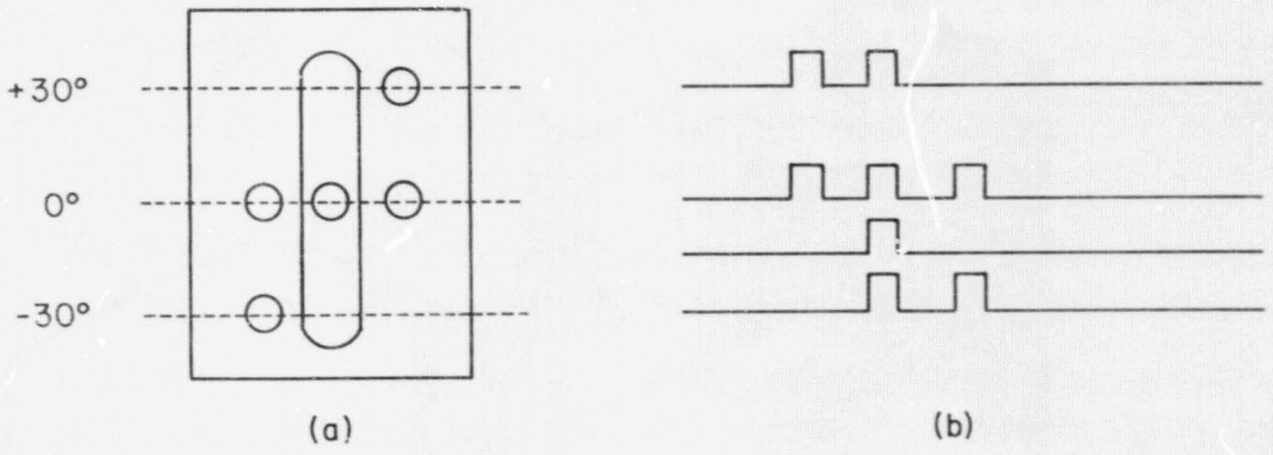

Figure 5.2 (a) Face plate of solar sensor, (b) Corresponding output signals.

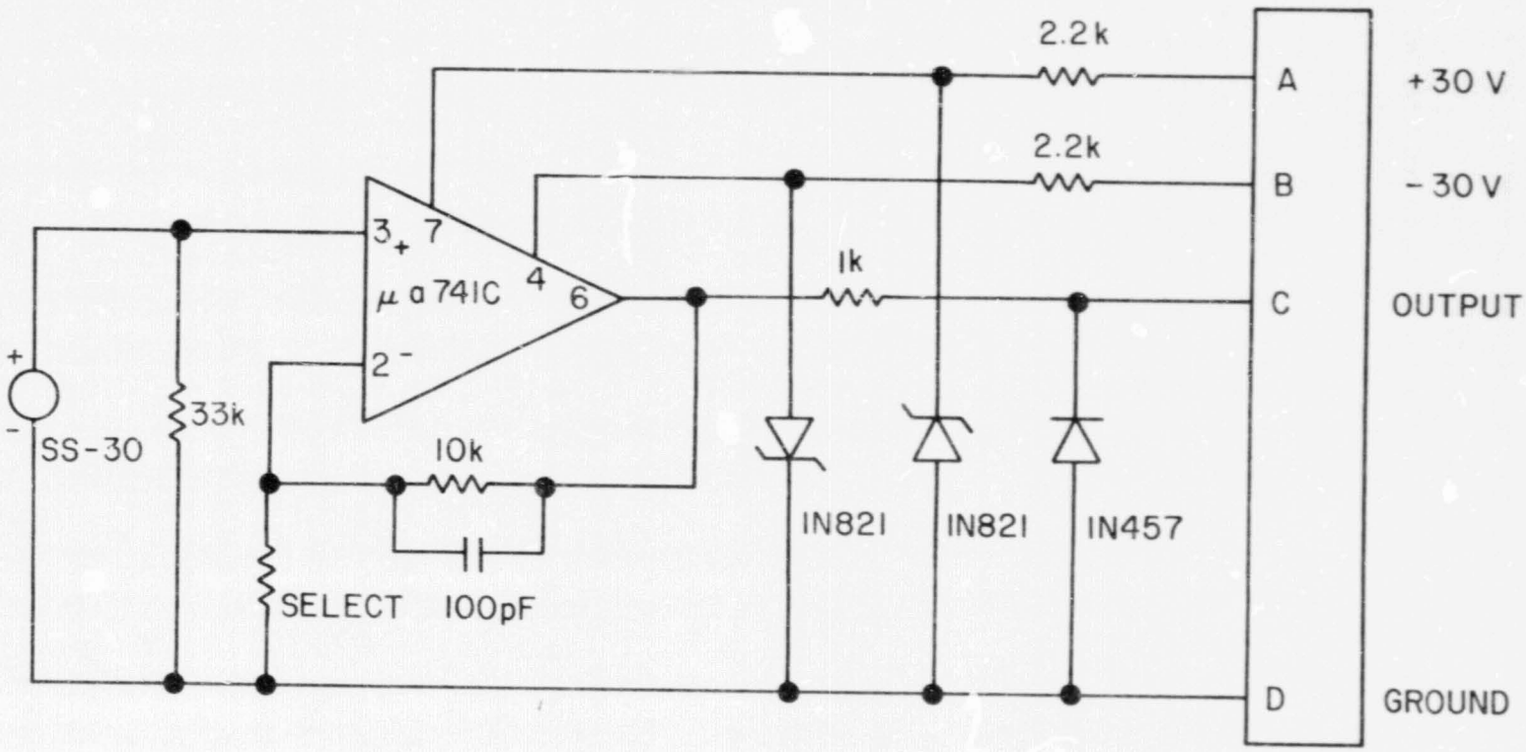

Figure 5.3 Circuit details of the visible light detection system.

The calibration setup requires a special attachment for mounting the sensor assembly to a photographic tripod, a power supply, a voltmeter, and a test source of visible light. The sun is used as the test source and therefore the calibration must be performed on a clear sunny day in a location with access to direct sunlight.

The special tripod attachment provides pre-calibrated deviation in 10° increments of the zenith angle of the detector with respect to some reference zenith angle. The reference angle for the calibration procedure is that of the sun. To put the sensor in the reference position, the tripod is first adjusted so that the veritcal slot in the faceplate is perpendicular to earth's surface using a carpenter's level as a guide. Then the reference angle is set by holding a blank sheet of paper behind the sensor assembly and fine adjusting the vertical angle of the tripod to produce as sharp as possible shadow on the plank sheet. In this position the path from the sun to the center of the faceplate should be perpendicular to the faceplate and, by definition, the rocket angle in this case would be 0°. Using the adjustment on the special tripod attachment the sensor can now be tilted in 10° increments. Once the reference position is determined, the amplifier gain adjustment and calibration measurements are performed as quickly as possible to avoid erroneous data due to the apparent movement of the sun in the sky.

With the sensor in the reference position, the amplifier gain in set by choosing the appropriate value for the resistor marked "select" in Figure 5.3. For the pre-eclipse flight the resistor is chosen to give an on-scale output for full light at normal incidence and for the two eclipse flights the resistors are chosen to give approximately 4 V output for 3.2 percent of full light at normal incidence. The following resistor values were chosen for the three payloads.

18.1020	R = 820 Ω
18.1021	R = 560 Ω
18.1022	R = 510 Ω

Once the gain is properly set, the first calibration measurements are made by placing different neutral density filters in front of the faceplate and then recording the corresponding voltage outputs. Using Kodak Wratten neutral density filters numbers 0.5, 1.0, and 2.0, data points are taken at 0.1, 0.32, 1.0, 3.2, and 10 percent transmissions. Table 5.1 gives the

Table 5.1 Relationship between filter numbers and percent transmission of the neutral density filters used in the visible light detector calibration.

Percent Transmission (T)	Filter Combination (D)
T	-log(T/100)
10^{2-D}	D
0.1	1 + 2 = 3
0.32	2 + 0.5 = 2.5
1.0	2
3.2	1 + 0.5 = 1.5
10	1
100	no filter

relationship between filter numbers and degrees of transmission for the filter combinations used in the calibration. Once the five data points (six in the case of pre-eclipse flight) are taken, they are plotted on semi-log paper. Figure 5.4 gives least-squares linear fits to the three sets of data taken for the instruments on flights 18.1020, 18.1021, and 18.1022.

The second set of calibration data, the angular variation, is taken at 1.0 percent of full sunlight and then at 0.1 percent of full sunlight. Readings are taken in pairs at 0°, ±10°, ±20°, ±30°, ±40°, ±50°, and the average of each pair is then normalized and plotted. Figures 5.5 and 5.6 give the angular variation for the three payloads for 1.0 percent and 0.1 percent of full sunlight, respectively. Notice that the sensor has a higher angular sensitivity at lower light levels.

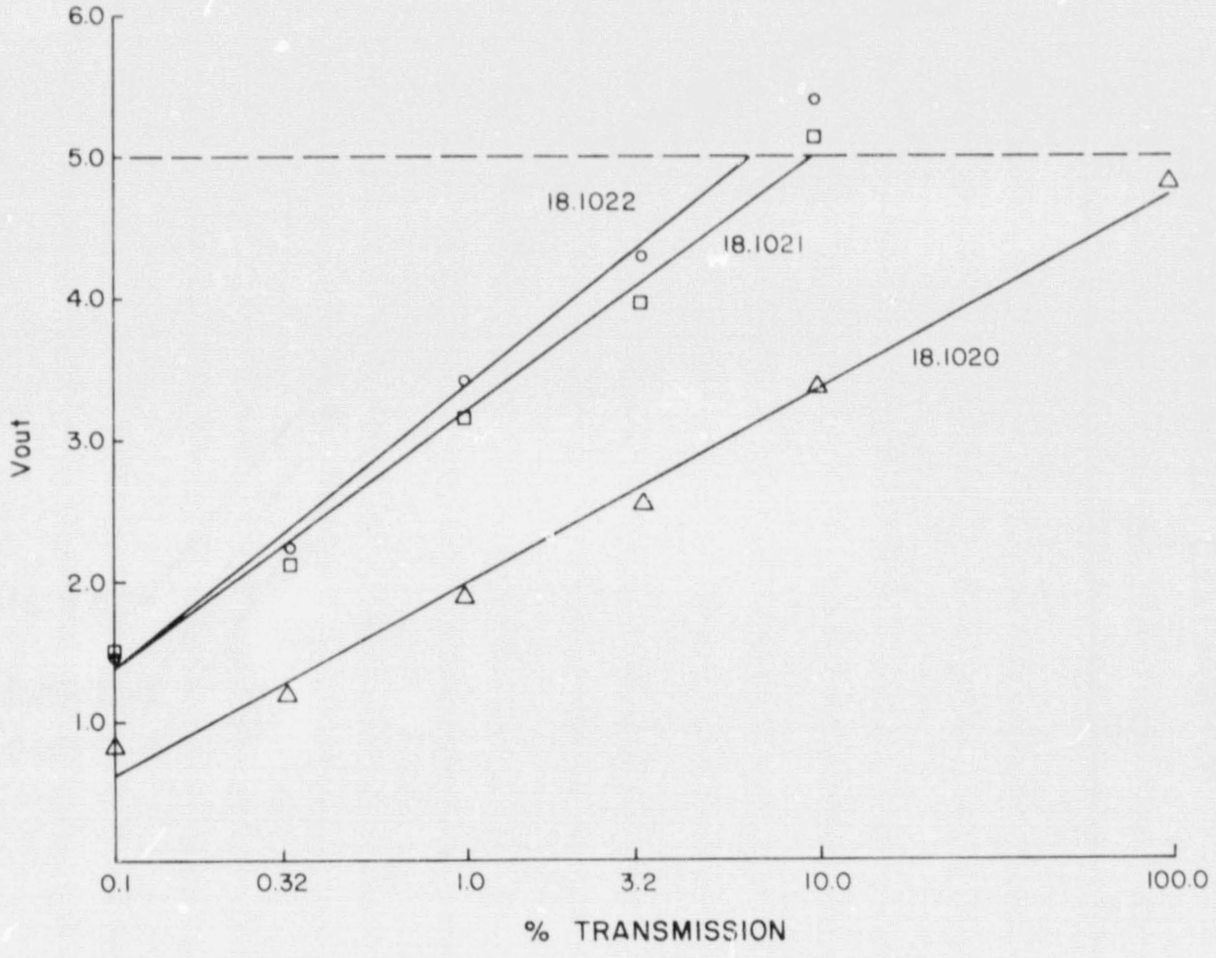

Figure 5.4 Linear fit to voltage output of visible light sensor for varied light intensity at normal incidence.

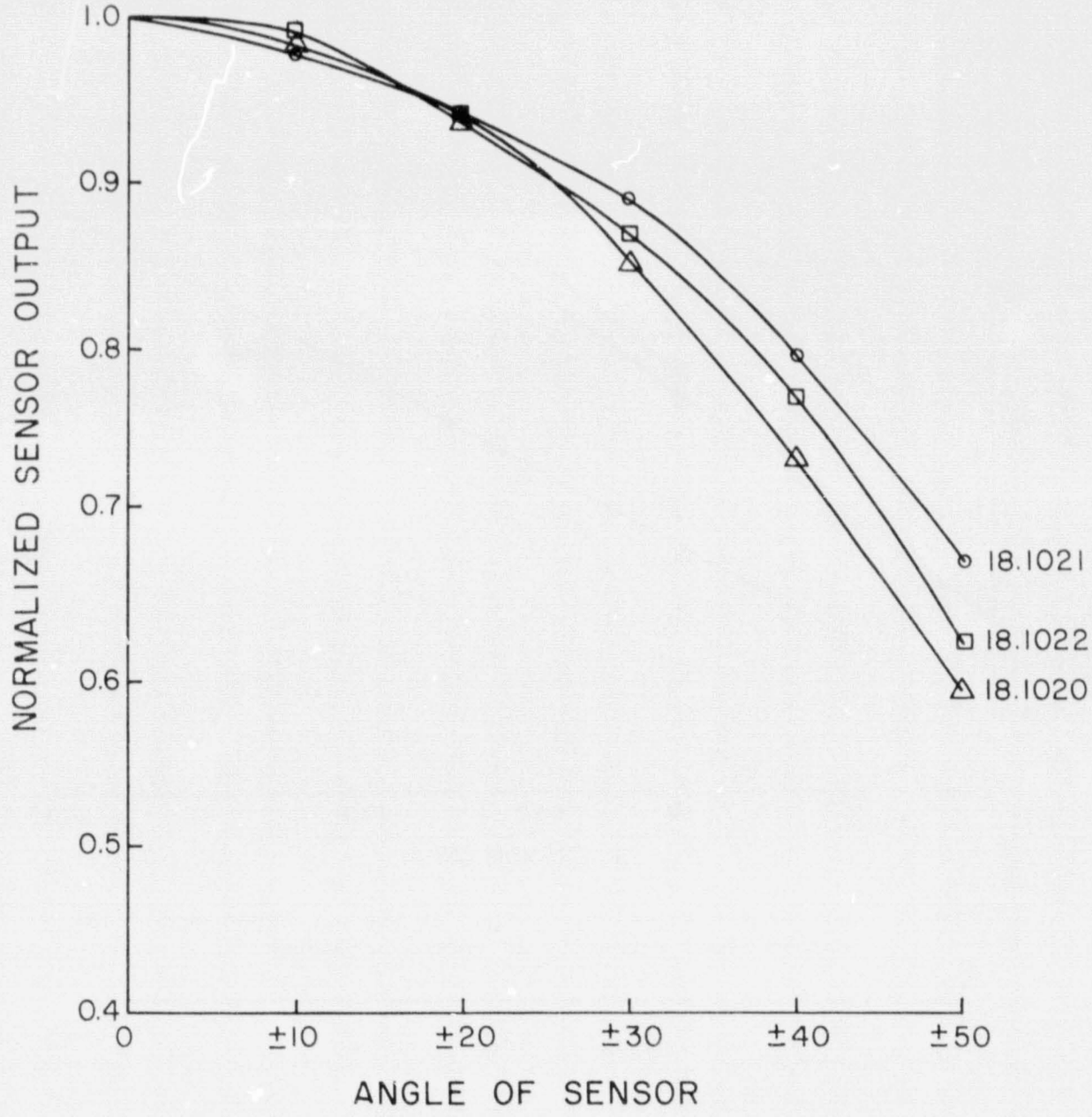

Figure 5.5 Angular variation of solar sensor for T = 1.0%.

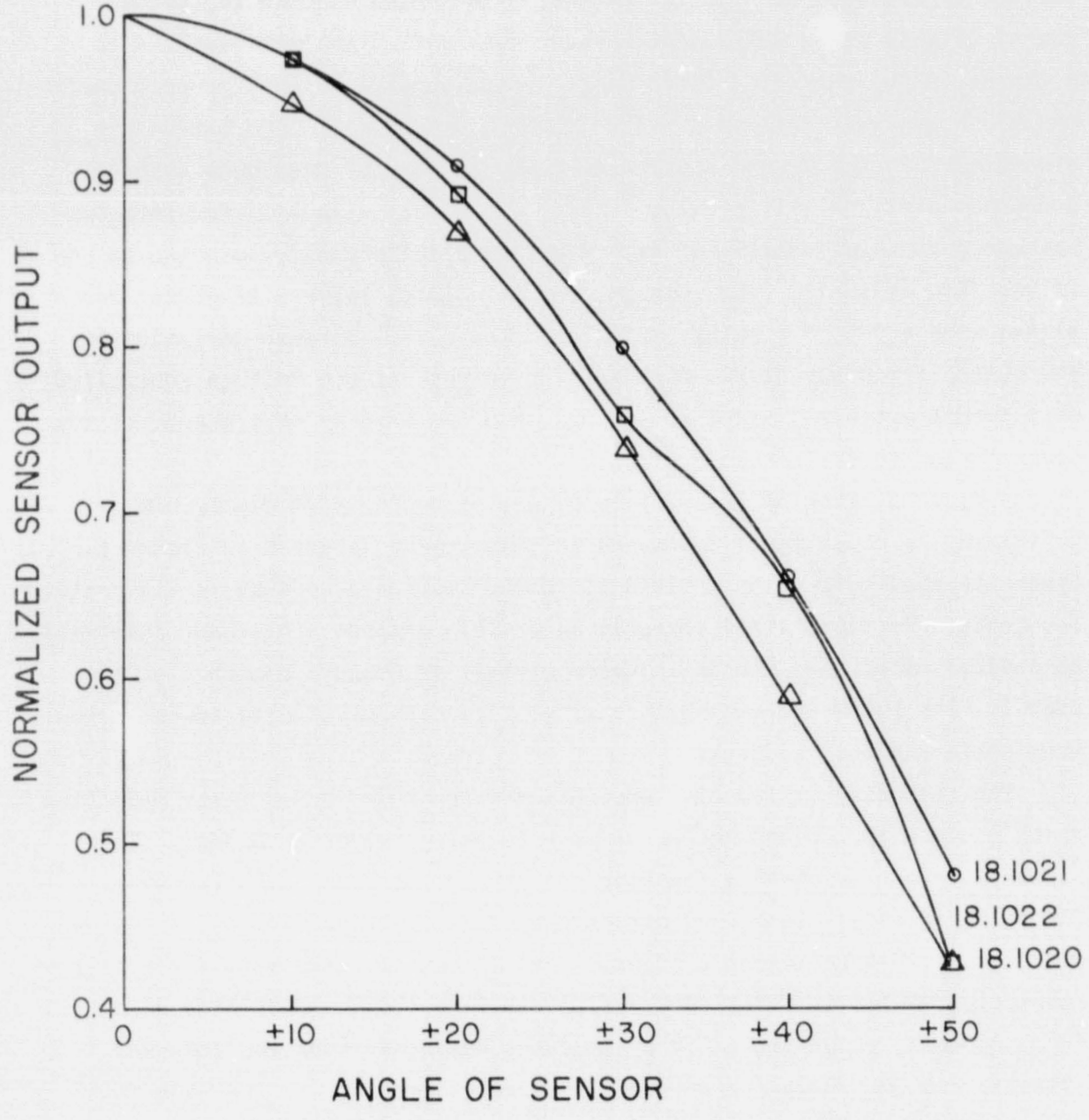

Figure 5.6 Angular variation of solar sensor for T = 0.1%.

6. PAYLOAD INTEGRATION

6.1 *Telemetry System*

The telemetry system of the payload is used to relay data from the various experiments down to the ground. The system used in the present rocket flights is an FM/FM system where each data signal is assigned to a channel using the IRIG (Inter Range Instrumentation Group) proportional bandwidth system. With this system sixteen channels of information are transmitted to the ground station on a single carrier frequency using a frequency division multiplexing scheme. Each data signal is fed into a voltage controlled oscillator with a center frequency corresponding to one of the IRIG channels. The voltage controlled oscillator will accept a signal with a 0 to 5 V swing, which produces a ±7.5 percent deviation of the center frequency at the output. The outputs of the voltage controlled oscillators are mixed together and are then fed into an FM transmitter for transmission to the ground station.

A block diagram of the portion of the on board telemetry system pertaining to experiments discussed in this report is given in Figure 6.1. Since the bandwidth of an individual channel varies according to its center frequency, the signals are transmitted on IRIG channels that have information bendwidths wider than the anticipated highest frequency component of the signal. The FM/FM system provides simple and economical data transmission from small sounding rockets.

The telemetry system also encompasses the ground based instrumentation which is used to recieve and record the incoming telemetry signal. The signal is picked up with a tracking antenna and fed into a FM receiver. The receiver output is stored directly on magnetic tape along with a time code and a 100 kHz reference signal. Provisions are also made for real-time inspection of the incoming data during the flight. The real-time signal is decoded, using phase-locked loop frequency discriminators and low-pass filters, and is presented on a chart record together with the time code. A block diagram of the ground based instrumentation is given in Figure 6.2. The oscilliscope and the chart recorder are used to monitor the operation of the experiments while the rocket is in flight.

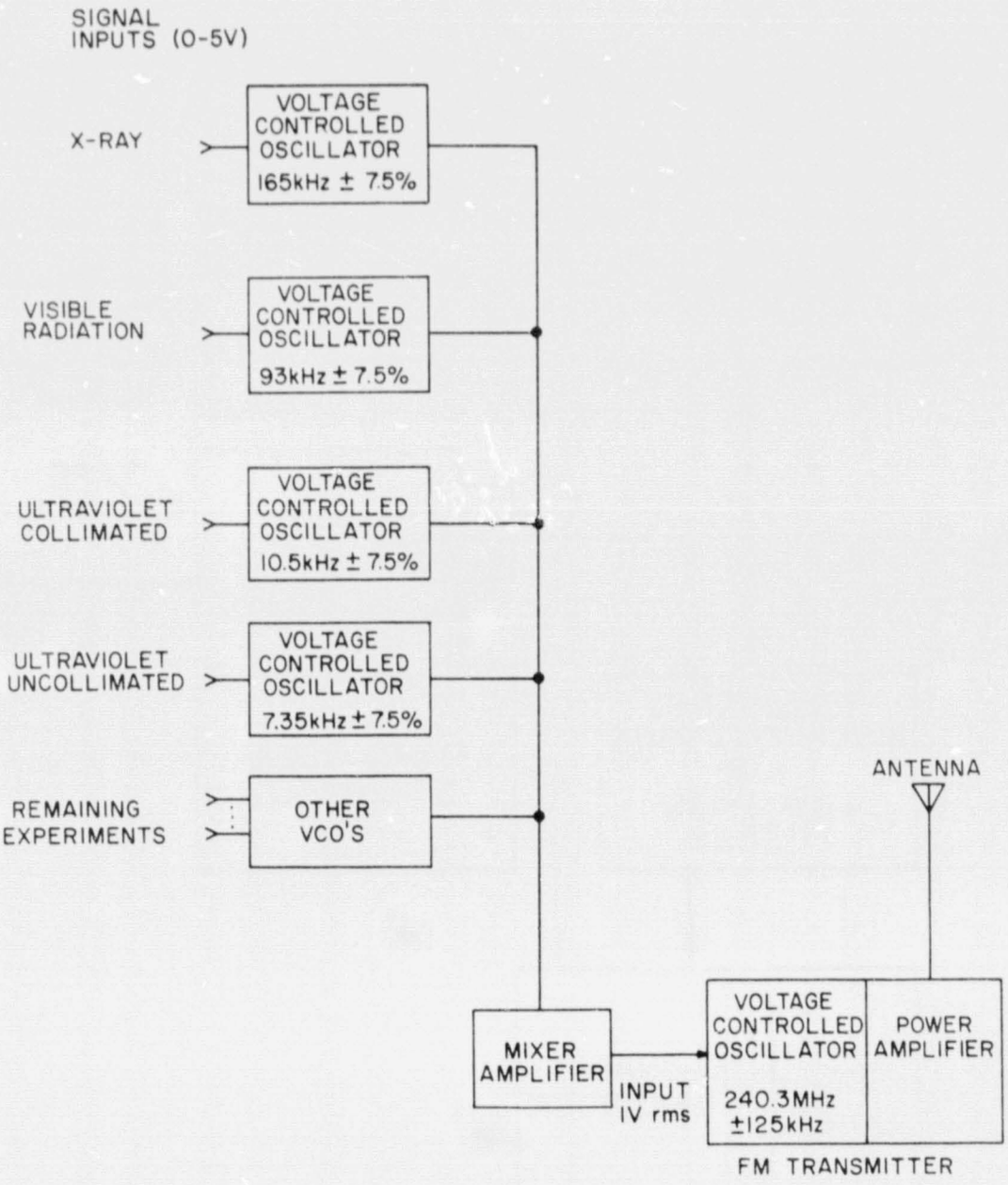

Figure 6.1 Rocket telemetry system for the UV experiment.

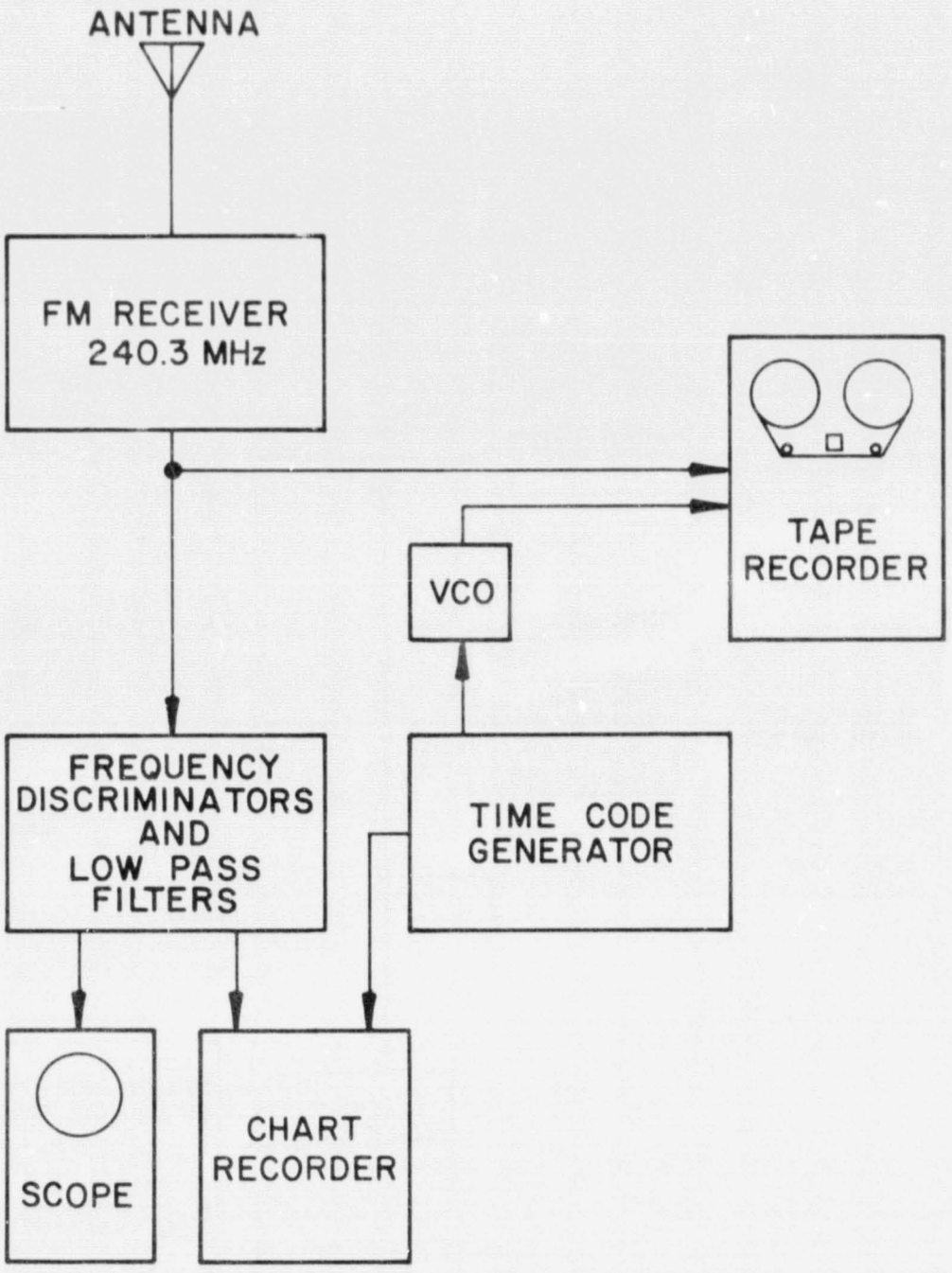

Figure 6.2 Ground telemetry system [*Evans and Smith*, 1975].

6.2 *Control and Power Systems*

The control and power system provides power for the payload instrumentation and controls certain occurances which must be excuted during a flight. Only the functions performed by the control and power system that pertain to the experiments covered in this report will be discussed.

The payload instrumentation is powered by a 30 V rechargeable battery that consists of twenty 2 Ampere-hour zinc-silver oxide cells packaged in a 3" × 4" × 7" aluminum container. Two power busses are derived from the battery; a 30 V line directly from the battery and a -30 V line supplied via a regulated dc/dc converter module.

Provisions are made to power the payload from an external power supply before a launch to preserve battery charge during the pre-flight checkout of the payload. This external supply maintains a full charge in the battery and also powers a heating element in the battery compartment. The heater is turned on only if the payload temperature is to low for optimum battery performance.

Two minutes before launch time, a relay is triggered to switch the payload to internal power. As a safeguard against this relay malfunctioning, a network of altitude sensitive switches (baroswitches) are arranged to switch the payload to internal power at an altitude of 12 km, regardless of the status of the relay. The baroswitch network also provides a 30 V calibration signal to the Lyman-α electronics while the rocket is in the range of 40 to 79 km. The purpose of this calibration signal is discussed later.

The instrumentation is protected during the actual launch of the rocket by two doors covering the sensor openings. Once the rocket has attained sufficient altitude (50 km) these doors must be released. At a predetermined elapsed time, a mechanical timer, which is started by the thrust of the rocket motor, ignites an explosive charge to jetison the doors from the payload. The door-ejection circuit is armed at 21 km by the baroswitch network. A block diagram of the pertinent features of the control and power system is shown in Figure 6.3.

6.3 *Mechanical Layout*

The aluminum framework of the University of Illinois payload consists of 12 inch diameter, 1/4 inch thick decks supported by 4 rigid side rails.

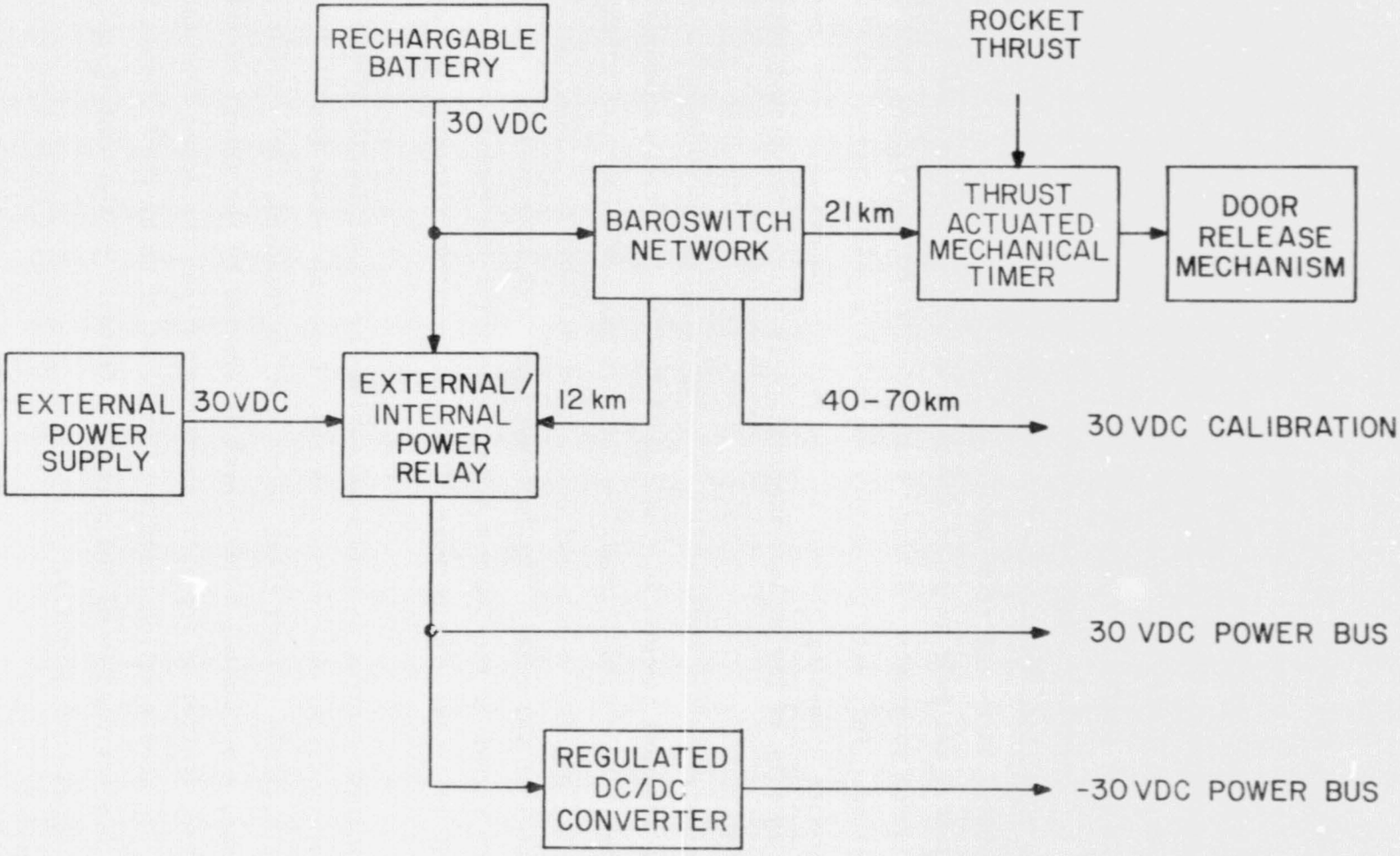

Figure 6.3 Block diagram of the portion of the control and power system pertinent to the X-ray, Lyman-α, and visible light experiments.

The entire assembly is enclosed in a 3/8 inch thick cylindrical shell with ejectable doors covering two opposing openings in the side of the payload. The doors are ejected during the flight to expose the data collecting instrumentation to the outside world. The location of the doors on the University of Illinois payload and the location of the University of Illinois payload with respect to other instrumentation is shown in Figure 6.4. Figure 6.5 gives a cutaway view of the University of Illinois payload showing the location of the experiments discussed in this report. Concluding this chapter is Figure 6.6 which is a photograph of the fully assembled University of Illinois payload section, taken prior to installation.

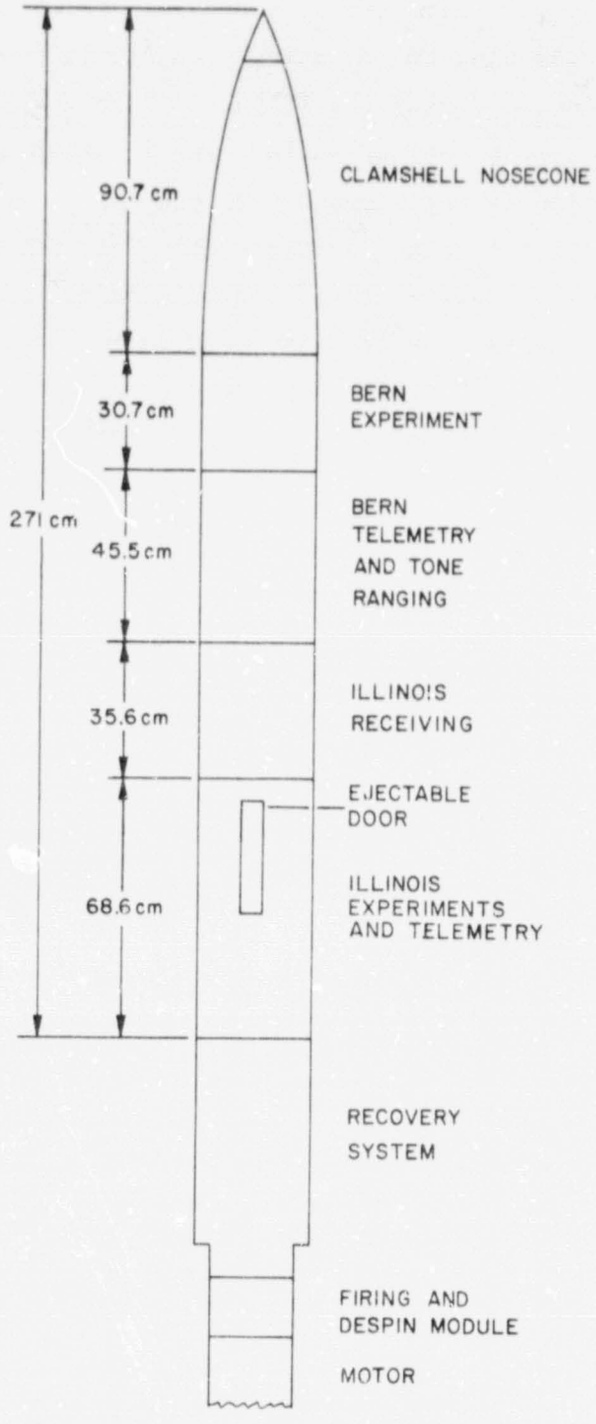

Figure 6.4 The general arrangement of the three payloads for the eclipse operation.

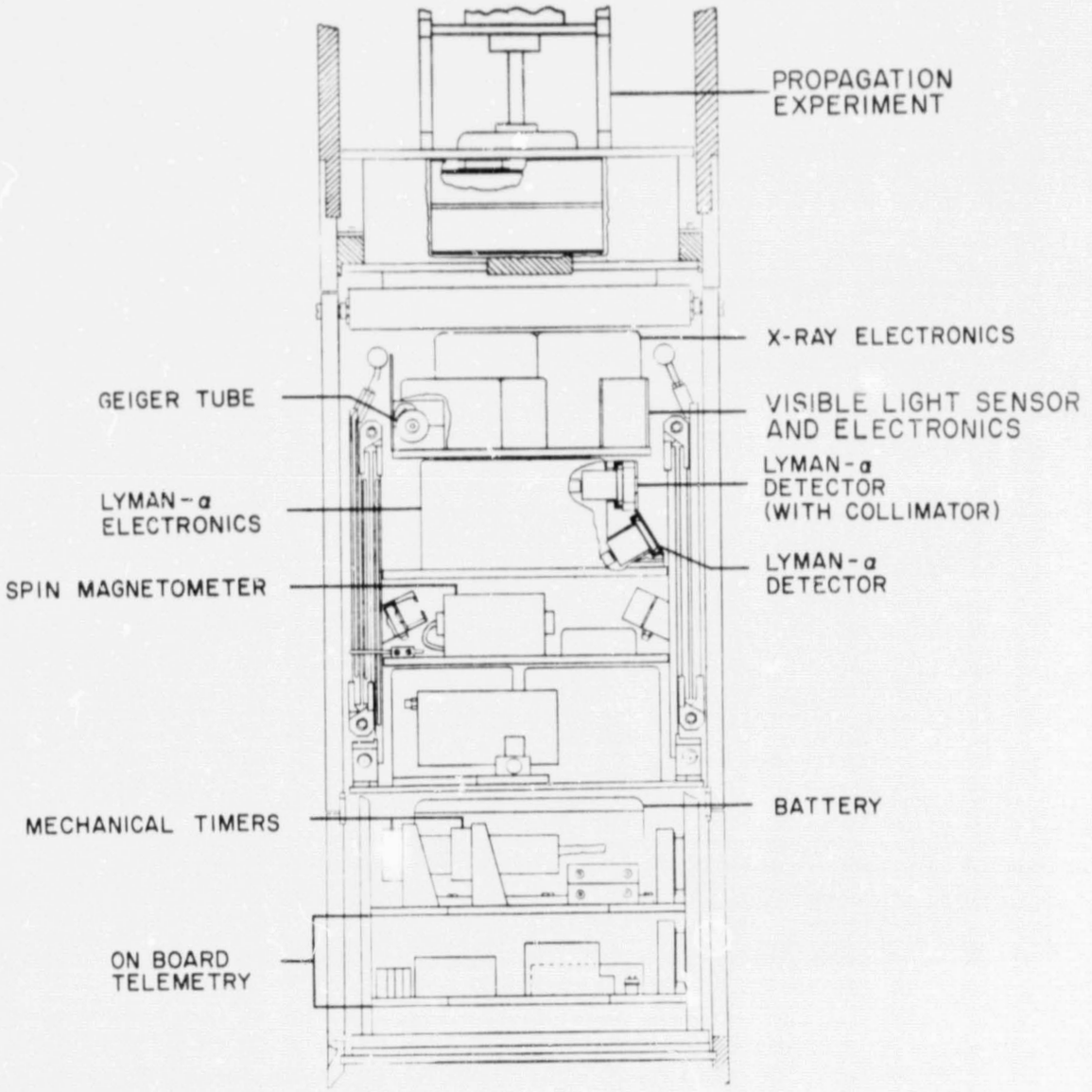

Figure 6.5 Arrangement of the University of Illinois experiments in the payload.

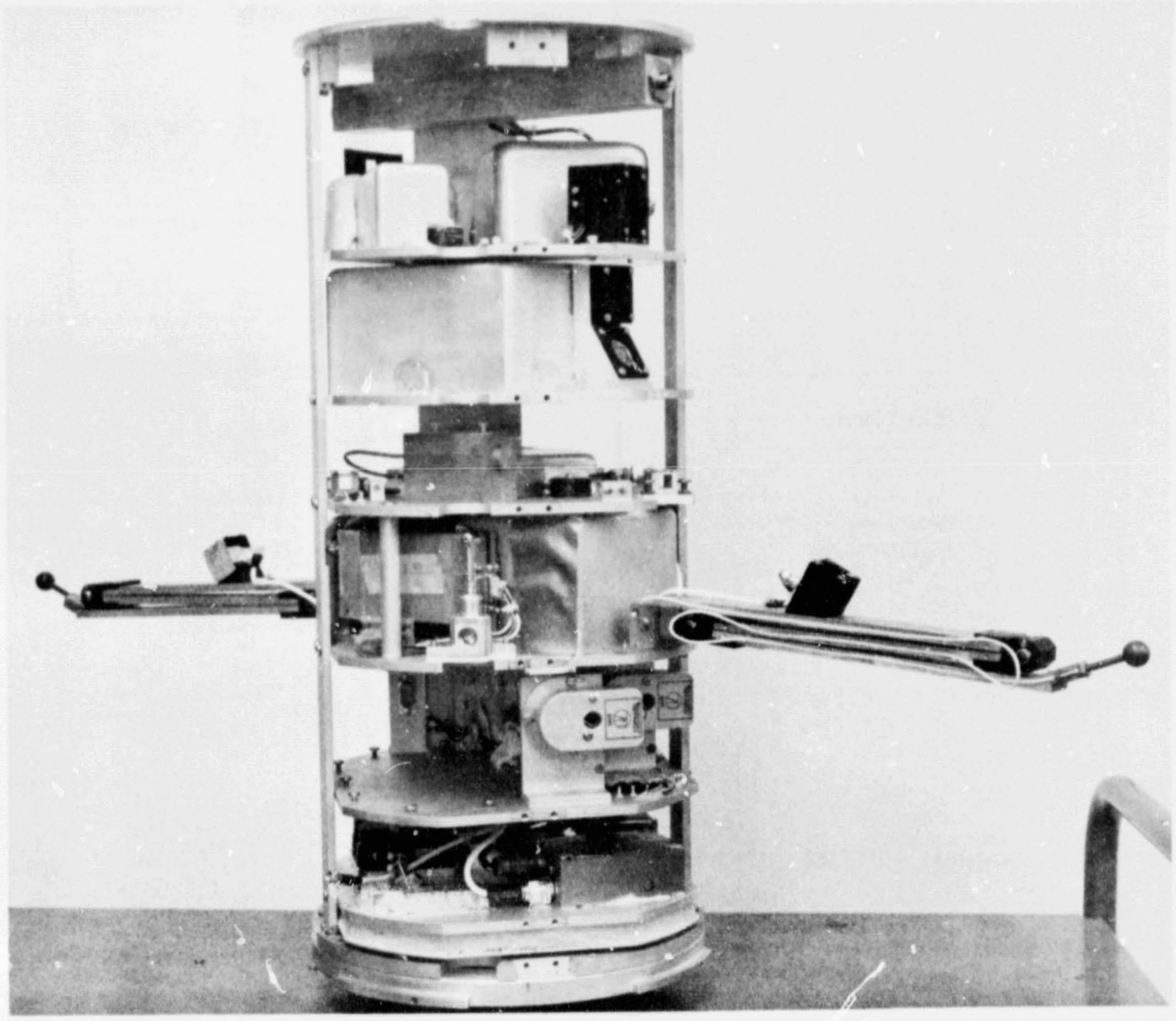

Figure 6.6 The lower section of one of the Nike Tomahawk payloads including the X-ray, Lyman-α and solar sensors, the partially extended booms carring the probes and the particle detectors, and supporting instrumentation.

7. DATA PROCESSING

7.1 *Introduction*

The signals representing the outputs of the various experiments are such that they require processing before they can be presented as useful data. A computer is used to perform most of the processing tasks. The recorded telemetry signal is first demultiplexed then digitized and re-recorded in a digital form. The recording of the digitized data is provided in an IBM format from the Wallops Island facility. To take advantage of the high speed of the CDC 175 computer at the University of Illinois, the IBM formatted data are copied to yet another tape in a format compatible with the CDC machine, thus providing both IBM and CDC formatted tapes.

This chapter describes, in detail, the processing of the raw data and discusses further processing to be performed in the future.

7.2 *Telemetry Calibration*

At the beginning of each IBM-formatted data tape are five records representing five output levels from the FM discriminators that were used to decode the data from the composite frequency division multiplexed telemetry signal. These levels represent band center, ±3.75%, and ±7.50% deviation from the center frequency of each channel. Ideally, they would correspond exactly to 0.0, 1.25, 2.50, 3.75, 5.00 V output from the payload instrumentation. In practice, this is not always the case and sometimes a correction must be applied to acquire the true levels. This correction is discussed later in this chapter.

The calibration levels for the present experiment, as read by the FORTRAN program CALIB [*Zimmerman and Smith*, 1980], are given in Table 7.1.

7.3 *Processing of Lyman-α Data*

The recorded signals from the collimated and uncollimated photometers are processed to derive Lyman-α absorption profiles and rocket aspect information. This processing is broken into the following categories,

(1) Establishing the reference levels

(2) Peak detection

(3) Detector aspect calibration

Table 7.1 Calibration levels from the digital data tapes as read by the program CALIB.

Instrumentation Channel		-7.50%	-3.25%	BAND CENTER	+3.75%	+7.50%
18.1020	Lyman-α (U)*	201.1	1116.1	2038.7	2957.3	3878.1
	Lyman-α (C)	109.7	1073.0	2036.3	3001.3	3964.8
	Solar Sensor	145.0	1985.3	2030.0	2976.5	3925.4
18.1021	Lyman-α (U)	203.4	1118.5	2041.4	2960.3	3880.9
	Lyman-α (C)	111.8	1074.8	2037.8	3002.4	3966.0
	Solar Sensor	149.8	1091.0	2037.9	2985.3	3935.1
18.1022	Lyman-α (U)	194.7	1113.6	2040.7	2963.2	3887.5
	Lyman-α (C)	112.2	1075.2	2039.7	3005.5	3970.8
	Solar Sensor	152.5	1095.1	2041.3	2989.4	3940.1

*U = Uncollimated detector

C = Collimated detector

7.3.1 *Reference levels.* Two reference voltages for each Lyman-α photometer are available on the digital tapes for verification of the calibration of the payload telemetry system. Unlike the demodulation operation which is performed in the laboratory with exact calibration levels, the modulation of the telemetry signal takes place within the payload and is therefore vulnerable to any variation in system performance that may be caused by extreme temperatures and/or mechanical shock. Thus there is a need to establish two reference voltage levels during the flight. These levels represent 0.0 and 5.0 V outputs from the Lyman-α electronics. The 0.0 V reference is taken from the Lyman-α data just prior to the ejection of the doors and the 5.0 V reference is generated by the Lyman-α electronics beginning 23 seconds after the launch and has a 6-second duration.

The recorded 5.0 V signal was noisy due to vibrations caused by the thrust of the Tomahawk stage and was not used. It is recommended that in future flights which use this type of instrumentation that the 5.0 V calibration signal be generated during a time interval of minimal mechanical vibration. Fortunately, the Lyman-α output before the door ejection was quite smooth and a usable zero reference signal was obtained. The zero references for flights 18.1020, 18.1021, and 18.1022 are given below.

Flight Number	Detector Type	
	Collimated	Uncollimated
18.1020	80.4	155.1
18.1021	235.1	362.8
18.1022	142.5	245.9

Once the zero references are determined, the telemetry system calibration levels of Table 7.1 can be normalized to the Lyman-α output. This is accomplished by shifting the five calibration levels the same amount so that the value corresponding to -7.50 percent deviation will be equal to the zero reference.

As an example, consider the channel corresponding to the uncollimated detector of flight 18.1020. The zero reference for this channel is 155.1 and from Table 7.1, the -7.50 percent deviation level is 201.1. Therefore,

to normalize the calibration levels of this channel each must be reduced by 46 units, resulting in the following data conversion levels.

155.1 - 0.0 Volts
1070.1 - 1.25 Volts
1992.7 - 2.50 Volts
2911.3 - 3.75 Volts
3832.1 - 5.00 Volts

With these data conversion levels, the data points of the digital tapes can be translated into voltages using linear interpolation between levels: an FM transmission scheme inherently provides a linear output. For example a recorded data point of 5000 would correspond to a voltage level of 3.87 volts. The data conversion levels for all three flights along the two additional quantities, the shift magnitude and the percent correction, are given in Table 7.2. The shift magnitude is the absolute value of the difference between the zero reference and the -7.5 percent deviation calibration level, and the percent correction is 100 times the ratio of the shift magnitude to the overall deviation of the calibration signal from -7.5 to +7.5 percent. With the aid of Table 7.2 the raw data can be converted to voltage levels with the percent correction indicating the degree of uncertainty of the data.

7.3.2 *Peak detection.* The spinning motion of the payload sweeps the view of the Lyman-α photometers past the sun producing a periodic output signal. This signal appears as a train of rounded pulses from the uncollimated photometers. Typical segments of Lyman-α waveforms are given in Figure 7.1. The maximum values of both types of pulses produced is of interest for determining rocket aspect and Lyman-α absorption profiles. These pulses will be referred to as "peaks" and their maximum values will be referred to as "peak value".

The detection of peaks and the determination of the peak values is performed by the FORTRAN program UVPEAKS, Appendix I. It takes input from the CDC formatted tapes and outputs peak values along with the corresponding elapsed times from launch. It also determines background Lyman-α values which are average signal levels between peaks. This background Lyman-α values which are average signal levels between peaks. This background signal represents the scattered Lyman-α detected by the photometers when

Table 7.2 Data conversion levels for the Lyman-α data tapes.

Instrumentation Channel		Voltage Output					Shift Magnitude	Percent Correction
		0.0	1.25	2.50	3.75	5.00		
18.1020	Uncollimated	155.1	1070.1	1992.7	2911.3	3832.1	46	1.3
	Collimated	80.4	1056.0	2000.7	2947.2	3896.1	29	0.8
18.1021	Uncollimated	362.8	1277.9	2200.8	3119.7	4040.3	159	4.3
	Collimated	235.1	1074.8	2161.1	3125.7	4089.3	123	3.2
18.1022	Uncollimated	245.9	1164.8	2091.9	3014.4	3928.7	51	1.4
	Collimated	142.5	1105.5	2070.0	3035.8	4001.1	30	0.8

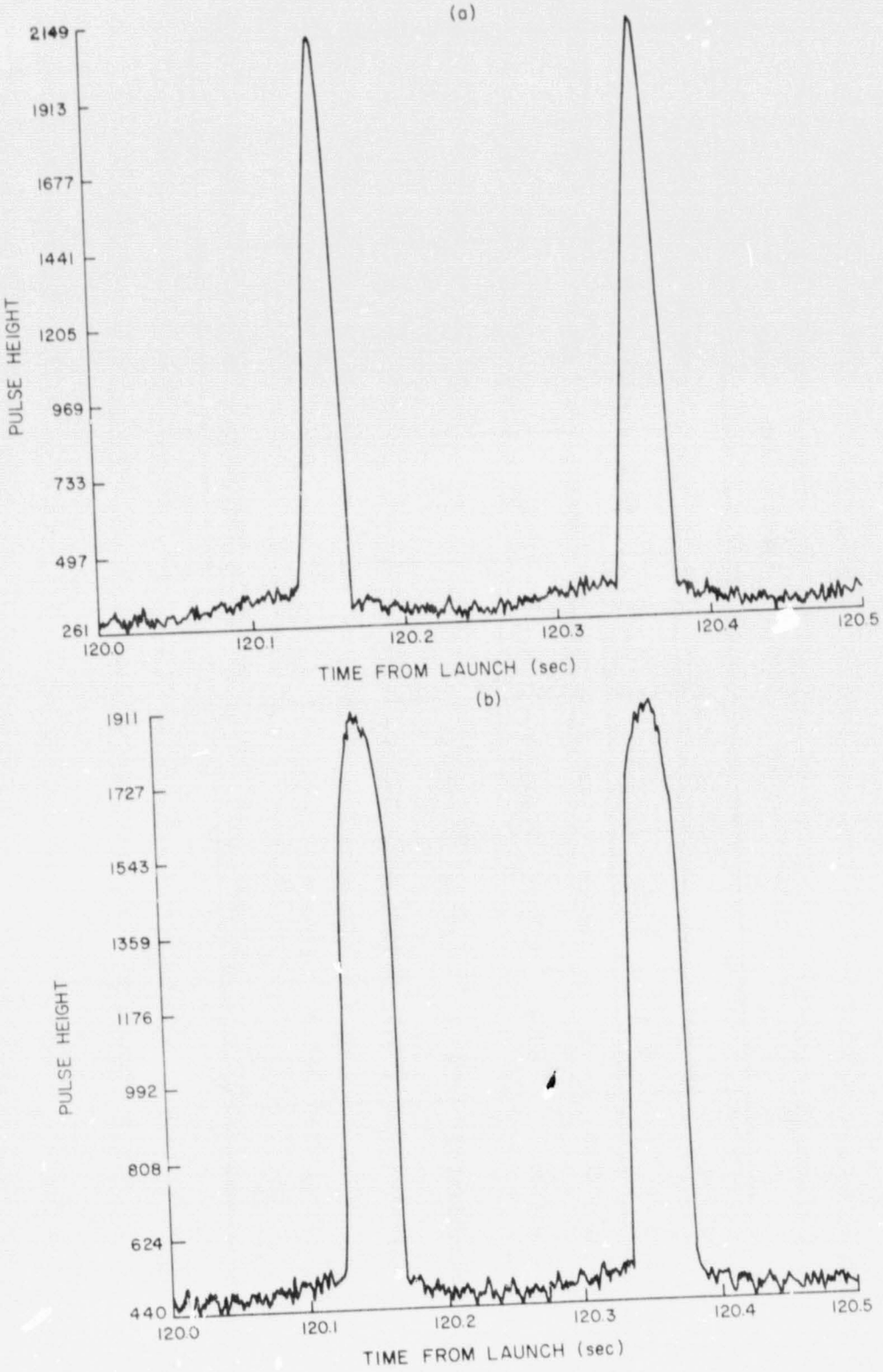

Figure 7.1 Representative portion of output signals from both Lyman-α detectors of flight 18.1022: (a) collimated, (b) uncollimated.

the sun is not within their direct viewing angle. A detailed description of how the program UVPEAKS works will now be presented.

The CDC formatted tapes are arranged in records containing one real number followed by an array of 5000 integers. The 5000 integers represent 5 channels of 1000 data points each, with every set of five consecutive integers containing one data point from each channel. The data points of channel n, where $1 \leq n \leq 5$, are given by every fifth element of the 5000 integer array starting with the n^{th} element, i.e., channel n is made up of all elements with indices in the set A, where $A = (n + 5j : j \in \{\mathbb{N} \cap [0,999]\})$. The real number at the beginning of each record represents the elapsed time from launch, which corresponds to the first set of 5 data points of the record. It should be noted that the elapsed time from launch is actually the elapsed time from ignition of the rocket rounded off to the nearest second. By doing this each record can be identified by a whole number of seconds and if an exact time is needed, the elapsed time from launch can be scaled accordingly. The exact launch times as taken from the chart records are 16:52:02, 16:52:01, and 16:54:01 UT for flights 18.1020, 18.1021, and 18.1022, respectively.

The program UVPEAKS processes the Lyman-α data one record at a time. A specified channel of each record is copied into the last 1000 locations of an 1100-element array called DATA. The first time a data record is read in, the first 100 elements of DATA are zero. For all subsequent readings of data records the first 100 elements of DATA contain the last 100 elements of the previous data record. This overlap allows detection of peaks which span two data records.

To detect a peak, the program scans all data points that are above a certain threshold that is specified by the user. The purpose of this threshold is to avoid detection of false peaks from within the background signal. An adaptive threshold option can also be specified by the user which allows the program to set the threshold equal to some fractional value of the magnitude of the previously detected peak. This fractional value remains constant throughout the run and must be entered by the user. It is sometimes necessary to test run the program to select the proper fraction. The adaptive threshold option is useful for when the background signal varies considerably during the flight. Before discussing how a peak is actually

detected two definitions are necessary. An "increase" is defined as a set of ten consecutive data points which have at least five positive differences between adjacent points that are less than the integer IJUMP. The default value for IJUMP is 100, but if necessary the user can enter a different value. The purpose of IJUMP is to provide noise immunity for the detection algorithm. Similarly a "decrease" is defined as 10 consecutive points with at least five negative differences between adjacent points which are less than the integer IJUMP.

The program UVPEAKS will scan the data looking for an "increase". Once an "increase" is found the program will look for a "decrease" starting with the data point that is the sixth element of the "increase". If the "decrease" is found the program will search for and count the local maximums within the data points bounded by the sixth element of the "increase" and the sixth element of the "decrease". If one local maximum and no local minimums are found the local maximum is considered a peak value. If more than one local maximum and/or more than zero local minimums are found, the program will apply a smoothing algorithm until either a peak value of the peak is identified or until the algorithm is applied ten times. The smoothing algorithm is given by the following difference equation.*

$$y(n) = [x(n - 1) + x(n) + x(n + 1)]/3$$

If a peak value is found, it is written to the output file along with the corresponding elapsed launch time to the nearest millisecond. Also, the number of filtering iterations used to obtain that peak value and the number of data points between the previous and present peak values are written to the output file. These numbers give an indication of the reliability of a specific data point. If no local maximum is found the program will proceed to search for the next "increase" starting with the tenth data point of the "decrease". The peak value identification algorithm is summarized in the flow diagram of Figure 7.2.

The program UVPEAKS has been used to determine the peak values of the Lyman-α data taken during flights 18.1020, 18.1021, and 18.1022. The program parameters used to generate these data are given in Table 7.3. The final

*Notice the non-causal nature of this smoothing algorithm. This is possible because the data for the entire flight is available from the digital tape in a random access manner.

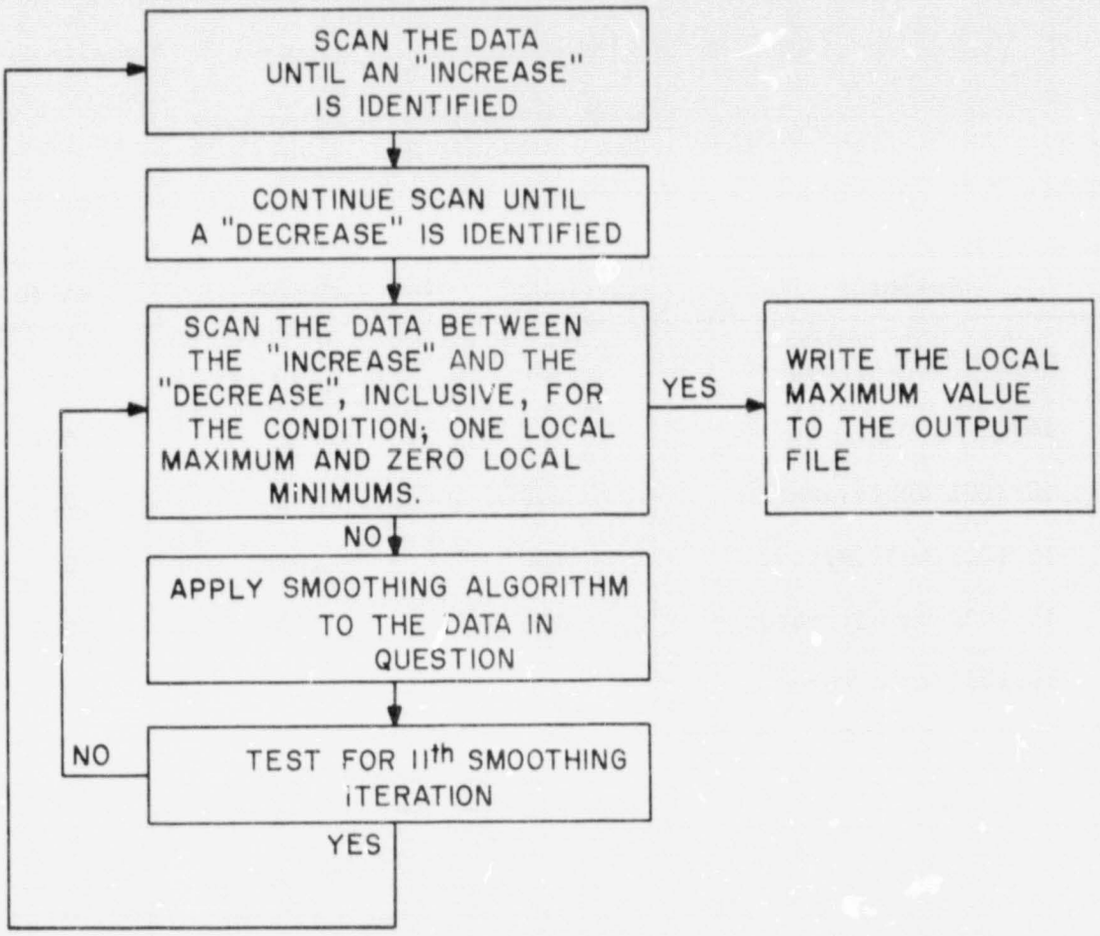

Figure 7.2 Flow diagram of the peak value identification algorithm used in the program UVPEAKS.

Table 7.3 Parameters used for executing UVPEAKS for each detector output.

Detector	IJUMP	ITHRSH	RATIO
18.1020 uncollimated	100	175	---
18.1020 collimated	200	90	0.1
18.1021 uncollimated	200	345	0.5
18.1021 collimated	100	235	0.5
18.1022 uncollimated	400	400	0.5
18.1022 collimated	400	250	0.5

plots are included in Chapter 8. It should be noted that these data are presented as a function of flight time, but could be given as a function of flight time, but could be given as a function of altitude using the flight trajectory record to convert flight time to altitude.

7.3.3 *Detector aspect calibration.* The Lyman-α photometers inherently exhibit a variation in output level with angle of incidence of incoming photons. A function fit to this angular variation is derived using experimental data obtained during flight 18.1021.

Before investigating the angular variation of the photometer, a preliminary expression which gives the included angle between a line normal to the surface of the photometer window and a line from the window to the sun in terms of the aximuthal and elevation angles of the two linear paths, will be derived. The included angle will be referred to as γ, he aximuth angles will be called ϕ_s and ϕ_p, and the elevation angles will be identified as θ_s and θ_p, where the subscripts s and p refer to the path to the sun and the normal to the photometer window, respectively. A pictoral representation of these angles is given in Figure 7.3. Consider the right triangle in Figure 7.3 with hypotenuse c. Applying the Pythagorean relationship to this triangle gives,

$$c^2 = c_o^2 + (b \sin \theta_s - a \sin \theta_p)^2 \tag{7.1}$$

The law of cosines applied to the triangle defined by the three sides labeled a_o, b_o, and c_o gives,

$$c_o^2 = a_o^2 + b_o^2 - 2a_o b_o \cos(\phi_s - \phi_p) \tag{7.2}$$

In terms of lines a and b the sides a_o and b_o are,

$$a_o = a \cos \theta_p \tag{7.3}$$

$$b_o = b \cos \theta_s \tag{7.4}$$

Substituting (7.3) and (7.4) into (7.2), and then substituting (7.2) into (7.1) gives the following expression for c^2,

$$c^2 = a^2 + b^2 - 2ab \sin \theta_s \sin \theta_p - 2ab \cos \theta_p \cos \theta_s \cos(\phi_s - \phi_p). \tag{7.5}$$

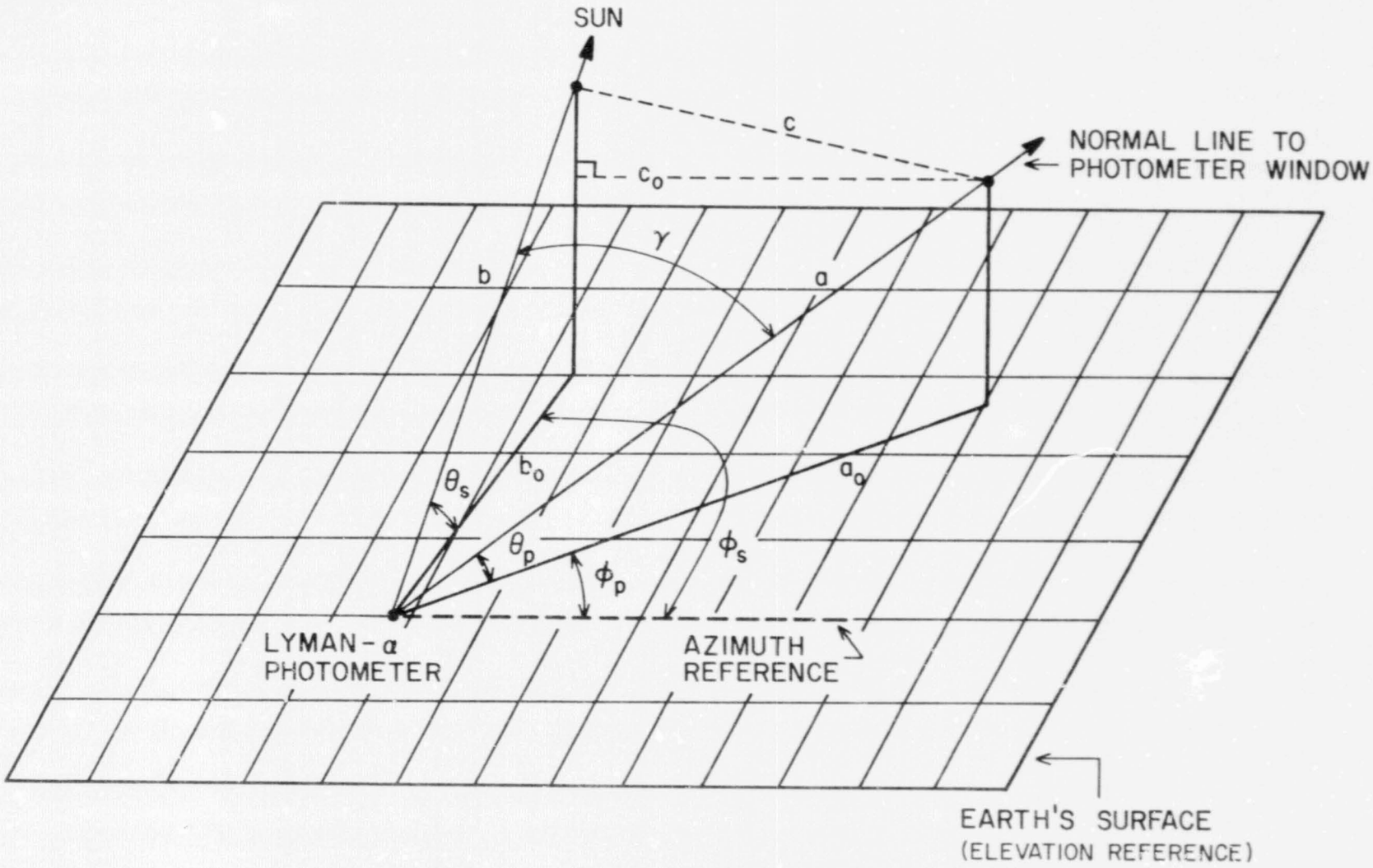

Figure 7.3 Pictorial representation of the angles pertinent to the Lyman-α detector aspect calibration.

Using (7.5) to represent c^2, the law of cosines applied to the triangle defined by the sides labeled a, b, and c gives the desired expression,

$$\cos \gamma = \sin \theta_s \sin \theta_p + \cos \theta_s \cos \theta_p \cos(\phi_s - \phi_p) \tag{7.6}$$

which defines the angle of interest, γ, in terms of the two linear paths a and b.

The "peak values", as determined by the program UVPEAKS, represent the detector output for whenever the azimuth angle of a line orthogonal to the detector window is equal to the azimuth angle of a linear path from the rocket to the sun, i.e., whenever $\phi_p = \phi_s$. Since the elevation angle of the sun is essentially constant throughout the flight (270), a plot of this data would vary as a function of the photometer elevation angle, θ_p, and the Lyman-α intensity. For determining the angular sensitivity of a detector, the variation due to Lyman-α intensity is eliminated by considering only the detector output for when the payload is in a region of the atmosphere where no absorption of Lyman-α takes place. This region of constant Lyman-α flux is generally considered to be altitudes above 100 km.

The collimated detector response is modeled by,

$$I(\gamma) = I_0 \cos^p(\gamma) \tag{7.7}$$

where p is some real number between 1.0 and 2.0 to be determined by function fitting $I(\gamma)$ to appropriate pulses of the detector output signal. A discussion of the selection of pulses suitable for modeling the detector angular sensitivity will follow.

Consider the aspect position defined by $\theta_s = \theta_p$ and $\phi_s = \phi_p$. For this orientation of the payload it can be seen from (7.6) that $\gamma = 0$ which indicates that the photometer window surface is orthogonal to a linear path from the detector to the sun. By observation of a plot of peak values, such as the plots in Chapter 8, it can be determined if the detector has passed through this orthogonal position and if it has the location where the payload passes through this position can be identified.

Due to the processional motion of the payload, the peak value plots of Chapter 8 exhibit a consistent periodic variation throughout the flight. If the detector passes through the orthogonal orientation during a flight, an additional pair of smaller variations will be present at one extreme of

The processional cycle caused by the detector passing through the point of its maximum output.* The maximum values of these smaller variations occur when the detector passes through the orthogonal position. Therefore, to locate the orthogonal positions of a given flight, one would look for the maximum values of the smaller variations.

If the orthogonal aspect position occurs while the payload is above the Lyman-α absorbing region or does not occur at all, an alternate aspect measuring device (e.g. a spin magnetometer) must be used to indicate when the payload is at the closest point to the orthogonal position, while it is still above the absorbing region and then a scaling factor must be used when determining I_0 and the angular sensitivity. Since the output of an uncollimated detector varies minimally for small angular deviations, a highly accurate alternate aspect sensor is not needed as long as the detector comes within a few degrees of the orthogonal aspect position.

As an example, consider a flight where the uncollimated detector does not pass through the orthogonal aspect position but does come within 2° at some point above the Lyman-α absorbing region, as indicated by a spin magnetometer. The angular sensitivity model (7.7) would be scaled down by a scaling factor, $\cos^p(2°)$, where $1 \leq p \leq 2$, before it is fitted to a pulse. For $p = 1$ the scaling factor is 0.999 and for $p = 2$ the scaling factor is also 0.999. If the spin magnetometer was inaccurate by 2° and the actual payload aspect was 4°, the scaling factor should have been somewhere between $\cos(4°) = 0.998$ and $\cos^2(4°) = 0.995$ which indicates a maximum scale factor error of only 0.4 percent. From this example, it can be seen that a high accuracy is not required of the spin magnetometer and that for small deviations from the orthogonal aspect position, the scaling factor is essentially equal to 1 and is therefore not needed.

Once the point in the trajectory is found where the detector either passes through or is within a few degrees of the orthogonal position, the angular sensitivity model (7.7) can be fitted to the pulses to determine the proper value of p. An explanation of how this was done for the data of flight 18.1021 will follow.

---

* A good example of this type of plot is the plot of peak values of the collimated detector output of flight 18.1020 in Chapter 8.

From the spin magnetometer output, it was found that the closest the uncollimated detector window came to being orthogonal to a line from the detector to the sun was 3° at an altitude of 132 km. and 194.5 s into the flight. Since $\cos(3°) \cong \cos^2(3°) = 1.0$ a scaling factor is not needed.

Five pulses from around 194.5 s into the flight were chosen for the curve fit. A plot of these pulses is given in Figure 7.4. Notice the considerable background level from when the sun is not directly within the viewing angle of the detector and the steep sides of the pulses caused by the edges of the opening in the shell of the payload.

Since the detector response is symmetrical and a smooth plot is desirable, each of the five pulses was divided into two parts at its axis of symmetry and then a point for point average of the resulting ten sets of data was determined. The background level was subtracted from the average variation and also the time scale was converted to an angular scale of 0° to 45°, where 0° corresponds to normal incidence. To convert from a time scale to an angular scale equation (7.6) was used with $\theta_s = 30°$, $\theta_p = 27°$, $\phi_p = 0°$ (reference), $\phi_s = f(t) = 360°(t/\tau)$, and $\tau = 210$ ms, where τ is the spin period of the payload. Rearranging (7.6) and inserting these values gives the following equation for angular deviation in terms of elapsed time (in milliseconds) from the center of a pulse.

$$\gamma = \text{arc cos } [0.227 + 0.772 \cos(t/0.583)] \tag{7.8}$$

A plot of the resulting average angular variation of the detector, denoted $f(\gamma)$, is given in Figure 7.5 (a).

Since the angular sensitivity is to be modeled by $\cos^n(\gamma)$, the following equation must be true

$$f(\gamma) = \cos^n(\gamma) \tag{7.9}$$

Taking the natural logarithm of both sides gives the following parametric equation in terms of the angle of incidence, γ,

$$\ln[f(\gamma)] = n \ln[\cos(\gamma)] \tag{7.10}$$

Since the opening in the payload shell cuts off direct Lyman-α penetration at 21° (see Figure 7.5), the slope of a least squares linear fit to the locus of points defined by,

$$\left\{ \Big(\ln[f(\gamma)],\ \ln[\cos(\gamma)]\Big) : \ 0 < \gamma < 21° \right\}, \tag{7.11}$$

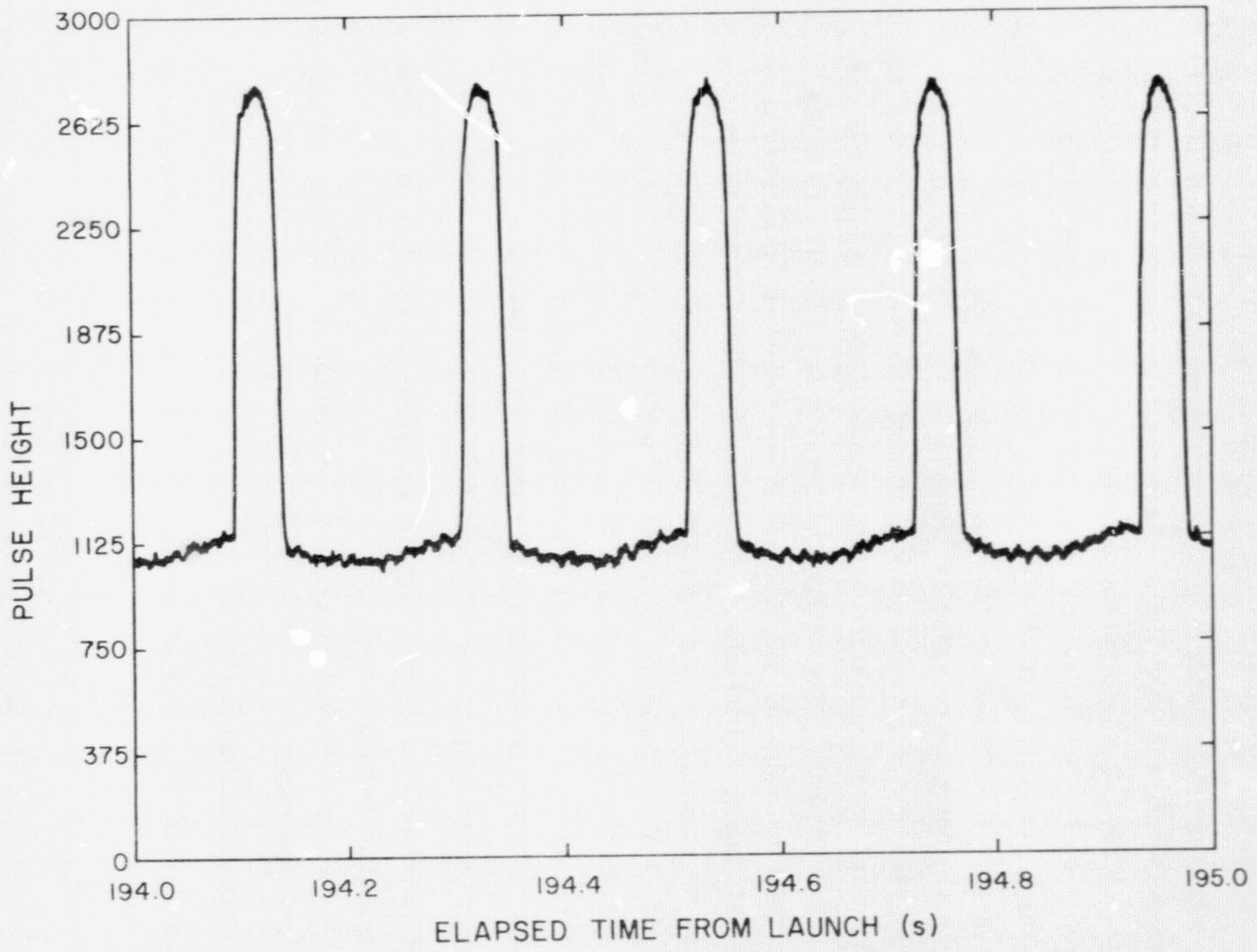

Figure 7.4 Five pulses from flight 18.1021 used for modelling the angular sensitivity of an uncollimated Lyman-α detector.

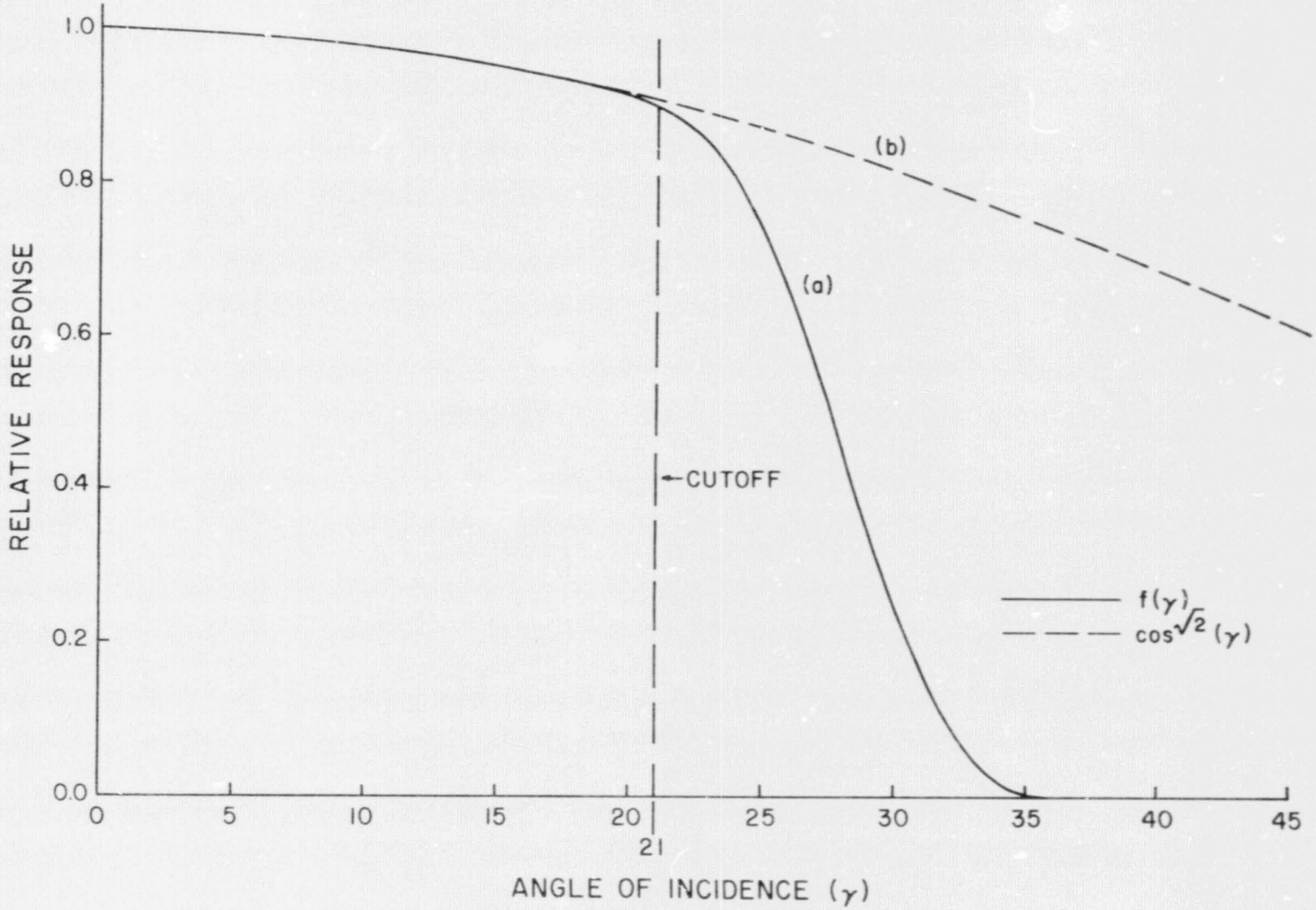

Figure 7.5 (a) Angular response of Lyman-α detector flown in payload 18.1021
(b) Angular response model, $\cos^{\sqrt{2}}(\gamma)$.

which gives a value of n = 1.1414 = $\sqrt{2}$. Figure 7.6 shows the data points in relation to the linear approximation and Figure 7.5 (b) gives the angular response model, $\cos^{\sqrt{2}}(\gamma)$, in relation to the actual angular sensitivity.

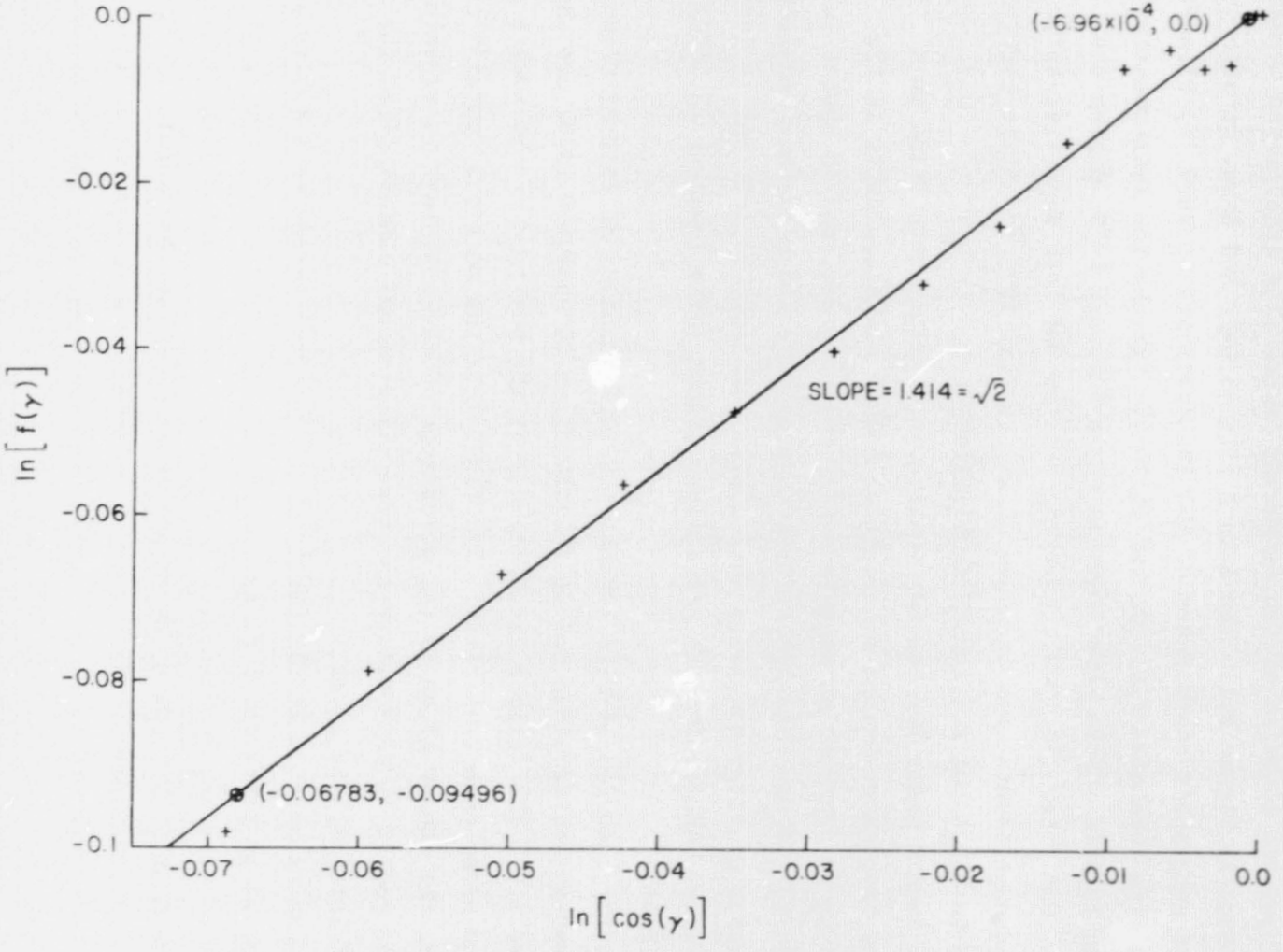

Figure 7.6 Linear approximation to ln[cos(γ)] versus ln[(γ)], for $0 \leq \gamma \leq 21°$, used for modelling the angular sensitivity of a Lyman-α detector.

8. FLIGHT PERFORMANCE

8.1 *Eclipse Circumstances*

The general location of the temporary launch site established by NASA is indicated in Figure 8.1. The launch site is near Red Lake, Ontario and the exact geographic coordinates of the launchers are 50.9029 °N, 93.4583 °W.

Two Nike Tomahawks (18.1021 and 18.1022) carrying the instrumentation described in this report were launched on 26 February 1979, during the eclipse. One other (18.1020), carrying similar but less sensitive solar radiation experiments, was launched on 24 February 1979 to obtain background data and to check out the launch facilities.

The launch times for the two rockets in totality were based on a predicted trajectory having an effective launch elevation angle in the range 83 to 86 degrees, an azimuth angle of 15 degrees, and an apogee in the range 134 to 138 km. The actual trajectories were close to those predicted with apogees of 132.6 and 132.3 km for Nike Tomahawks 18.1021 and 18.1022, respectively. Apogee for the pre-eclipse launch (Nike Tomahawk 18.1020) was 130.5 km.

The trajectories of Nike Tomahawk 18.1021 launched at 1652:00 UT and Nike Tomahawk 18.1022 launched at 1654:10 UT on 25 February 1979, are shown in Figure 8.2. The eclipse circumstances at the position of the rocket are indicated along each trajectory. For times when the rocket is outside of totality, the number given is the percentage of the disc that is visible. Where the rocket is in totality the time since second contact (i.e. the start of totality) is given.

It can be noted that the first of the two rockets enters totality at T + 60 s, at an altitude of 61 km, on ascent and exits at T + 300 s, at an altitude of 68.5 km, on descent. The second rocket remained in totality from launch until T + 106 s, at an altitude of 105 km, on ascent.

The circumstances confirm that, as planned, one rocket was in the *D* region just after the start of totality and the other just before the end of totality.

Another perspective on the eclipse circumstances is presented in Figure 8.3. Here the apparent sun-moon distance, in solar radii, is plotted against time. The magnitude of the eclipse is 1.0403 (i.e. the ratio of the mean diameters of moon and sun) so that a sun-moon distance of 0.0403 solar radii

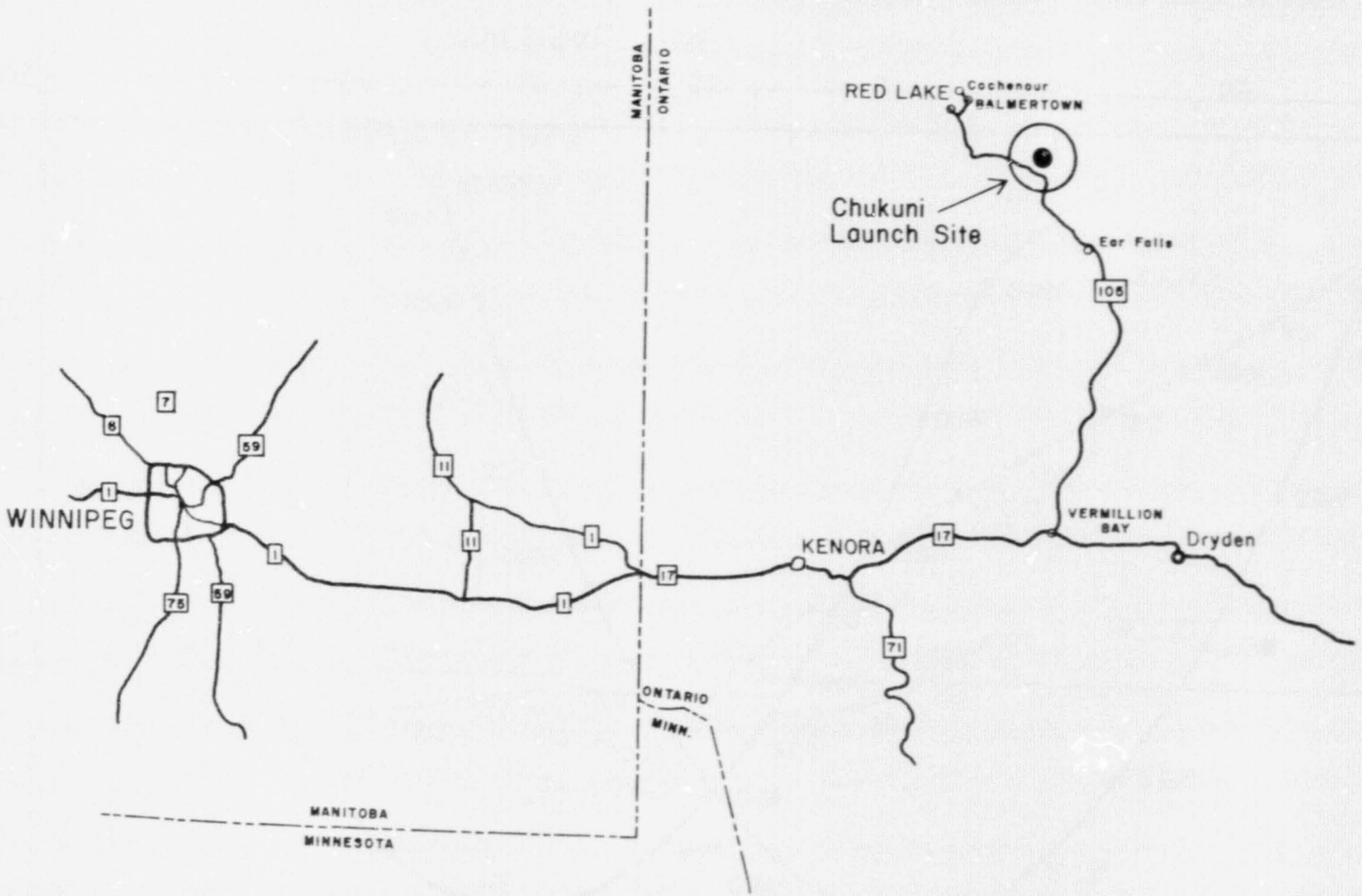

Figure 8.1 The location of the launch site for the eclipse of 26 February 1979.

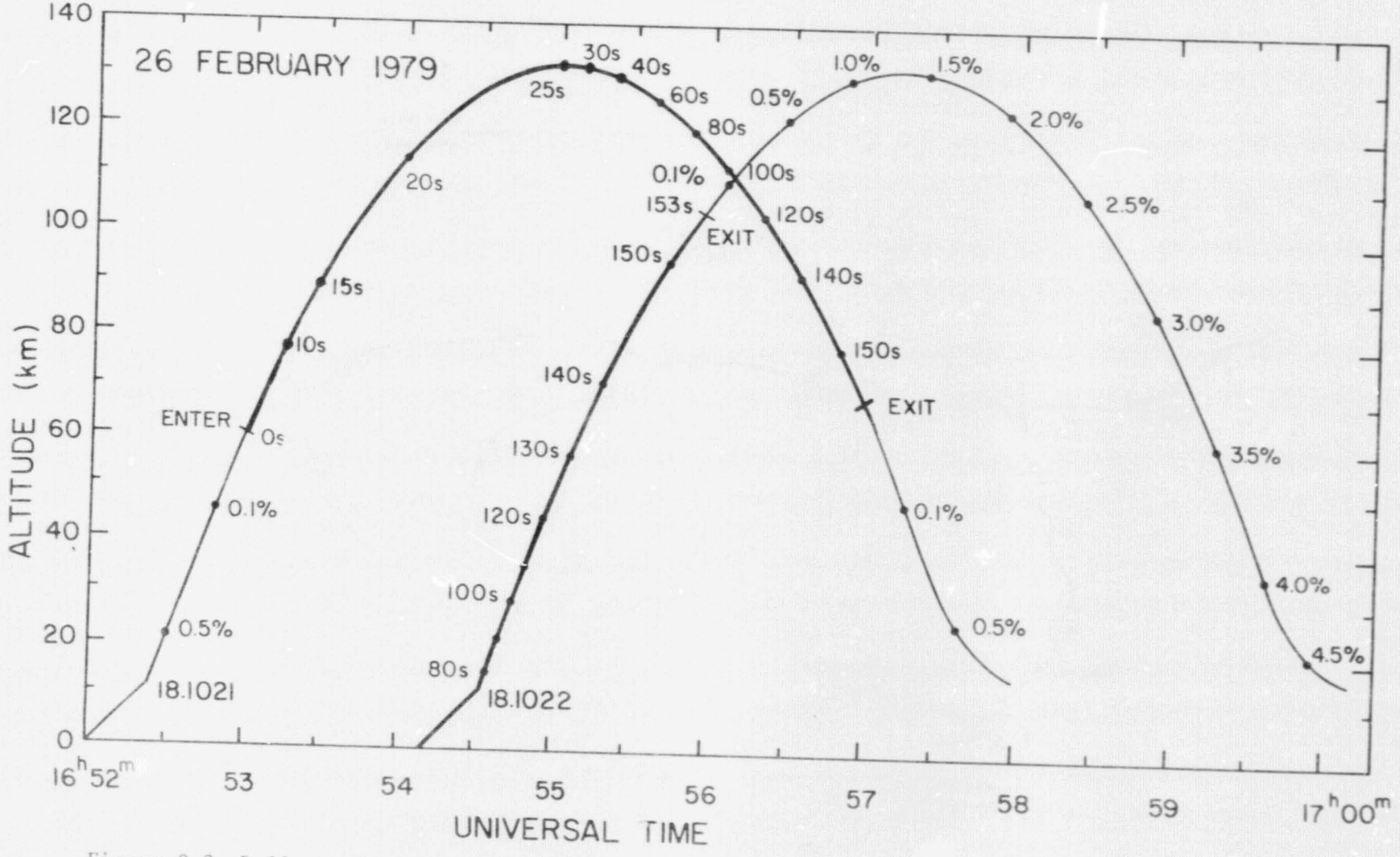

Figure 8.2 Eclipse circumstances at the position of the rocket. Marked along each rocket trajectory is the percentage of the solar disc that is visible and, inside totality, the time (seconds) since second contact.

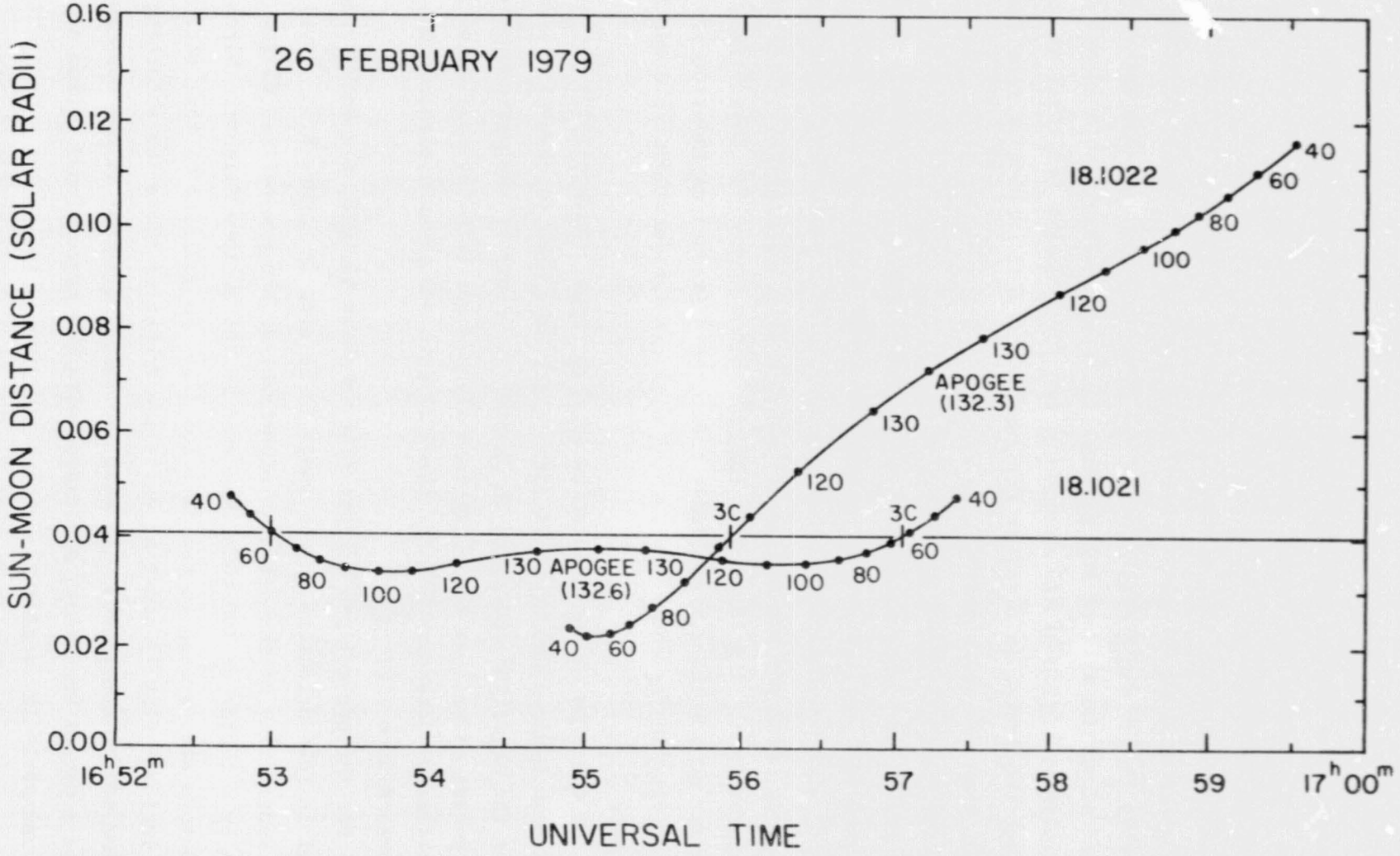

Figure 8.3 The eclipse circumstances at the position of the rocket represented by the radial distance from the shadow axis. The rocket altitude (km) is marked along each curve.

represents the edge of totality and 0 is center of totality. This figure gives a picture of the rocket position in terms of radial distance from the center of totality.

A complementary view of the trajectories is shown in Figure 8.4. This is a polar plot of the sun-moon distance against the angular position relative to the sun's North point, and gives a picture of the rocket position viewed along the axis of the shadow. It is a remarkable coincidence that the relative motion of the shadow and the first rocket (18.1021) is such as to keep the rocket in totality for such an extended period of time (rather longer than was anticipated).

8.2 *Solar Radiation Experiments*

Preliminary observations of the output signals from the detectors indicate that good direct and background Lyman-α data, as well as rocket aspect, will be obtainable using appropriate data processing techniques. The signal from the pre-eclipse flight exhibits a progressive decay starting at approximately T + 100 s from launch. Since apogee for this flight occurres at T + 182 s, this decay indicates a gradual degradation of sensitivity during the flight, which will require additional processing to correct.

At the time of the completion of this report (August 1979) the signals from both Lyman-α detectors of each flight have been successfully processed using the algorithm described in Chapter 7. Plots of the maximum values of the pulses as well as the background signals for both the collimated and uncollimated detectors for the three flights are given separately in Figures 8.5 to 8.7.

For the pre-eclipse flight, Nike Tomahawk 18.1020, the background level in both detectors is too small to be seen in Figure 8.5. Recall that the sensitivity of the detector experiment of the pre-eclipse flight was less by a factor of 100 than that used in the eclipse flights. Since the detectors are exposed to the full sun (i.e. no eclipse) on that occasion the incident flux is constant while the rocket is above the absorbing region of the atmosphere. In fact the recorded signal is not constant. It shows a period variation, associated with the precessional motion of rocket, and unexpectedly, a gradual decrease in signal, indicating a degradation of the detectors themselves. Since this is an effect of the high

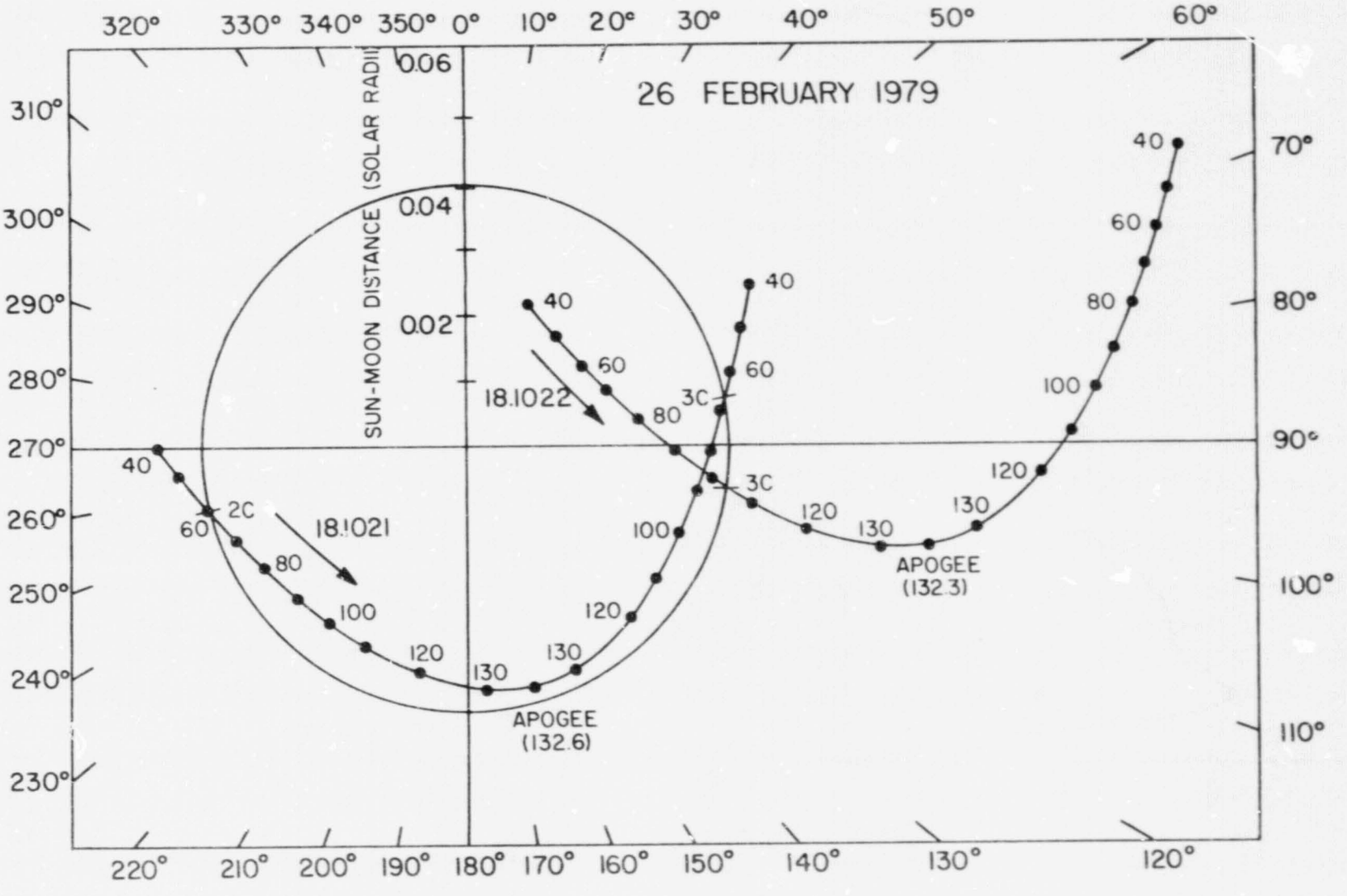

Figure 8.4 The eclipse circumstances here show the position of rocket viewed along the axis of the shadow. The rocket altitude (km) is marked along each curve.

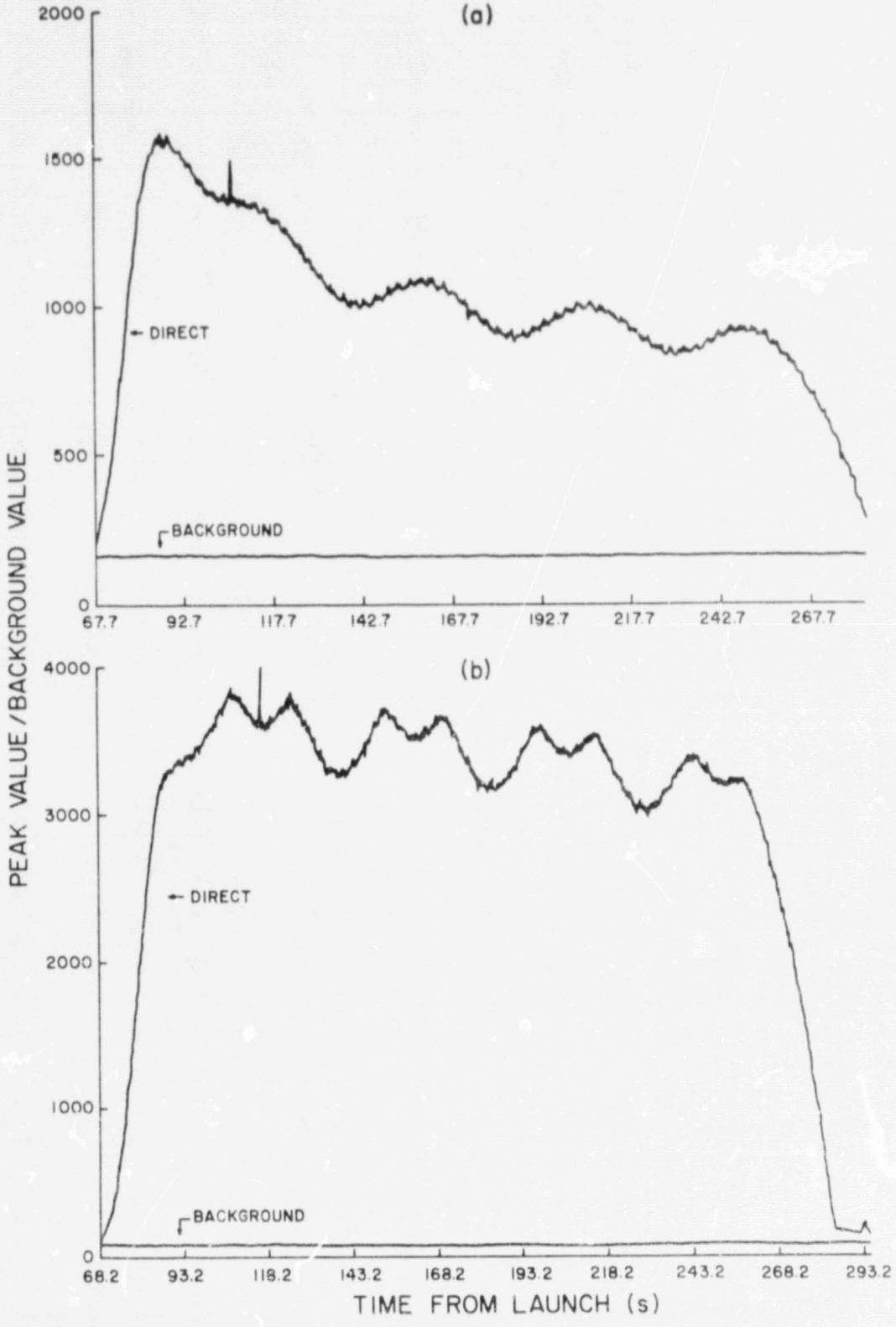

Figure 8.5 Maximum values of pulses and background values for both Lyman-α signals obtained during flight 18.1020 (a) uncollimated; (b) collimated.

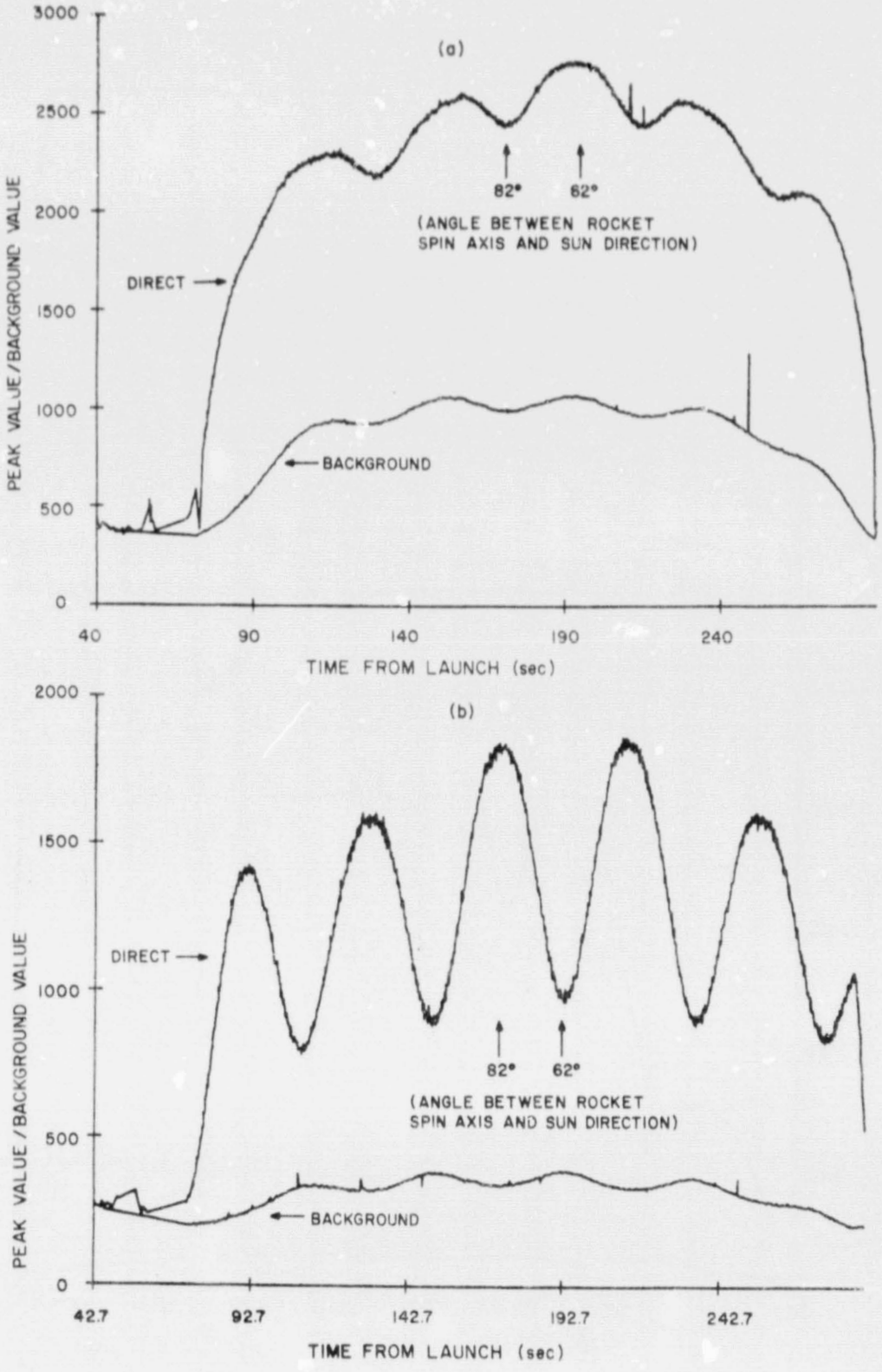

Figure 8.6 Maximum values of pulses and background values for both Lyman-α signals obtained during flight 18.1021 (a) uncollimated; (b) collimated.

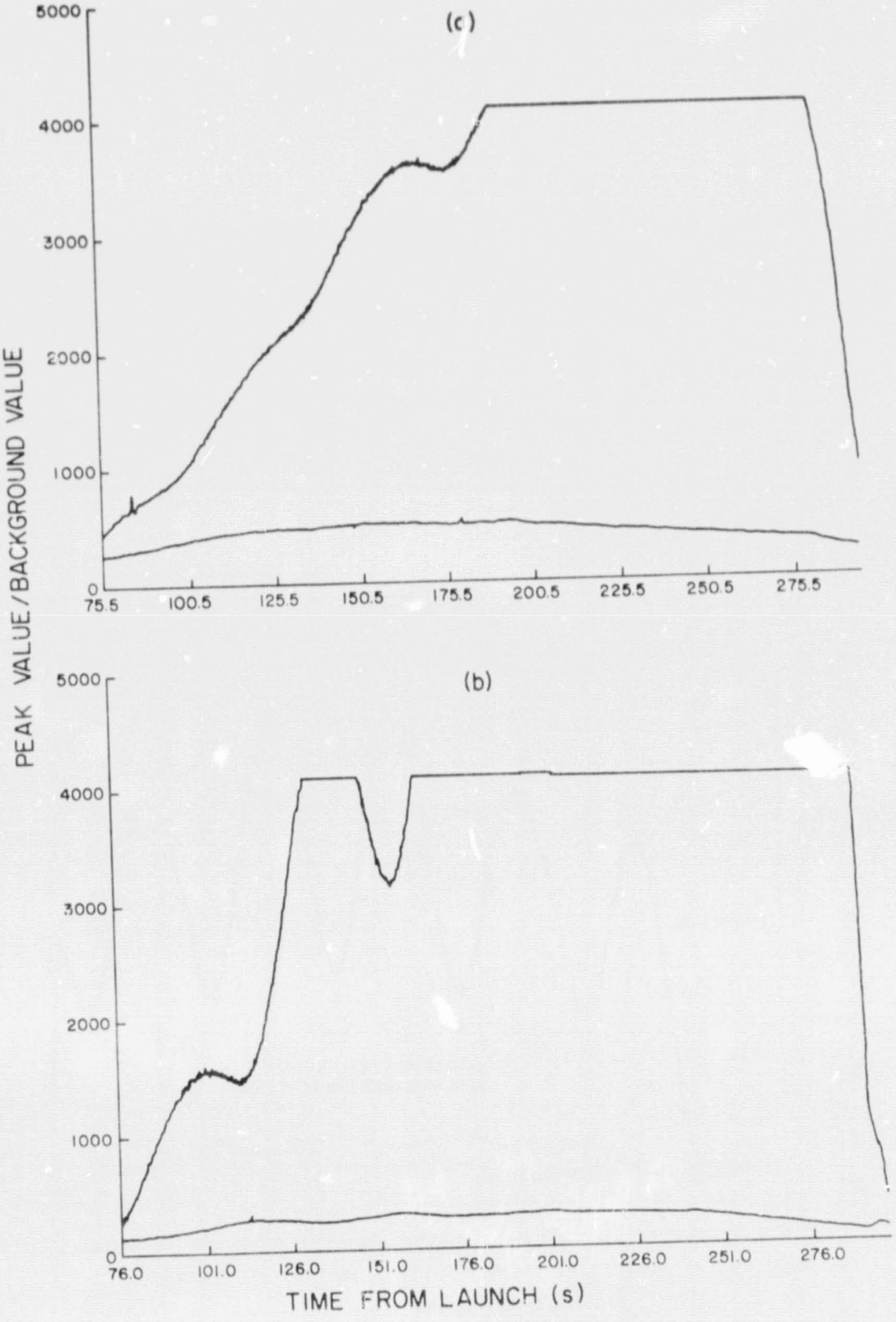

Figure 8.7 Maximum values of pulses and background values for both Lyman-α signals obtained during flight 18.1022 (a) uncollimated; (b) collimated.

(unattenuated) flux the actual Lyman-α flux can be determined by extrapolating back to the time that the rocket exits the absorbing region, at an altitude of about 110 km.

The rapid increase in signal in the initial part of the data represents the decreasing absorption of the Lyman-α flux and can be converted to a concentration profile of molecular oxygen.

Neither detector on Nike Tomahawk 18.1021 show evidence of degradation, presumably attributable to the relatively small Lyman-α flux in totality (roughly 0.5% of the flux from the uneclipsed sun). The symmetry of the data, in time, is consistant with the symmetrical nature of the trajectory of the rocket with respect to the umbra (see Figure 8.4). The precessional motion of the rocket is evident in the oscillating nature of the signal. As expected the uncollimated detector shows less sensitivity to payload orientation than does the collimated detector. The included angle of the precession cone for this flight, determined from the aspect magnetometer, is 20 degrees.

Nike Tomahawk 18.1022 was launched during totality and exited the umbra. As seen in Figure 8.7 the signal increases, with a superimposed oscillation again due to the precessional motion, until it reaches full scale (which represents about 1 percent of the flux from the uneclipsed sun). These data, together with those of 18.1021 allow the brightness of the solar chromosphere in Lyman-α to be determined. Also of interest in Figure 8.7 is the variation of the intensity of the scattered Lyman-α signal. This has not yet been explained, even qualitatively.

9. CONCLUSION AND RECOMMENDATIONS FOR FUTURE WORK

This report has described the instrumentation and preliminary results of a group of solar radiation experiments flown in sounding rockets before and during the eclipse of 26 February 1979. The over-all design of the structure of a scientific payload and the post-flight data processing tasks have also been discussed.

Originally it was planned that results from both the X-ray and Lyman-α experiments would be included in this report. Due to an unusually high flux of energetic particles on the day of the eclipse, the hard X-ray data from the two eclipse launches was contaminated and is therefore not presented. However, it is fortunate that satellite observations on that day show that no significant level of hard X-rays was produced by the sun at the time of the eclipse.

The Lyman-α data has been processed to some extent and is presented in this report. Maintaining the goals of this paper, a detailed description of the Lyman-α data processing tasks, already performed, has been given along with motivation for the final processing of the data. A summary of the overall Lyman-α data processing requirements will follow.

The purpose of the Lyman-α data processing is to derive rocket aspect, direct Lyman-α intensity, and scattered background Lyman-α intensity from the recorded output currents of the two Lyman-α photometers. The data processing is divided into the following seven tasks.

(1) Modelling of the angular response of the uncollimated detector.

(2) Modelling of the angular response of the collimated detector.

(3) Determining the maximum values of the output pulses from the two photometers to be used in the derivation of both the direct Lyman-α intensity and the rocket aspect profiles.

(4) Determining the background level between the pulses of both signals to be used in the derivation of both the direct Lyman-α intensity and the rocket aspect profiles.

(5) Deriving the rocket aspect profile from the maximum values obtained in (3).

(6) Deriving the direct Lyman-α intensity profile by using the rocket aspect profile to normalize the data of (3).

(7) Derive the background Lyman-α intensity profile by applying a diffusion model to the data of (4).

A functional fit has been made to the angular response of the uncollimated detector in Nike Tomahawk 18.1021. It was found that the function

$$I = I_0 \cos^{\sqrt{2}} (\chi) \tag{9.1}$$

is a very good approximation to the detector output, where I_0 is the output current of the detector at normal incidence, and I is the output current for incoming radiation at an angle of incidence χ. Details of the curve fitting to the uncollimated detector output have been given in this report.

The collimated detector is closely approximated by a linear function and requires a linear curve-fitting technique. Since the uncollimated detector does not approach a position of normally incident radiation, two degrees of freedom must be considered when fitting the function to an output pulse.

A FORTRAN program titled UVPEAKS has been used to identify the maximum values of the output pulses and the background levels between the output pulses for both detectors of all three flights. The theoretical base and use of the program has been covered in this report. Outputs of the program have been plotted and are also presented.

The peak values of the signals from the Lyman-α detectors are also used to determine the rocket aspect. Since the Lyman-α intensity varies with altitude, the output currents from the detector must vary as a function of altitude as well as aspect angle. The outputs in terms of aspect angle, χ and altitude, h, are

$$I_1(h,\chi) = I_0(h) \cos^{\sqrt{2}} (\chi) \tag{9.2}$$

$$I_2(h,\chi) = I_0(h) \ (m\chi + b) \tag{9.3}$$

where I_1 and I_2 are the maximum values of the uncollimated and collimated detector outputs, repsectively, and m and b are to be determined by curve

fitting to the collimated output pulses. Taking the ratio of (9.2) and (9.3) gives the following equation.

$$\frac{I_1}{I_2}(h,\chi) = \frac{\cos^{\sqrt{2}}(\chi)}{m\chi + b} \tag{9.4}$$

Since m and b are known constants and the ratio $I_1/I_2\ (h,\chi)$ is easily calculated, the aspect angle χ can be determined, as a function of altitude, by solving (9.4) numerically for the aspect profile, $\chi(h)$, using a digital computer.

With the aspect profile available, the direct Lyman-α intensity profile is easily determined by solving (9.2) for $I_0\ (h,\chi)$ and inserting the corresponding values of $\chi(h)$. The background Lyman-α intensity profile is determined in a similar manner.

As mentioned in the text, the orientation of the Lyman-α detector is quite critical in an aspect determination application. In future applications of this technique, it is advised that care be taken in positioning the detectors to minimize the data processing and for independence from other aspect measuring devices. For example, it was necessary to use the spin magnetometer data to indicate when the detector approached a position of normally incident solar radiation. If the Lyman-α detector had passed through this position it would have been identifiable from the Lyman-α data independent of the spin magnetometer output. If this was the case, the spin magnetometer would have served only as verification of that position as opposed to being the sole indicator.

In general, the Lyman-α experiments were quite successful in that preliminary data indicate that accurate Lyman-α profiles, as well as rocket aspect, have been successfully obtained.

As a final note, it is hoped that the results of the experiments discussed in this paper will aid in the understanding of the complex interaction between solar radiation and the various components of the atmosphere.

REFERENCES

Accardo, C. A., L. G. Smith, and G. A. Pintal [1972], Rocket observations of solar x-rays during the eclipse of 7 March 1970, *J. Atmos. Terr. Phys.*, *34*, 613-620.

Evans, J. C. and L. G. Smith [1975], Rocket measurements of ozone and molecular oxygen by absorption spectroscopy, *Aeron. Rep. No. 66*, Aeron. Lab., Dep. Elec. Eng., Univ. Ill., Urbana-Champaign.

Korff, S. A. [1947], *Electron and Nuclear Counters-Theory and Use*, D. Van Nostrand Company, Inc.

Mechtly, E. A., K. Seino, and L. G. Smith [1969], Lower ionosphere electron densities measured during the solar eclipse of November 12, 1966, *Radio Sci.*, *4*, 371-375.

Mechtly, E. A., C. F. Sechrist, and L. G. Smith [1972], Electron-loss coefficients for the *D*-region of the ionosphere from rocket measurements during the eclipses of March 1970 and November 1966, *J. Atmos. Terr. Phys. 34*, 641-646.

O'Kelley, G. D. [1962], *Detection and Measurement of Nuclear Radiation*, Subcommittee on Radio-Chemestry, National Academy of Sciences, National Research Council.

Price, William J. [1964], *Nuclear Radiation Detection*, 2nd Edition, McGraw-Hill Book Company, New York.

Smith, L. G. [1972], Rocket observations of solar UV radiation during the eclipse of 7 March 1970, *J. Atmos. Terr. Phys.*, *34*, 601-611.

Smith, L. G., C. A. Accardo, L. H. Weeks, and P. J. McKinnon [1965], Measurements in the ionosphere during solar eclipse of 20 July 1963., *J. Atmos. Terr. Phys.*, *27*, 803-829.

Weeks, L. H. and L. G. Smith [1971], Lyman-α measurements during the solar eclipse of 12 November 1966., *Solar Phys.*, *20*, 59-63.

Whitten, R. C. and I. G. Poppoff [1971], *Fundamentals of Aeronomy*, John Wiley and Sons, Inc., New York.

Zimmerman, R. K., Jr., and L. G. Smith [1980], Rocket measurements of electron temperature in the *E* region, *Aeron. Rep. No. 92*, Aeron. Lab., Dep. Elec. Eng., Univ. Ill., Urbana-Champaign.

APPENDIX I

Listings of the programs UVPEAKS and FOUR

A.I.1 UVPEAKS

```
      PROGRAM UVPEAKS (INPUT,OUTPUT,UVDATA,UVOUT,BOUT,TAPE1=UVDATA,
     1TAPE2=UVOUT,TAPE3=BOUT,TAPE4=INPUT,TAPE5=OUTPUT)
C
C....  THIS PROGRAM IS USED TO IDENTIFY AND TABULATE PEAK VALUES
C....  FROM UV DATA OBTAINED DURING FLIGHTS 18.1020,18.1021,AND 18.1022.
C....  DATA(1100) = DATA RECORD WHICH IS BEING PROCESSED
C....  IJUMP = MAXIMUM ALLOWABLE INCREASE/DECREASE BETWEEN CONSECUTIVE
C....  POINTS; USED FOR NOISE DISCRIMINATION
C....  ICON = NO. OF CONSECUTIVE POINTS TO BE PROCESSED DURING EACH CALL
C....  TO SUBROUTINES INC OR DEC
C....  NA = NO. OF DATA POINTS TO BE AVERAGED AT A TIME BY
C....  SUBROUTINE SMOOTH
C....  ITHRSH = INITIAL THRESHOLD FOR ADAPTIVE THRESHOLD OPTION
C....  THRESH = THRESHOLD CONSTANT
C....  RATIO = (PRESENT THRESHOLD)/(PREVIOUS PEAK VALUE)
C....  TRKNUM = THE TAPE TRACK TO BE PROCESSED
C....  T = TIME OF FIRST DATA POINT IN A RECORD
C....  T1P = TIME OF PREVIOUSLY IDENTIFIED PEAK
C....  J1 = PREVIOUS PEAK LOCATION
C....  INC1/DEC1 = LOCATION OF FIRST DATA POINT IN AN "INCREASE" OR
C....  "DECREASE"
C....  INCF/DECF = INDICATES IF AN "INCREASE"/"DECREASE" WAS FOUND IN
C....  THE SPECIFIED SEARCH LIMIT
C....  NID = NUMBER OF INCREASES (OR DECREASES) USED TO IDENTIFY AN
C....  "INCREASE" (OR "DECREASE") IN THE SUBROUTINE INC (OR DEC)
C....  SP = THE APROXIMATE SPIN PERIOD
C
      INTEGER DATA,DEC1,NID,NA,DRANL,DRANU
      INTEGER DECF,PRANL,PRANU,NA,NFI,ARRAY(5000),TRKNUM,THRESH
      COMMON /ALL/ DATA(1100)
      COMMON /MDI/ NID,ICON,IJUMP
      COMMON /MPDI/ THRESH
      COMMON /MPB/ T1P,J1
      COMMON /MP/ T,THRYES,RATIO,ITHRSH
      COMMON /MB/ SP
      DATA NID,NA,THRESH,ICON,IJUMP/5,3,425,9,100/
      DATA J1,T1P/0,0.0/
      DATA STOP,ITHRSH/500.0,0/
      REWIND 1
      REWIND 2
      REWIND 3
C
C....  INITIALIZE DATA(1-100) TO ZERO.
C
      DO 10 J=1,100
   10   DATA(J)=0
      PRINT (5,*) "ENTER THE TRACK NUMBER AND THE APPROXIMATE SPIN PERIO
     1D IN MILLISECONDS;"
      READ (4,*) TRKNUM,SP
```

```
      PRINT (5,*) "THE CURRENT PARAMETER VALUES ARE;"
      PRINT (5,*) "THRESHOLD=",THRESH,", IJUMP=",IJUMP,", STOP=",STOP
      PRINT (5,*) "DO YOU WANT TO CHANGE ANY PARAMETERS ?"
      READ 20, PARYES
   20 FORMAT (A6)
      IF (PARYES.EQ."N") GO TO 30
      PRINT (5,*) "ENTER DESIRED VALUES"
      READ (4,*) THRESH,IJUMP,STOP
      PRINT (5,*) "THRESHOLD=",THRESH,", IJUMP=",IJUMP,", STOP=",STOP
   30 PRINT (5,*) "ADAPTIVE THRESHOLD OPTION ? (Y OR N)"
      READ 40, THRYES
   40 FORMAT (A6)
C
C....  THE ADAPTIVE THRESHOLD OPTION WILL SET A NEW THRESHOLD EQUAL TO A
C....  CERTAIN FRACTION (SPECIFIED BY RATIO) OF THE PREVIOUS PEAK VALUE.
C
      IF (THRYES.EQ."N") GO TO 50
      PRINT (5,*) "ENTER THRESHOLD RATIO AND INITIAL THRESHOLD;"
      READ (4,*) RATIO,THRESH
      ITHRSH=THRESH
C
C....  READ ONE RECORD FROM THE TAPE INTO ARRAY.
C
   50 READ (1) T,ARRAY
      IF (EOF(1).NE.0.0) STOP
      IF (T.GT.STOP) STOP
C
C....  OUTPUT THE TIMES OF EVERY TENTH RECORD TO INDICATE TO
C....  THE USER THAT THE TAPE IS BEING READ.
C
      IF (AMOD(T,10.0).EQ.0.0) PRINT (5,*) "T= ",T
C
C....  READ THE TRACK SPECIFIED BY TRKNUM FROM ARRAY INTO
C....  DATA(100-1100).
C
      DO 60 L=1,4996,5
        L1=101+((L-1)/5)
        L2=TRKNUM+L-1
   60   DATA(L1)=ARRAY(L2)
      INC1=-NID+1
      DEC1=-NID+1
      JJ=-SP*.8
C
C....  IF A PEAK WAS FOUND SET LOWER SEARCH LIMIT OF SUBROUTINE
C....  INC TO A NUMBER OF LOCATIONS PAST THE PREVIOUS PEAK
C....  WHICH IS EQUAL TO 80% OF THE APPROXIMATE SPIN PERIOD
C....  IN MILLISECONDS. IF A PEAK WAS NOT FOUND SET THE LOWER
C....  SEARCH LIMIT TO THE TENTH ELEMENT OF THE PREVIOUSLY
C....  DETECTED "DECREASE".
C
   70 IRANL=DEC1+NID+(SP*.8)+JJ
      JJ=0
```

```
      IF (IRANL.GT.1090) GO TO 80
C
C....  SET UPPER SEARCH LIMIT FOR SUBROUTINE INC TO LOCATION 1100.
C
      IRANU=1100
      CALL INC (IRANL,IRANU,INCF,INC1)
      IF (INCF.EQ.0) GO TO 80
      IF (1100-(INC1+NID).LT.10) GO TO 80
C
C....  SET LOWER SEARCH LIMIT FOR SUBROUTINE DEC TO INC1+NID.
C
      DRANL=INC1+NID
C
C....  SET UPPER SEARCH LIMIT FOR SUBROUTINE DEC TO LOCATION 1100.
C
      DRANU=1100
      CALL DEC (DRANL,DRANU,DECF,DEC1)
      IF (DECF.EQ.0) GO TO 80
C
C....  SET SEARCH LIMITS FOR SUBROUTINE PEAK.
C
      PRANL=INC1+NID
      PRANU=DEC1+10-NID
      IF ((PRANL.LT.2).OR.(PRANU.GT.1099)) GO TO 80
      CALL PEAK (PRANL,PRANU,NA,NFI)
      GO TO 70
   80 CONTINUE
C
C....  MOVE LAST HUNDRED ELEMENTS OF DATA(1100) INTO DATA(1-100).
C
      DO 90 K=1,100
        K1=1000+K
   90   DATA(K)=DATA(K1)
      GO TO 50
      END
C
      SUBROUTINE PEAK (PRANL,PRANU,NA,NFI)
C
C....  THIS SUBROUTINE WILL SEARCH FOR A "PEAK" WITHIN THE LOCATIONS OF
C....  DATA(1100) SPECIFIED BY THE SEARCH LIMITS PRANU & PRANL. IF
C....  NECESSARY, SUBROUTINE PEAK WILL CALL THE SMOOTHING SUBROUTINE
C....  SMOOTH UP TO NINE TIMES TO IDENTIFY A "PEAK". IF A "PEAK" IS
C....  FOUND, THE PEAK VALUE IS WRITTEN TO THE OUTPUT FILE UVOUT ALONG
C....  WITH THE CORRESPONDING TIME AND NUMBER OF SMOOTHING ITERATIONS.
C....  THEN A CALL IS MADE TO SUBROUTINE BACK AND THE RESULTING
C....  BACKROUND VALUE AND CORRESPONDING TIME ARE WRITTEN TO OUTPUT
C....  FILE BOUT. IF NO "PEAK" IS IDENTIFIED AFTER NINE CALLS TO SMOOTH,
C....  CONTROL IS RETURNED TO THE MAIN PROGRAM AND NOTHING IS WRITTEN TO
C....  THE OUTPUT FILES.
C....  PRANL = LOWER SEARCH LIMIT
C....  PRANU = UPPER SEARCH LIMIT
C....  NFI = NUMBER OF FILTER ITERATIONS
```

```
C....  NDB = NUMBER OF DATA POINTS BETWEEN PREVIOUS PEAK AND
C....  PRESENT PEAK
C....  NLM = NUMBER OF LOCAL MAXIMUMS
C....  J1 = PREVIOUS PEAK LOCATION
C....  J2 = PRESENT PEAK LOCATION
C....  T1 = TIME CORRESPONDING TO PRESENT PEAK VALUE
C....  T1P = TIME CORRESPONDING TO PREVIOUS PEAK VALUE
C....  JB = NUMBER OF LOCAL MAXIMUMS
C
      INTEGER DATA,NFI,NLM,PRANL,PRANU,NLM,NDB,THRESH
      COMMON /ALL/ DATA(1100)
      COMMON /MPDI/ THRESH
      COMMON /MPB/ T1P,J1
      COMMON /MP/ T,THRYES,RATIO,ITHRSH
      COMMON /PB/ NDB,T1
      NFI=0
   10 NLM=0
      JB=0
      J3=0
      DO 30 I=PRANL,PRANU
C
C....  TEST FOR THE MAXIMUM ALLOWABLE NUMBER OF CALLS TO
C....  SUBROUTINE SMOOTH
C
       IF (NFI.EQ.10) GO TO 140
C
C....    COUNT NUMBER OF LOCAL MINIMUMS.
C
       IF ((DATA(I).LT.DATA(I+1)).AND.(DATA(I).LT.DATA(I-1))) JB=JB+1
C
C....    TEST FOR CANDIDATES FOR LOCAL MAXIMUMS.
C
       IF ((DATA(I).GE.DATA(I+1)).AND.(DATA(I).GE.DATA(I-1))) GO TO 20
       GO TO 30
C
C....    SET J2 EQUAL TO THE LOCATION OF THE PRESENT CANDIDATE FOR A
C....    LOCAL MAXIMUM. J3 IS THE LOCATION OF THE PREVIOUS CANDIDATE FOR
C....    LOCAL MAXIMUM.
C
   20  J2=I
C
C....    IF TWO CONSECUTIVE CANDIDATES ARE FOUND, CONSIDER THE FIRST ONE
C....    TO BE A LOCAL MAXIMUM AND IGNORE THE SECOND ONE. OTHERWISE THE
C....    LOCATION J2 IS CONSIDERED TO INDICATE A LOCAL MAXIMUM
C....    AND THE LOCAL MAXIMUM COUNT (NLM) IS INCREASED BY ONE.
C
       IF ((J2-J3).EQ.1) GO TO 30
       NLM=NLM+1
C
C....    SET J3 EQUAL TO THE LOCATION OF THE PRESENT LOCAL MAXIMUM
C....    AND JUMP TO THE TOP OF THE DO LOOP TO TEST THE NEXT POINT
C....    WITHIN THE SEARCH LIMITS.
```

```
C
      J3=J2
   30 CONTINUE
C
C.... RETURN TO MAIN PROGRAM IF NO LOCAL MAXIMUM IS FOUND.
C
      IF (NLM.EQ.0) GO TO 140
C
C.... IF EXACTLY ONE LOCAL MAXIMUM AND NO LOCAL MINIMUMS ARE FOUND
C.... GO TO 60. OTHERWISE CALL SUBROUTINE SMOOTH.
C
      IF ((NLM.EQ.1).AND.(JB.EQ.0)) GO TO 60
C
C.... FOR THE FIRST CALL TO SUBROUTINE SMOOTH INCREASE THE UPPER
C.... SEARCH LIMIT BY ELEVEN LOCATIONS. FOR SUBSEQUENT CALLS THE
C.... UPPER SEARCH LIMIT IS NOT CHANGED AGAIN.
C
      IF (NFI.EQ.0) GO TO 40
      GO TO 50
   40 PRANU=PRANU+11
      IF (((PRANL-40).LT.1).OR.((PRANU+40).GT.1100)) GO TO 140
C
C.... APPLY SMOOTHING TO A WINDOW WHICH IS 40 LOCATIONS WIDER ON
C.... EACH SIDE THAN THE SEARCH LIMIT.
C
   50 CALL SMOOTH (NA,NFI,PRANL-40,PRANU+29)
C
C.... NOW THAT THE DATA HAS BEEN SMOOTHED JUMP TO 10 TO SEARCH AGAIN
C.... FOR A SINGLE "PEAK".
C
      GO TO 10
   60 IF (J2.LE.100) GO TO 70
      GO TO 80
C
C.... CALCULATE THE TIME CORRESPONDING TO THE SINGLE LOCAL
C.... MAXIMUM WHICH WILL BE CONSIDERED TO BE A "PEAK".
C
   70 T1=T-1.0+((899.0+FLOAT(J2))/1000.0)
      GO TO 90
   80 T1=T+((FLOAT(J2)-101)/1000)
C
C.... IF TWO PEAKS ARE IDENTIFIED WITHIN 0.025 SECONDS OF EACH OTHER,
C.... THE SECOND ONE IS IGNORED AND CONTROL IS RETURNED TO THE MAIN
C.... PROGRAM.
C
   90 IF (ABS(T1P-T1).LT.0.025) RETURN
C
C.... IF THE PRESENT PEAK IS THE FIRST ONE FOUND IN THE PRESENT
C.... RECORD GO TO 100.
C
      IF (J1.EQ.0) GO TO 100
C
```

```
C....  APPLY AN ADAPTIVE THRESHOLD IF IT IS GREATER
C....  THAN OR EQUAL TO THE INITIAL THRESHOLD, OTHERWISE APPLY THE
C....  INITIAL THRESHOLD.
C
      IF (THRYES.EQ."Y") THRESH=IFIX(RATIO*FLOAT(DATA(J2)))
      IF (THRESH.LT.ITHRSH) THRESH=ITHRSH
C
C....  CALCULATE THE NUMBER OF DATA POINTS FROM THE PREVIOUS "PEAK" TO
C....  THE PRESENT "PEAK".
C
      NDB=IFIX(T1*1000.0)-IFIX(T1P*1000.0)
      CALL BACK (J2,BVAL,TBACK)
      WRITE (2,120) T1,DATA(J2),NFI,NDB
      GO TO 110
C
C....  IF THE ADAPTIVE THRESHOLD OPTION WAS CHOSEN AND THE PRESENT
C....  PEAK VALUE IS MORE THAN 50% GREATER THAN THE INITIAL
C....  THRESHOLD RETURN CONTROL TO THE MAIN PROGRAM.
C
  100 IF ((DATA(J2).GT.(IFIX(1.5*FLOAT(ITHRSH)))).AND.(THRYES.EQ.
     1"Y     ")) RETURN
      WRITE (2,130) T1,DATA(J2),NFI
  110 J1=J2
      T1P=T1
  120 FORMAT (1H ,F7.3,3X,I10,3X,I2,3X,I6)
  130 FORMAT (1H ,F7.3,3X,I10,3X,I2)
  140 RETURN
      END
C
      SUBROUTINE DEC (DRANL,DRANU,DECF,DEC1)
C
C....  THIS SUBROUTINE WILL SEARCH FOR A "DECREASE" WITHIN THE LOCATIONS
C....  OF DATA(1100) SPECIFIED BY THE SEARCH LIMITS DRANL & DRANU. IF
C....  A "DECREASE" IS FOUND SUBROUTINE DEC WILL RETURN WITH DECF=1 AND
C....  WITH DEC1 CONTAINING THE LOCATION OF THE FIRST ELEMENT
C....  OF THE "DECREASE".
C....  DRANL = LOWER SEARCH LIMIT
C....  DRANU = UPPER SEARCH LIMIT
C....  DECF=0  IF NO DECREASE IS FOUND IN SPECIFIED RANGE
C....  DECF=1  IF DECREASE IS FOUND IN SPECIFIED RANGE
C....  DEC1 = LOCATION OF FIRST DATA POINT IN A "DECREASE"
C
      INTEGER DATA,NID,DECF,DRANL,DRANU,DEC1,THRESH
      COMMON /ALL/ DATA(1100)
      COMMON /MDI/ NID,ICON,IJUMP
      COMMON /MPDI/ THRESH
      DECF=0
      IDATA=0
C
C....  TEST FOR AT LEAST NID DECREASES, WHICH ARE LESS THAN IJUMP,
C....  IN EACH SET OF TEN CONSECUTIVE POINTS WITHIN SPECIFIED RANGE.
C
```

```
   10 JYES=0
      DO 40 JTEN=1,ICON
        IF (DATA(DRANL+IDATA+JTEN-1).LT.THRESH) GO TO 40
        IF (DATA(DRANL+IDATA+JTEN).LT.DATA(DRANL+IDATA+JTEN-1)) GO TO 20
        GO TO 40
   20   IF ((DATA(DRANL+IDATA+JTEN-1)-DATA(DRANL+IDATA+JTEN)).LT.IJUMP)
     1  GO TO 30
        GO TO 40
   30   JYES=JYES+1
   40   CONTINUE
      IF (JYES.GE.NID) GO TO 50
C
C....  TRY NEXT SET OF TEN DATA POINTS ONLY IF WITHIN SPECIFIED RANGE.
C
      IDATA=IDATA+1
      IF ((DRANL+IDATA+9).GT.DRANU) GO TO 60
      GO TO 10
C
C....  INDICATE A DECREASE WAS FOUND AND DETERMINE THE LOCATION OF THE
C....  FIRST DATA POINT IN THE "DECREASE".
C
   50 DECF=1
      DEC1=DRANL+IDATA
   60 RETURN
      END
C
      SUBROUTINE INC (IRANL,IRANU,INCF,INC1)
C
C....  THIS SUBROUTINE WILL SEARCH FOR AN "INCREASE" WITHIN THE
C....  LOCATIONS OF DATA(1100) SPECIFIED BY THE SEARCH LIMITS IRANL &
C....  IRANU. IF AN "INCREASE" IS FOUND, SUBROUTINE INC WILL RETURN
C....  WITH INCF=1 AND WITH INC1 CONTAINING THE LOCATION OF THE FIRST
C....  ELEMENT OF THE "INCREASE".
C....  IRANL = LOWER SEARCH LIMIT
C....  IRANU = UPPER LIMIT OF RANGE
C....  INCF=0  IF NO INCREASE IS FOUND IN SPECIFIED RANGE
C....  INCF=1  IF INCREASE IS FOUND IN SPECIFIED RANGE
C....  INC1 = LOCATION OF FIRST DATA POINT IN AN "INCREASE"
C
      INTEGER DATA,NID,THRESH
      COMMON /ALL/ DATA(1100)
      COMMON /MDI/ NID,ICON,IJUMP
      COMMON /MPDI/ THRESH
      INCF=0
      IDATA=0
C
C....  TEST FOR AT LEAST NID INCREASES, WHICH ARE LESS THAN IJUMP,
C....  IN EACH SET OF CONSECUTIVE POINTS WITHIN SPECIFIED RANGE.
C
   10 JYES=0
      DO 40 JTEN=1,ICON
        IF (DATA(IRANL+IDATA+JTEN-1).LT.THRESH) GO TO 40
```

```
      IF (DATA(IRANL+IDATA+JTEN).GT.DATA(IRANL+IDATA+JTEN-1)) GO TO 20
      GO TO 40
   20 IF ((DATA(IRANL+IDATA+JTEN)-DATA(IRANL+IDATA+JTEN-1)).LT.IJUMP)
     1 GO TO 30
      GO TO 40
   30 JYES=JYES+1
   40 CONTINUE
      IF (JYES.GE.NID) GO TO 50
C
C.... TRY NEXT SET OF TEN DATA POINTS ONLY IF WITHIN SPECIFIED RANGE.
C
      IDATA=IDATA+1
      IF ((IRANL+IDATA+9).GT.IRANU) GO TO 60
      GO TO 10
C
C.... INDICATE AN INCREASE WAS FOUND AND DETERMINE THE LOCATION OF THE
C.... FIRST DATA POINT IN THE "INCREASE".
C
   50 INCF=1
      INC1=IRANL+IDATA
   60 RETURN
      END
C
      SUBROUTINE SMOOTH (NA,NFI,PRANL,PRANU)
C
C.... THIS SUBROUTINE WILL SMOOTH THE DATA POINTS IN DATA(1100)
C.... THAT ARE WITHIN THE LOCATIONS BOUNDED BY PRANL & PRANU. THE
C.... CURRENT VALUE OF NFI WILL BE INCREMENTED BY 1 EACH TIME
C.... THIS SUBROUTINE IS CALLED.
C.... NA = NUMBER POINTS AVERAGED
C.... NFI = NUMBER OF FILTER ITERATIONS
C
      INTEGER NA,NFI,PRANL,PRANU,I,NAT,SUM,DATA
      COMMON /ALL/ DATA(1100)
      NFI=NFI+1
      IF (NFI.EQ.10) GO TO 30
      DO 20 I=PRANL,PRANU
        NAT=NA/2
        SUM=0
        DO 10 J=1,NA
   10     SUM=SUM+DATA(I-NAT+J-1)
   20   DATA(I)=SUM/NA
   30 RETURN
      END
C
      SUBROUTINE BACK (J2,BVAL,TBACK)
C
C.... THIS SUBROUTINE WILL DETERMINE AND WRITE A BACKROUND VALUE
C.... TO OUTPUT FILE BOUT EXCEPT IF THE PRESENT "PEAK" AND THE PREVIOUS
C.... "PEAK" ARE NOT IN THE SAME RECORD OR IF THE DISTANCE FROM THE
C.... PREVIOUS "PEAK" TO THE PRESENT "PEAK" IS NOT WITHIN A 9.6
C.... PERCENT DEVIATION FROM THE APROXIMATE SPIN PERIOD.
```

```
C....  J1 = PREVIOUS PEAK LOCATION
C....  J2 = PRESENT PEAK LOCATION
C....  BVAL = BACKROUND LEVEL
C....  TBACK = CORRESPONDING TIME OF BACKROUND LEVEL
C
      INTEGER DATA,BVAL
      COMMON /ALL/ DATA(1100)
      COMMON /PB/ NDB,T1
      COMMON /MPB/ T1P,J1
      COMMON /MB/ SP
C
C....  TEST TO SEE IF THE PRESENT AND PREVIOUS "PEAKS" ARE NOT IN
C....  THE SAME RECORD OR IF THE DISTANCE BETWEEN THEM IS NOT
C....  WITHIN 9.6 PERCENT OF THE APROXIMATE SPIN PERIOD.
C
      MIN=IFIX(SP-(SP*.096))
      MAX=IFIX(SP+(SP*.096))
      IF ((NDB.LT.MIN).OR.(NDB.GT.MAX).OR.(J1.GT.J2)) RETURN
C
C....  CALCULATE THE TIME CORRESPONDING TO THE PRESENT BACKROUND VALUE.
C
      TBACK=((T1-T1P)/2.)+T1
      KMID=J1+NDB/2
      JCOUNT=0
      ISUM=0
C
C....  DETERMINE THE PRESENT BACKROUND LEVEL.
C
      I1=KMID-25
      I2=KMID+25
      DO 10 I=I1,I2
   10   ISUM=ISUM+DATA(I)
      BVAL=ISUM/51
      WRITE (3,20) TBACK,BVAL
   20 FORMAT (1H ,F7.3,3X,I10)
      RETURN
      END
      END
```

A.I.2 Sample output of the program UVPEAKS

Elapsed time from launch	Peak value	Number of filter iterations	Number of data points between peaks
107.356	812	1	207
107.568	821	1	212
107.779	796	2	211
107.990	798	2	211
108.201	799	2	211
108.409	798	2	208
108.621	801	2	212
108.832	780	4	211
109.042	801	1	210
109.253	797	3	211
109.463	796	2	210
109.672	815	2	209
109.883	793	2	211
110.093	812	1	210
110.305	811	2	212
110.516	802	2	211
110.726	820	2	210
110.936	825	0	210
111.147	824	2	211
111.358	817	2	211
111.567	838	1	209
111.779	847	1	212
111.989	844	1	210
112.198	871	1	209
112.410	860	1	212
112.619	872	1	209
112.832	889	1	213
113.043	874	2	211
113.251	890	2	208
113.464	904	1	213
113.672	916	1	208
113.885	930	1	213
114.095	936	1	210
114.305	942	1	210
114.515	955	1	210
114.724	967	1	209
114.935	983	1	211
115.147	987	1	212
115.358	997	1	211
115.567	1014	1	209
115.777	1011	1	210
115.990	1042	2	213
116.199	1033	2	209
116.410	1073	1	211
116.621	1058	2	211
116.831	1074	2	210
117.042	1098	1	211
117.253	1093	1	211
117.461	1115	2	208
117.674	1128	1	213
117.883	1139	1	209
118.094	1179	0	211
118.305	1160	1	211
118.516	1180	1	211
118.725	1180	2	209
118.937	1190	2	212
119.148	1222	1	211
119.358	1215	1	210
119.569	1265	0	211
119.780	1264	1	211
119.990	1256	1	210
120.200	1276	1	210

A.I.3 FOUR

```
      PROGRAM FOUR(INPUT,OUTPUT,FILE,TAPE1=FILE,MIKE,TAPE2=MIKE)
      REAL FN,F,AN
      REWIND 1
      PRINT*,"ENTER NUMBER OF ITERATIONS AND RISE TIME"
      READ*,N,TR
      N=N+1
      DO 10 IT=1,501
      T=.001*FLOAT(IT)-.251
      FN=.12
      F=0.0
      DO 20 I=1,N
      F=F+FN
      S=FLOAT(I)
      PI=3.1415926
      W=6.*S
      AN=(8.35/(PI*PI*S*S))*(1-COS(.2395*PI*S))
      IF(IT.EQ.1) WRITE(2,60) W,AN
   60 FORMAT(F12.5,F12.5)
      THETA=ATAN((TR*S)/.0612)
   20 FN=AN*COS((S*T*2.*PI-THETA)/.167)/SQRT(((PI*S*TR)**2.)*27.051+1.)
   10 WRITE(1,30) T,F
   30 FORMAT(1X,F7.3,3X,F12.5)
      STOP
      END
```